SNAPSHOT INTERFEROMETRIC SYSTEMS WITH POLARIZATION CAMERAS

by

Xiaobo Tian

A Dissertation Submitted to the Faculty of the

JAMES C. WYANT COLLEGE OF OPTICAL SCIENCES

In Partial Fulfillment of the Requirements

For the Degree of

DOCTOR OF PHILOSOPHY

In the Graduate College

THE UNIVERSITY OF ARIZONA

2020

THE UNIVERSITY OF ARIZONA
GRADUATE COLLEGE

As members of the Dissertation Committee, we certify that we have read the dissertation prepared by **Xiaobo Tian, titled** ***Snapshot Interferometric Systems with Polarization Camera*** and recommend that it be accepted as fulfilling the dissertation requirement for the Degree of Doctor of Philosophy.

Rongguang Liang ____________________ Date: 04/14/2020
Professor Rongguang Liang, Chair

Dae Wook Kim ____________________ Date: 4/14/2020
Professor Daewook Kim

SKHP ____________________ Date: 04/14/2020
Professor Stanley K. H. Pau

Final approval and acceptance of this dissertation is contingent upon the candidate's submission of the final copies of the dissertation to the Graduate College.

I hereby certify that I have read this dissertation prepared under my direction and recommend that it be accepted as fulfilling the dissertation requirement.

Rongguang Liang ____________________ Date: 04/14/2020
Professor Rongguang Liang
Dissertation Committee Chair
Wyant College of Optical Sciences

ACKNOWLEGEEMENTS

I would like to thank my advisor Prof. Rongguang Liang for all his help and guidance during my Ph.D. career, for his patience, motivation, immense knowledge and proactive attitude. I am deeply thankful to him for providing me the opportunity to pursue a wide array of projects throughout my Ph.D. career. Without his guidance and persistent help, this dissertation would not have been possible.

Besides my advisor, I would like to thank the rest of my dissertation committee members Prof. Stanley Pau and Prof. Dae Wook Kim for providing a helpful review of this dissertation. I would also like to thank my former research advisor Prof. Jose Sasian for his help in both research and life.

I would like to thank all the members of the Applied Optics Lab that I have collaborated with throughout my Ph.D. career. In particular, I would like to thank: Yu Zhang, Daodang Wang, Shaun Pacheco, Xiaoyin Zhu, Bofan Song, Zhihan Hong, Qi Cui and Shaobai Li for their useful discussions and collaborations.

I would like to thank all my friends, Miaomiao Xu, Xingzhou Tu, Yitian Ding, Yufeng Yan, Weichuan Gao and many others for their friendship.

Finally, I would like to thank my family for their endless love, encouragement, and support.

DEDICATION

To my parents, Qingshui Tian and Mengxia Wang.

Contents

LIST OF FIGURES

LIST OF TABLES

ABSTRACT

Interferometry has been established as an important tool for a variety of applications, including physics, industrial manufacturing, biology, and medicine. Phase-shifting interferometry is one of the most general methods in interferometric systems for its high measurement accuracy, rapid measurement, good results for low contrast fringes, and independence of irradiance variations across the pupil. In most cases, the phase calculation error caused by environmental noise is the primary error. Comparing with temporal phase-shifting, which introduces a phase-shift sequentially, spatial phase-shifting methods that capture phase-shifted interferograms simultaneously can significantly reduce the influence of environmental noise.

In this dissertation, we present several snapshot phase-shifting interferometric systems with the pixelated mask spatial phase-shifting technique using a polarization camera. As a spatial phase-shifting method, the pixelated polarization camera method has the advantages of a common path configuration, compact design, achromatic over a very wide range, and fixed spatial interference patterns, which makes it suitable for dynamic measurement. Various applications based on this technique are presented, including on-machine interferometry, single-shot multi-wavelength interferometry, snapshot quantitative phase microscopy, and freeform surface metrology. The principles and applications are theoretical analyzed and experimental demonstrated for each system.

Chapter 1 Introduction to Optical Interferometry

1.1 Introduction

Over the past decades, optical interferometry has been established as one of the most general methods for optical metrology due to its high accuracy and relatively simple configuration. An interferometric system takes advantage of the wave nature of light. In most interferometers, one beam of light from the light source is separated into two beams that travel different paths. Then these two beams are combined and generate interference patterns. Based on the interference patterns, the information of the optical path difference (OPD) between these two paths can be calculated. The OPD information is used for precise measurement of small distance, thickness, refractive index of the materials, surface irregularities, and spectrum lines. Although there are many different kinds of interferometry configurations [1, 2], the basic configurations are similar, including a light source, an optical component that separates light into the test and reference beams, a standard reference surface in the reference arm, a test surface in the test arm, another optical component that recombines the test and reference beams, and a detector that records the interference fringes.

Interferometry technology has been developed for many years. In 1887 Albert Michelson and Edward Morley constructed the interferometer used in the Michelson-Morley experiment [3]. In

1907, Michelson was awarded the Noble Prize in Physics "for his optical precision instruments and the spectroscopic and metrological investigations carried out with their aid." The basic Michelson interferometer and its modification are widely used in optical research and industry for surface measurement of lenses and prisms, measurement of refraction index, or the speed of light in different mediums, and even the wind and temperature changes in the atmosphere.

With the development of light source, detector, and the computation power, different interferometer configurations have been developed [2], including Michelson interferometer, Fizeau interferometer, Mach-Zehnder interferometer, Twyman-Green interferometer, lateral shear interferometer, radial shear interferometer, point diffraction interferometer, multiple-wavelength interferometer, white light interferometer, and many others. Interferometry has been widely used in a variety of fields, including physics, engineering, applied science, and biology.

The largest limitation of a common interferometry for optical testing is the sensitivity to the environment, like vibration and air turbulence. In recent decades, dynamic interferometry has been developed [4, 5] to reduce the sensitivity to the environment. This dissertation focuses on the principle and applications of dynamic interferometric systems for measuring the optical surface information like the surface shape and the surface roughness, and the phase information of a biomedical samples.

1.2 Optical Interferometry

1.2.1 Basic Interference

A beam of light contains two basic information: irradiance and phase. Assume the wave is linearly polarized in *y*-direction and propagates in *z*-direction in a vacuum, the electric field U of the wave can be represented as:

$$U = a\exp[i(kz - \omega t + \phi_0)]\hat{y} = a\exp(i\phi)\exp[-i(\omega t + \phi_0)] \tag{1.1}$$

where a is the amplitude, $k = 2\pi / \lambda$ is the wavenumber, λ is the wavelength, z is the distance, ω is the oscillation frequency, t is the time, ϕ_0 is the phase offset, and ϕ is the corresponding phase difference. If we ignore the factors of proportionality, the irradiance of a single field is defined as:

$$I = \left|U\right|^2 = \int dtUU^* = a^2 \tag{1.2}$$

For two monochromatic wave propagate in the same direction and polarize in the same plane, the total field U is the sum of the components,

$$U = U_T + U_R \tag{1.3}$$

where U_T and U_R are the fields of the two waves. And the irradiance of this wave can be written as [6]:

$$\begin{aligned} I &= \left|U\right|^2 = \left|U_T + U_R\right|^2 \\ &= \left|U_T\right|^2 + \left|U_R\right|^2 + U_T U_R^* + U_T^* U_R \\ &= I_T + I_R + 2\sqrt{I_T I_R}\cos(\phi) \end{aligned} \tag{1.4}$$

where I_T and I_R are the irradiance of the two waves separately, and ϕ is the phase difference between them.

The contrast of the interference is described as visibility, which is defined as:

$$v = \frac{I_{\max} - I_{\min}}{I_{\max} + I_{\min}} \tag{1.5}$$

where I_{max} is the maximum irradiance value and I_{min} is the minimum irradiance value. If the two fields are monochromatic with the same polarization, the visibility can be written as:

$$v = \frac{2\sqrt{I_T I_R}}{I_T + I_R} \tag{1.6}$$

1.2.2 Transform-based Algorithm

There are mainly two algorithms used to extract phase information from interferograms: transform-based algorithm [7] and phase-shifting algorithm [8]. Transform-based algorithms, including Fourier transform [7], Hilbert transform [9], windowed Fourier transform [10], wavelet transform [11], the energy minimization method [12], and so on, extract the phase from a single interferogram. The carrier can be introduced by adding a large tilt to the interferogram. The interferogram with certain carrier can be written as:

$$I(x,y) = I_a(x,y) + I_b(x,y)\cos[2\pi f_0 x + \phi(x,y)] \tag{1.7}$$

where $I_a(x,y)$ and $I_b(x,y)$ are the unwanted irradiance variations, and $\phi(x,y)$ is the phase. In most cases, $I_a(x,y)$, $I_b(x,y)$ and $\phi(x,y)$ vary slowly compared with the variation introduced by the spatial-carrier frequency f_0. The input irradiance can be rewritten as:

$$I(x,y) = I_a(x,y) + I_c(x,y)\exp(2\pi i f_0 x) + I_c^*(x,y)\exp(-2\pi i f_0 x) \tag{1.8}$$

$$I_c(x,y) = \frac{1}{2} I_b(x,y)\exp[i\phi(x,y)] \tag{1.9}$$

where $*$ denotes a complex conjugate. Then a Fourier transform can be applied with respect to Equation 1.8 by the use of a fast-Fourier-transform (FFT) algorithm, which give

$$\tilde{I}(f,y)=\tilde{I}_a(f,y)+\tilde{I}_c(f-f_0,y)+\tilde{I}_c^*(f+f_0,y) \tag{1.10}$$

where $\tilde{I}$ is the Fourier transform of *I*. The irradiance of $I_c(x,y)$ is separated by the carrier frequency f_0 in Frequency domain, which can be obtained by translating $\tilde{I}_c(f-f_0,y)$ back to origin and inverse Fourier transform of $\tilde{I}_c(f,y)$. A complex logarithm can be applied to Equation 1.9 as:

$$\log[I_c(x,y)]=\log\left[I_b(x,y)/2\right]+i\phi(x,y) \tag{1.11}$$

The phase in the imaginary part can be separated from the unwanted amplitude variation I_b in the real part.

The phase information in the interferogram is obtained from a single interferogram, which makes it useful for single-shot measurement. However, there are sign ambiguity problems for these methods, including the local sign ambiguity and the global sign ambiguity. Usually the prior knowledge of the measured surface is needed to determine the accurate inclination direction of the reconstructed phase. Besides, the spatial resolution of the phase image is also limited due to the high frequency carrier and the Fourier transform process.

1.2.3 Phase-Shifting Algorithm

Interferometry, which uses phase-shifting techniques, is considered as phase-shifting interferometry (PSI) [1, 2, 13, 14]. PSI is a powerful tool for analyzing interferograms to recover the phase information, with the advantages of high measurement accuracy, rapid measurement, good results with low contrast fringes, results independent of irradiance variations across the pupil, and obtaining phase at a fixed grid of points.

PSI can be classified into temporal phase-shifting and spatial phase-shifting. In the temporal phase-shifting technique, at least three phase-shifted interferograms are captured in time sequence, which can be achieved by a piezoelectric transducer (PZT) [15], frequency shifting source, and polarization phase shifters [16,17]. In the spatial phase-shifting techniques, several phase-shifted interferograms are captured within a single shot at different locations by multi-cameras or on different areas of a camera [4,5,18-26].

In PSI, a set of interferograms are recorded with preset phase-shift values. The interferogram with certain phase-shift value can be written as:

$$I = I_T + I_R + 2\sqrt{I_T I_R}\cos(\phi + \delta) \tag{1.12}$$

where δ is the relative phase-shift between the two beams. The number of interferograms can be three, four, five or more. Based on the number of interferograms, different phase reconstruction algorithms [2, 27] can be applied. The three-step algorithm has phase-shift values of $\pi/3$, π, and $5\pi/3$. The irradiance can be written as:

$$\begin{aligned} I_1 &= I_T + I_R + 2\sqrt{I_T I_R}\cos(\phi + \pi/3) \\ I_2 &= I_T + I_R + 2\sqrt{I_T I_R}\cos(\phi + \pi) \\ I_3 &= I_T + I_R + 2\sqrt{I_T I_R}\cos(\phi + 5\pi/3) \end{aligned} \tag{1.13}$$

and the phase can be calculated by:

$$\phi = \tan^{-1}\left(\sqrt{3}\,\frac{I_3 - I_1}{I_3 + I_1 - 2I_2}\right) \tag{1.14}$$

Thus the phase at each point on the detector can be obtained from the interferograms. While the three-step algorithm is simple, it is sensitive to measurement noise. In order to increase the accuracy of the measurement, four-step and five-step algorithms have been developed.

In four-step algorithm, phase-shift values are 0, $\pi/2$, π, and 3 $\pi/2$. The irradiance of the four interferograms are:

$$\begin{aligned} I_1 &= I_T + I_R + 2\sqrt{I_T I_R}\cos(\phi) \\ I_2 &= I_T + I_R - 2\sqrt{I_T I_R}\sin(\phi) \\ I_3 &= I_T + I_R - 2\sqrt{I_T I_R}\cos(\phi) \\ I_4 &= I_T + I_R + 2\sqrt{I_T I_R}\sin(\phi) \end{aligned} \tag{1.15}$$

The phase can be calculated as:

$$\phi = \tan^{-1}\frac{I_4 - I_2}{I_1 - I_3} \tag{1.16}$$

As for five-step algorithm, the phase shift values are 0, $\pi/2, \pi,$ 3 $\pi/2$ and 2 π. The phase can be calculated as:

$$\phi = \tan^{-1}[\frac{2(I_2 - I_4)}{2I_3 - I_1 - I_5}] \tag{1.17}$$

1.3 Dynamic Interferometry

Dynamic interferometry can be achieved by transform-based techniques [12] or spatial phase-shifting techniques [4,5,18-26]. Compared to the interferometry using transform-based algorithms, PSI has high accuracy and low uncertainty for optical testing. However, traditional temporal PSI acquires data over a series of camera frames. The measurement accuracy can be influenced by environmental noise like vibration and air turbulence. Vibration effect can be reduced by taking all the phase-shifted interferograms simultaneously. Simultaneous PSI can be achieved by using spatial carrier [18-20], multi-cameras [21-23], holographic element [5], and a polarization camera

[25, 26] which has a micro-polarizer array attached on the detector. By using these dynamic PSI techniques, the advantages of PSI can be kept while the vibration problem can be reduced.

1.3.1 Spatial Carrier Method

The spatial carrier method introduces a known angle between the test and reference arms, typically by tilting the reference surface. Within each small window on the detector, the phase varies linearly and the phase difference between adjacent pixels is constant. Thus a normal phase-shifting algorithm can be used to calculate the phase. However, if the test wavefront contains large aberration, the fringes are not equally spaced on the detector, which may influence the measurement accuracy. Some systematic errors may be introduced since the beams are sheared at the detector and the beams travel different paths through the system. In order to reduce such errors, another approach uses a phase filter like Wollaston prism to generate tilt between the test and reference beams. In such configuration, the test beam and reference beam are orthogonally polarized. The phase filter followed by a polarizer is placed directly in front of the detector.

1.3.2 Multi-cameras Method

One classical technique of simultaneous PSI with multi-cameras is shown in Figure 1.1 [5]. Four phase-shifted interferograms can be captured with phase-shifted values of 90° at the same time on different cameras. The incident light is linear polarized at an angle of 45 degrees. A $\lambda/8$ wave plate is placed in the reference arm oriented along the x-axis. The light in the reference arm passes through the $\lambda/8$ wave plate twice, which generate a 90° phase difference between the x and y components. A polarized beam splitter is used to separate the light to x and y directions. When the reference arm interferences with the test arm, a 90 degree phase-shift is generated between the x-direction and y-direction on the two detectors at each side of the PBS. In the dielectric beam splitter, a 180° phase difference is introduced between the two interfering beams if one of the two beams is reflected from a high index medium to a low index medium and the other beam is reflected from a low index medium to a high index medium. For the beams going back toward the laser, there is a 180° phase difference between the interferograms in the normal interferometer output and the interferograms going back toward the laser. Based on this principle, the two interferograms on each side of the PBS2 have a 180° phase difference comparing with the two interferograms on each side of the PBS1. Thus, four phase-shifted interferograms can be captured simultaneously. One problem of such configuration is that the calibration and alignment requirements of the four cameras are very critical. And the system is not compact enough for certain applications.

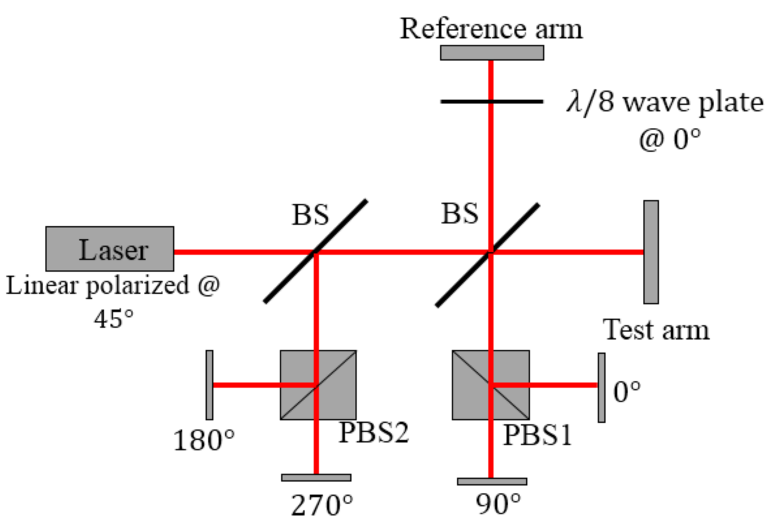

Figure 1.1 Simultaneous PSI with multi-cameras [5]

1.3.3 Holographic Polarization Method

In order to reduce the calibration and alignment difficulties of the multi-cameras method, the approach that has all four phase-shifted interferograms on a single detector was proposed [5]. In this configuration, a polarization beamsplitter introduces orthogonal polarization for the test and reference beams. These two beams pass through a holographic element that splits them into four separate beams. Four phase-shifted interferograms are generated by a birefringent mask and a linear polarizer at 45° just in front of the detector. Since all four interferograms are detected simultaneously on a single detector array, the alignment difficulty is reduced.

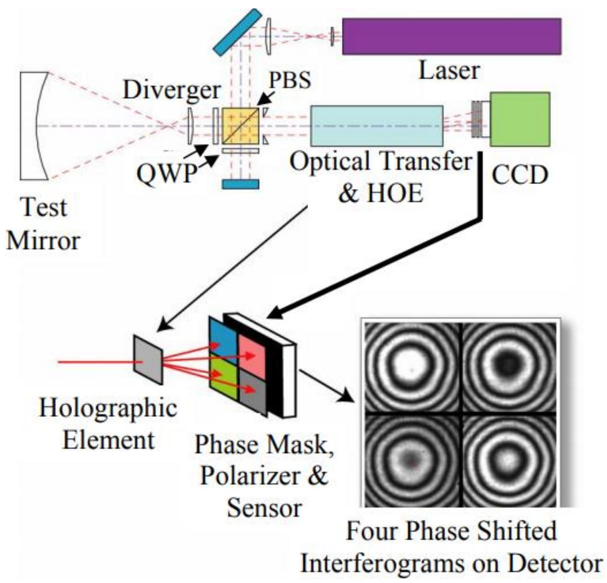

Figure 1.2 Simultaneous PSI with holographic element [5]

1.3.4 Polarization Camera Method

The polarization camera is composed of pixel-size linear polarizers oriented at four different angles (0°, 45°, 90°, and 135° are the polarization orientations employed in most polarization cameras), superimposed on a camera sensor chip, as shown in Figure 1.3(a) [28]. The polarization direction is filtered by the micro-polarizer array according to polarizer angles. Therefore, each pixel measures the irradiance coming from only 1 of the 4 different polarizers. Commercial polarization cameras include the PolarCam device from 4D Technology and the IMX250MZR polarization-dedicated sensor from SONY (Tokyo, Japan). For custom polarization sensors, the pixelated polarizer is attached on top of the on-chip lens layer, as shown in Figure 1.3(b) [28]. The optical crosstalk increases with the incident angle and the distance between the polarizer and photodiode. Under a given f-number condition, to minimize optical crosstalk, it is important to reduce the distance. The polarizer in Sony's polarization sensor is formed on chip under the on-chip lens layer, as shown in Figure 1.3(c) [28]. A shorter distance between the polarizer and the photodiode improves the extinction ration, reduces the incident angle dependence, and reduces the polarization crosstalk.

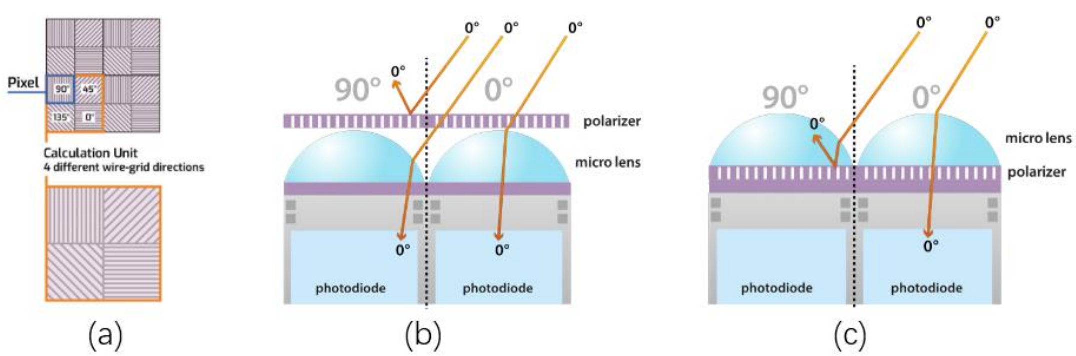

Figure 1.3 Polarization camera sensor (a) Polarization filter array. (b) Structure of conventional polarization sensor and (c) Sony polarization sensor. [28]

For two incident beams with opposite circular polarization, the Jones Vector of the incident beams can be written as: $E_T = \frac{1}{\sqrt{2}}\begin{bmatrix}1\\ i\end{bmatrix}e^{i\varphi}$ and $E_R = \frac{1}{\sqrt{2}}\begin{bmatrix}1\\ -i\end{bmatrix}$. After passing through a linear polarizer at $\theta°$, the output beam is $E = P*(E_T + E_R)$, where $P = \begin{bmatrix} \cos^2\theta & \sin\theta\cos\theta \\ \sin\theta\cos\theta & \sin^2\theta \end{bmatrix}$ is the Jones matrix of the polarizer. After passing through the polarizer, the irradiance with two incident orthogonal circular polarization states is:

$$I = EE^* = I_T + I_R + 2\sqrt{I_T I_R}\cos(\phi + 2\theta) \tag{1.20}$$

A phase-shift value of 2θ is introduced by a polarizer orientated at θ. This serves as the foundation for the pixelated mask phase-shifting. The arrangement of the polarization camera phase shifter is shown in Figure 1.4. The linear polarizers in the polarizer array are a set of metal wires at angles of 0°, 45°, 90°, and 135°, introducing phase shifts at 0°, 90°, 180°, and 270°. The irradiance within each subpixel can be written as:

$$\begin{aligned} I_1 &= I_T + I_R + 2\sqrt{I_T I_R}\cos(\phi) \\ I_2 &= I_T + I_R - 2\sqrt{I_T I_R}\sin(\phi) \\ I_3 &= I_T + I_R - 2\sqrt{I_T I_R}\cos(\phi) \\ I_4 &= I_T + I_R + 2\sqrt{I_T I_R}\sin(\phi) \end{aligned} \tag{1.21}$$

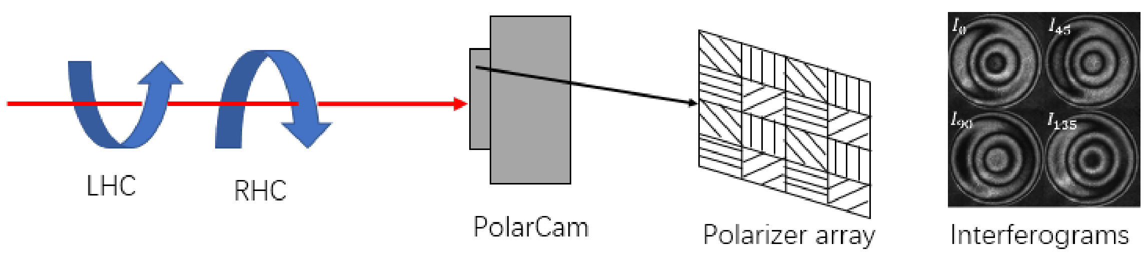

Figure 1.4 Polarization camera phase shifter arrangement

1.4 Conclusion

Interferometry is the most important method in optical metrology. In this chapter, the author introduces the basic principle of interference, phase reconstruction algorithms, and different methods of dynamic phase-shifting interferometry. The dynamic phase-shifting interferometry based on the polarization camera has been widely adopted to optical metrology due to the advantage of high measurement accuracy, fast measurement speed, insensitive to environmental noise, and relatively compact configuration. This dissertation contains the principle of dynamic spatial phase-shifting interferometry and a collection of different applications based on such configuration. For each chapter, the author discusses the principle and applications of each system.

Chapter 2 introduces a dual-mode snapshot interferometry system for on-machine metrology, which contains the function of both macro-interferometry and micro-interferometry. The limitations of current on-machine metrology systems are discussed. Both numerical analysis and experiments have been carried out to demonstrate the feasibility of this system.

Chapter 3 introduces a snapshot multi-wavelength interference microscope for high speed measurement of large vertical range discontinuous microstructures and surface roughness. The limitation of the measurement range of a common interference microscope is discussed. By using a customized polarization camera with a linear micro-polarizer array and Bayer filters, snapshot multi-wavelength phase-shifting measurement is achieved. Camera calibration of the color polarization camera is discussed in this chapter.

Chapter 4 introduces a multi-wavelength quantitative polarization and phase microscope for measuring the spectral dependent quantitative polarization and phase information. This system integrates a polarized light microscope and a snapshot quantitative phase microscope in a single system, utilizing a novel full-Stokes camera operating in the red, green, and blue spectrum. The customized RGB full-Stokes camera is built with two customized color polarization cameras, a non-polarization beam splitter, one achromatic quarter waveplate, and one glass compensation plate with the same thickness as the achromatic quarter waveplate. The operating principle and calibration method are discussed in this chapter. A red blood cell sample is measured to demonstrate the feasibility of measuring quantitative polarization and phase information of live cells.

Chapter 5 introduces a snapshot phase-shifting diffraction phase microscope. Diffraction phase microscope is widely used in biomedical sample measurement. However, the most commonly used phase reconstruction method in the diffraction phase microscope is the Fourier transform algorithm, which limits the reconstruction performance of the high frequency information. In this chapter, the author introduces a snapshot phase-shifting diffraction phase microscope by a polarization grating and a polarization camera. Both reflection and transmission modes are demonstrated with experiments.

Chapter 6 discusses a snapshot adaptive freeform null testing system with a deformable mirror compensator. Freeform measurement is one of the key barriers in effectively and expediently fabricating complex freeform elements. Using a deformable mirror as an adaptive null component is one of the solutions. A deformable mirror control algorithm based on the stochastic parallel gradient descent algorithm is developed to control the deformable mirror to null the interference fringes. By using a polarization camera for snapshot measurement, the iterative speed is much increased.

Chapter 2 Snapshot Dual-mode Interferometric System for On-machine Metrology

2.1 Introduction

With the increasing need for high precision optical elements, an accurate and efficient metrology method is highly demanded. As an accurate testing method, the interferometry has been widely used as a non-contact surface metrology for optical elements. To evaluate the fabrication quality of the optical elements, surface form and surface roughness measurements are necessary. Various laser interferometers, such as Fizeau interferometer, Twyman-Green interferometer, and point-diffraction interferometer [1, 2], have been developed for surface form measurement. And interference microscopes [29] like white light interferometer are used for surface roughness measurement. By combining the laser interferometer and interference microscope, the surface characteristics can be evaluated over a wide range of spatial frequencies precisely.

Typically, the fabricated optical elements are measured in off-line condition for both surface form and surface roughness. The fabricated part needs to be removed from the workspace and remount back to the machining tool if the part is not fabricated to the specification. The off-line metrology places an ultrahigh requirement on the precision of the part re-installation, increasing the fabrication time and introducing extra alignment errors. However, most of the commercial measurement tools are designed for off-line metrology, which are large in volume and sensitive to environmental noise. And most of the commercial available interferometers are designed for only a single working mode, either interferometer mode or interference microscope mode. These commercial tools are hard to be applied for on-machine measurement.

Various on-machine metrology or in-process inspection techniques have been developed for ultra-precision machining systems, including hybrid vision system [30], chromatic confocal microscope [31-33], deflectometry [34] and interferometry [35-37]. However, all these methods are designed for either measuring surface form or surface roughness. To meet the need for measuring both surface form and surface roughness, we developed a compact and dual-mode snapshot interferometric system using a Linnik configuration [38].

In this chapter, a snapshot dual-mode interferometric system (SDIS) is presented for on-machine metrology for diamond turning optical fabrication. This system combines a laser interferometer and an interference microscope in a single system, which can be used for measuring both surface form and surface roughness. Four phase-shifted interferograms are captured within a single-shot by using a polarization camera. This SDIS was build and validated on a Moore Nanotech 350FG diamond turning machine (DTM).

2.2 Polarization Camera

The spatial phase-shifting with polarization camera has significant advantages in dynamic interferometer because of its snapshot nature. However, this kind of camera also suffers from several errors like fixed pattern noise (FPN), photon response nonuniformity (PRNU), nonuniformity in the micro-polarizer extinction ration, micro-polarizer array orientation misalignment and pixel cross-talk [39]. As an important optical component in the interferometer, camera calibration is necessary for high accuracy measurement. For a common polarization camera, a wire-grid micro-polarizer array is attached in front of the detector. The micro-polarizer array contains four linear polarizers orientated at four different angles (0°, 45°, 90°, and 135°), forming a 2 x 2 superpixel. Four phase-shifted interferograms with the phase-shift values of 0°, 90°, 180°, and 270° are capture within a single shot. Since each pixel can only measure one polarization state, the Stokes vector of each pixel is reconstructed by the integration algorithm [40]. To calculate the phase value, the irradiance is recovered by a weighted average in a 3 x 3 grid in camera calibration, as shown in Figure 2.1. The irradiance $I_{0°}$, $I_{45°}$, $I_{90°}$, and $I_{135°}$ of the pixel (i, j) are represented as:

$$\begin{aligned} I_{135^\circ} &= I_{i,j} \\ I_{0^\circ} &= (I_{i,j-1} + I_{i,j+1})/2 \\ I_{90^\circ} &= (I_{i-1,j} + I_{i+1,j})/2 \\ I_{45^\circ} &= (I_{i-1,j-1} + I_{i+1,j-1} + I_{i-1,j+1} + I_{i+1,j+1})/4 \end{aligned} \tag{2.1}$$

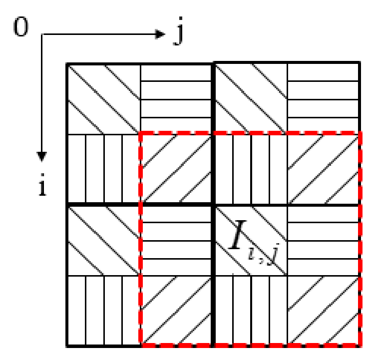

Figure 2.1 Schematic of the micro-polarizer array

The weighted average is a linear combination of neighboring pixels, which has the same format of linear interpolation of $I_{0°}$, $I_{45°}$, $I_{90°}$, and $I_{135°}$ polarization states in pixel (i, j). A linear-spline interpolation can is used to recover the missing irradiance of each pixel as $I = \left[I_0\ I_{45}\ I_{90}\ I_{135}\right]^T$. The incident light can be represented by the Stokes vector $\vec{S}_{in} = \left[S_0\ S_1\ S_2\ S_3\right]^T$. S3 is the circular part in the Stokes vector of the incident light, which is 0 in our experiment. The input Stokes vector $\vec{S}_{in}$ is revised as $\vec{S}_{in} = \left[S_0\ S_1\ S_2\right]^T$. The measurement matrix *W* and corresponding pixel offsets *d* are written as:

$$W = \begin{bmatrix} w0_0 & w0_1 & w0_2 \\ w45_0 & w45_1 & w45_2 \\ w90_0 & w90_1 & w90_2 \\ w135_0 & w135_1 & w135_2 \end{bmatrix}, d = \begin{bmatrix} d0 \\ d45 \\ d90 \\ d135 \end{bmatrix} \tag{2.2}$$

in which *w0, w45, w90,* and *w135* are the first rows of the corresponding Mueller matrix of each linear analyzer, and *d0, d45, d90,* and *d135* are the corresponding pixel offsets in the superpixel. The relationship between irradiance *I*, measurement matrix *W*, corresponding pixel offsets *d*, and input Stokes vector S_{in} of each pixel is:

$$I = W \cdot \vec{S}_{in} + d \tag{2.3}$$

The measurement matrix *W* can been acquired by

$$W = [I - d] \cdot S_{in}^{-1} \tag{2.4}$$

where S_{in}^{-1} is the pseudo-inverse of S_{in}. The ideal measurement matrix of the four linear analyzers W_{ideal} can be described as:

$$W_{ideal} = \frac{1}{2}\begin{bmatrix} 1 & 1 & 0 & 0 \\ 1 & 0 & 1 & 0 \\ 1 & -1 & 0 & 0 \\ 1 & 0 & -1 & 0 \end{bmatrix} \tag{2.5}$$

The corrected irradiance of each pixel is

$$I_{corrected} = W_{ideal} \cdot W^{-1} \cdot [I - d] \tag{2.6}$$

where W^{-1} is the pseudo-inverse of *W*. After calibration, the corrected irradiance of four polarization states is reconstructed at each pixel.

The setup for the calibration process is shown in Figure 2.2. A LED with a central wavelength of 630 nm and a 10 nm bandpass filter is used as the light source, which is the same light source used in the interferometric system. The light from the light source passes through a bandpass filter and an integrating sphere to provide uniform illumination. A linear polarizer is placed in front of the polarization camera. The incident Stokes vector can be calculated by the orientation of the linear polarizer. The calibration is carried out with seven groups of input Stokes vectors with different illumination irradiance levels. Within each group, the linear polarizer is rotated from 0° to 170° with an increment of 10°. The image captured by the polarization camera is 12-bit raw data, and the pixel value is used to represent the relative irradiance of the incident light.

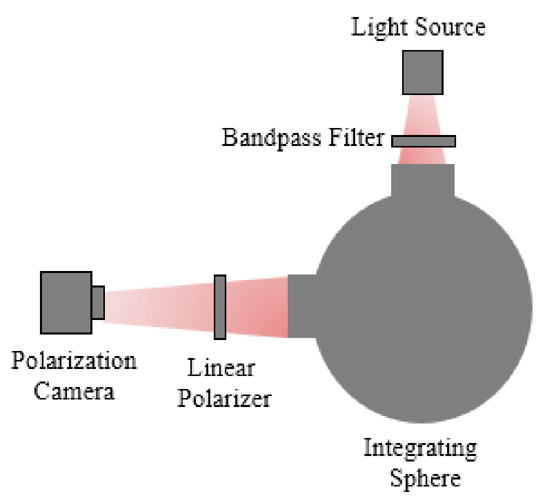

Figure 2.2 Calibration setup for the polarization camera

Camera calibration results are shown in Figure 2.3 and Figure 2.4. When a narrowband light source is used, the light reflected from the micro-polarizer and the sensor may introduce interference patterns, as shown in Figure 2.3(a). Figure 2.3(b) shows that the calibration method can effectively correct the background interference pattern. Figure 2.4 shows the interferogram of a diamond turned flat copper. The background pattern is removed, and the interference fringes are normalized after calibration, demonstrating that the calibration method is effective.

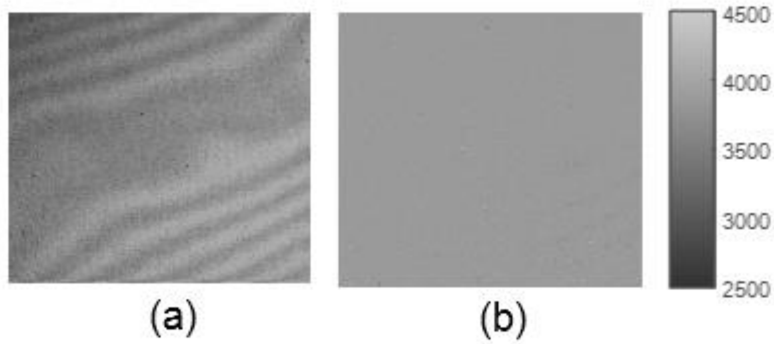

Figure 2.3 Calibration result of polarization camera with uniform illumination. (a) Image before calibration and (b) image after calibration

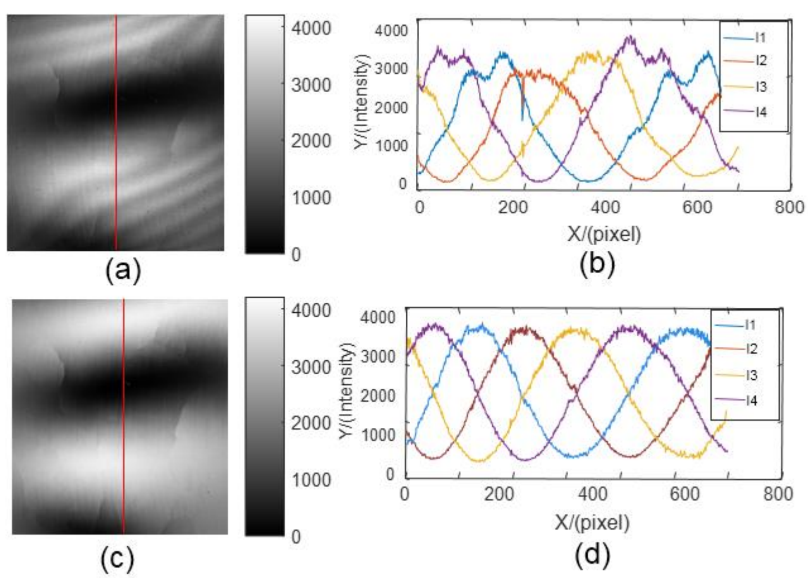

Figure 2.4 Calibration results of a diamond turned flat copper surface. Interferogram (a) before and (c) after calibration. Irradiance distribution in four channels of polarization (b) before and (d) after calibration.

2.3 System Design

This SDIS is a combination of a Linnik interference microscope and a Twyman-Green laser interferometer. The schematic diagram of the system is shown in Figure 2.5. A HeNe laser and a LED is used as light sources. The HeNe laser with a wavelength of 632.8 nm is used for measuring surface form, and the LED with a center wavelength of 630 nm and bandwidth of 10 nm is used for measuring surface roughness. A beam expander is inserted in the laser beam to increase the beam size of the laser, which leads to a 20 mm beam size after the beam expander. The light from these two light sources is combined by a beam splitter (BS), then passes through a linear polarizer with the transmission axis oriented at 45° to the x-axis. The relative irradiance between the test and reference arms can be adjusted by rotating the polarizer to obtain the optimal fringe contrast. After reflected by a folding mirror, the p and s polarized beams of the incident linear polarized beam are separated by a polarizing beam splitter (PBS). The p and s polarized beams are transmitted and reflected into the reference and test arms. The polarization of both beams rotates 90° after passing twice through a quarter-wave plates (QWP) with the fast axis at 45° relative to the x-axis, which allows the returning beams to go to the observing screen. Two identical long working distance microscope objective (Edmund M Plan Apo 10X) with 0.28 NA are used for matching the optical paths, forming a Linnik interferometer. Another QWP with its fast axis at 45° is placed in front of the camera, transforming the two orthogonal linear polarized beams to opposite circular polarized beams. A pixelated polarization camera (4D Technology, Inc.) is used to capture the four phase-shifted interferograms simultaneously.

This SDIS is mounted on a linear translation stage on the DMT. The working mode can be switched by removing and remounting the objective in the reference arm. In interferometer mode, the laser is used as the light source. The objective in the reference arm is removed, forming a Twyman-Green laser interferometer. The test sample with different radius of curvature can be measured by choosing objectives with different F-number in the test arm. As for the interference microscope mode, the objective in reference is remounted. The LED is used as the light source to reduce the coherent noise.

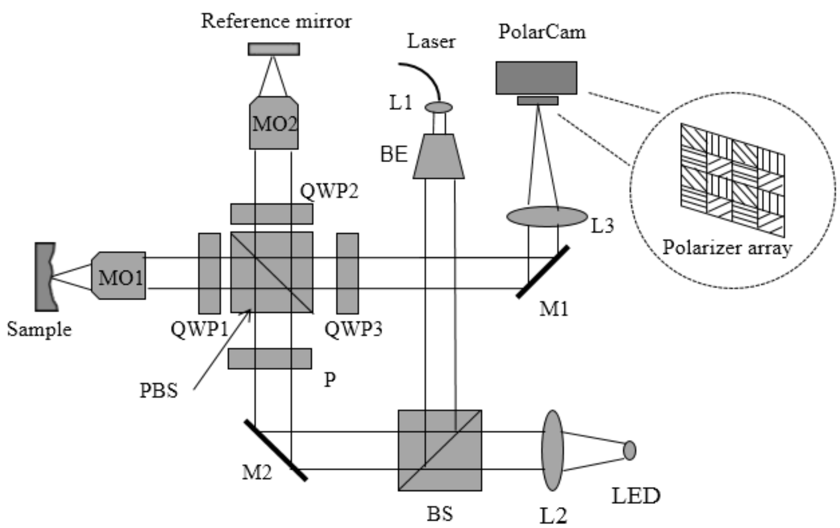

Figure 2.5 Snapshot dual-mode interferometric system: QWP1 - QWP3: quarter wave plates; P: polarizer; BS: non-polarizing beam splitter; PBS: polarizing beam splitter; BE: beam expander; L1 - L3: lenses; M1 – M2: mirrors; MO1 - MO2: microscope objectives.

The Jones vectors of the test and reference beams before the polarization camera can be written as:

$$\begin{aligned} E_T &= Q_3 * T_{pbs} * Q_1' * M_T * Q_1 * R_{pbs} * E_i \\ E_R &= Q_3 * R_{pbs} * Q_2' * M_R * Q_2 * T_{pbs} * E_i \end{aligned} \tag{2.7}$$

where $E_i = \frac{1}{\sqrt{2}}\begin{bmatrix}1\\1\end{bmatrix}$ is the incident Jones vector after passing through the polarizer orientated at 45°. Q_1, Q_1', Q_2, Q_2' and Q_3 are the Jones matrix of QWP1, QWP2 and QWP3, defined as $Q = \begin{bmatrix} cos^2\theta + isin^2\theta & (1-i)cos\theta sin\theta \\ (1-i)\cos\theta sin\theta & sin^2\theta + icos^2\theta \end{bmatrix}$ where θ is the fast axis angle of the QWP to the horizontal axis, T_{pbs} and R_{pbs} are the transmittance and reflectance Jones matrix of the PBS, defined as $T_{pbs} = \begin{bmatrix} T_p & 0 \\ 0 & T_s \end{bmatrix}$, $R_{pbs} = \begin{bmatrix} R_p & 0 \\ 0 & R_s \end{bmatrix}$, T_p and T_s are the transmittance factors of the PBS for p and s light, R_p and R_s are the reflectance factors for p and s light. M_T is the Jones matrix of the test sample, defined as $M_T = e^{i\phi}\begin{bmatrix} 1 & 0 \\ 0 & -1 \end{bmatrix}$, and M_R is the Jones matrix of a dielectric mirror, defined as $M_R = \begin{bmatrix} 1 & 0 \\ 0 & -1 \end{bmatrix}$.

Ideally, E_T and E_R are circular polarized with the opposite direction, which can be simplified as $\frac{1}{\sqrt{2}}\begin{bmatrix}1\\i\end{bmatrix}e^{i\varphi}$ and $\frac{1}{\sqrt{2}}\begin{bmatrix}1\\-i\end{bmatrix}$ respectively. The superposition of the test and reference waves generates fringe patterns after passing through different micro-polarizers. The irradiance of the interferograms of each superpixel are shown as:

$$\begin{aligned} I_1 &= I_T + I_R + 2\sqrt{I_T I_R}\cos(\phi) \\ I_2 &= I_T + I_R - 2\sqrt{I_T I_R}\sin(\phi) \\ I_3 &= I_T + I_R - 2\sqrt{I_T I_R}\cos(\phi) \\ I_4 &= I_T + I_R + 2\sqrt{I_T I_R}\sin(\phi) \end{aligned} \tag{2.8}$$

And the four-step phase-shifting algorithm can be used to calculate the phase information.

2.4 Error Analysis

The environmental error is reduced since the SDIS takes measurement simultaneously. However, the components errors [41], as an important error source, need to be considered. The components errors include the retardance and orientation of the QWP, the diattenuation and orientation of the micro-polarizer array, misalignment between micro-polarizer array and CCD pixels, and non-ideal PBS.

2.4.1 Quarter Waveplate Related Errors

In the theoretical calculation, the retardance of the QWP is exactly $\lambda/4$, and the orientation of the QWP is perfectly aligned along 45°. To calculate the effect of the QWP error, the Jones matrix of the QWP in Equation 2.7 can be modified as:

$$Q = R(-45^\circ - \varepsilon)\begin{pmatrix} 1 & 0 \\ 0 & e^{i(\pi/2+\delta)} \end{pmatrix} R(45^\circ + \varepsilon) \tag{2.9}$$

where $R(\theta) = \begin{pmatrix} \cos\theta & \sin\theta \\ -\sin\theta & \cos\theta \end{pmatrix}$ is the rotation matrix, ε is the QWP orientation error, and δ is the QWP retardance error. The orientation and retardance error is shown in Figure 2.6. For the case of QWP orientation, the result is not critically affected. The orientation of QWP1 and QWP2 only changes the relative irradiance between test and reference beams, which could be compensated by rotating the polarizer. But the orientation of QWP3 causes the output beams elliptical polarized, which may introduce some phase error. Figure 2.6(a) shows the phase error caused by 5° QWP orientation error of QWP3, producing approximately 0.00025λ peak-to-valley error. The magnitude of this error is pretty small and can be ignored. In Figure 2.6(b), the phase error caused by a $\lambda/10$ retardance error is shown. The peak-to-valley error in the calculated phase is about 0.033λ. This error will be significantly increased with a larger retardance error, especially for the case that the QWP is used for multi-wavelength. So an achromatic zero order QWP is preferred for multi-wavelength measurement. Since all these errors are phase relative, several measurements can be made and averaged to reduce this phase error.

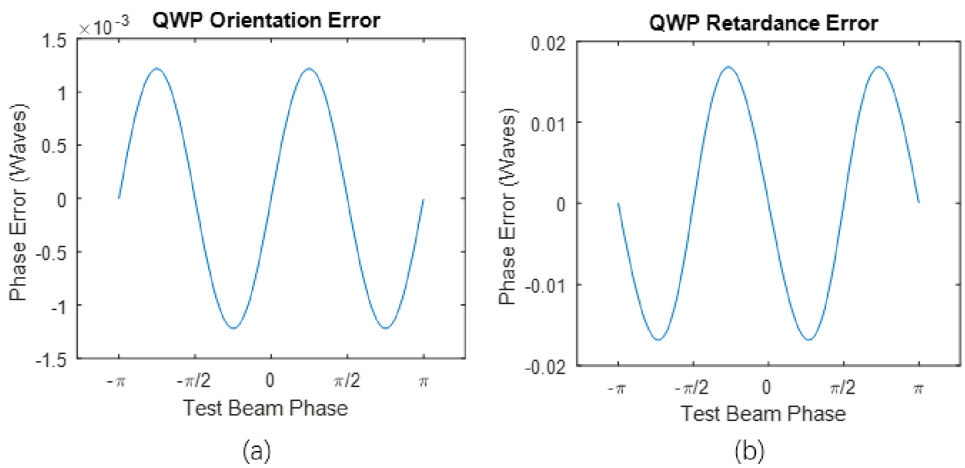

Figure 2.6 Phase error due to QWP error. (a) phase error caused by QWP orientation, (b) phase error caused by QWP retardance

2.4.2 Polarizer Related Errors

Since the phase-shift produced for each pixel is dependent on the linear polarizer and the irradiance at the pixel, any error in the polarizer may cause phase error. The main errors in the polarizer include orientation error, diattenuation error, and misalignment between micro-polarizer array and detector pixels.

The phase-shift value is twice as the orientation angle of the linear polarizer. Thus the orientation error in the linear polarizer would cause a phase-shift error. If all polarizers are orientated with the same amount error, the calculated phase remains unchanged. If only one of the polarizers contains such error, then a phase-shift error is introduced. Figure 2.7(a) shows the phase error caused by a 0.5° polarizer orientation error in 0° polarizer. In the real micro-polarizer array fabrication process, this error is even smaller, leading to a negligible phase error.

The diattenuation describes the amount of light passing through the polarizer. A perfect linear polarizer exhibits a diattenuation of 1.0. If the polarizers have the same diattenuation within a superpixel, the calculated phase remains the same since all irradiance multiplies a same value. However, if only one polarizer has a diattenuation drop within the superpixel, then the calculate phase would generate a phase dependent error. Figure 2.7 (b) shows the phase error caused by the diattenuation error. The diattenuation of 0° polarizer is 0.9, while others remain 1. Since the diattenuation only influences the irradiance by a scale vector, this error can be reduced by normalizing the interferograms and camera calibration.

Another error in the polarizer camera is the misalignment between micro-polarizer and camera pixels, as shown in Figure 2.8. The new irradiance on a certain pixel of the camera sensor is a linear combination of the previous irradiance I_1, I_2, I_3, and I_4:

$$\begin{bmatrix} I_1' \\ I_2' \\ I_3' \\ I_4' \end{bmatrix} = \begin{bmatrix} a & b & c & d \\ b & a & d & c \\ c & d & a & b \\ d & c & b & a \end{bmatrix} * \begin{bmatrix} I_1 \\ I_2 \\ I_3 \\ I_4 \end{bmatrix} \tag{2.10}$$

$$\varphi = \arctan \frac{I_4' - I_2'}{I_1' - I_3'} \tag{2.11}$$

where I_1', I_2', I_3', and I_4' are the irradiance on each subpixel after considering the misalignment, a is the percentage of the primary polarized state, b, c, and d are the percentage of the other polarized states. For a=0.855, b=0.095, c=0.005, d=0.045, the phase error is shown in Figure 2.7(c). These values are just used for simulation and not represent the real micro-polarizer array offsite.

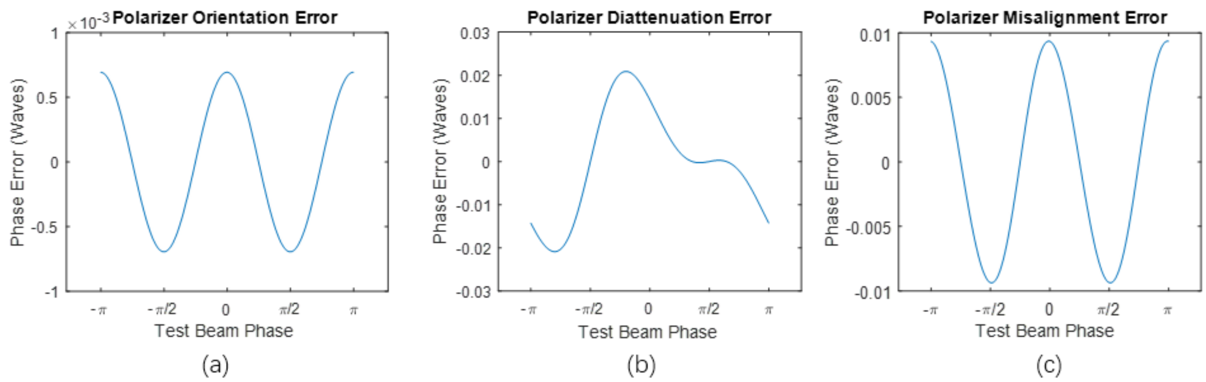

Figure 2.7 Phase error due to polarizer error

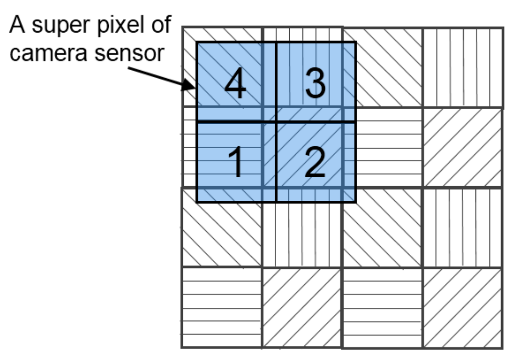

Figure 2.8 Misalignment between micro-polarizer and camera sensor

2.4.3 Polarizing Beam Splitter Related Error

In theoretical calculation, we assume a perfect PBS, which 100% transmits p-polarized light and 100% reflects s-polarized light. However, such a perfect PBS does not exist in real life. For a non-ideal PBS (Thorlabs CMM1-PBS251) with 96.9% transmission for P-polarized light and 0.07% for S-polarized light, assume there is no energy loss in PBS, then the transmittance and reflectance matrices of the PBS are $T_{pbs} = \begin{bmatrix} 0.984 & 0 \\ 0 & 0.026 \end{bmatrix}, R_{pbs} = \begin{bmatrix} 0.176 & 0 \\ 0 & 0.999 \end{bmatrix}$. The phase error caused by the error of the non-ideal PBS is shown in Figure 2.9.

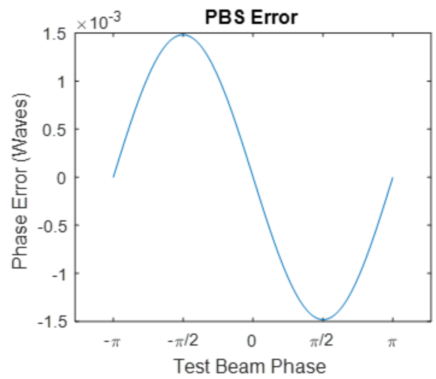

Figure 2.9 Phase error due to non-ideal PBS

These phase related errors caused by optical components can be reduced by camera calibration and Lissajous ellipse fitting algorithm [42-44]. Besides the phase related errors, other error sources like system error and alignment error can degrade the test accuracy as well, which can be subtracted after calibration.

2.5 Experiment Results

To demonstrate the performance of our SDIS, this system was built and tested on a Moore Nanotech 350FG diamond turning machine (DTM). As shown in Figure 2.10(a), the SDIS was mounted on a linear translation stage between two diamond cutting tool holders. Before measurement, the optical axis of the SDIS was aligned parallel with the spindle axis. Two objectives were removed from the system and the laser source was turned on. Another flat mirror was fabricated and mounted on the spindle. Thus the tilt between the SDIS and the spindle axis can be minimized by nulling the interferogram. Figure 2.10(b) shows the components in the system. The dimension of the system is 12x12x3 inches.

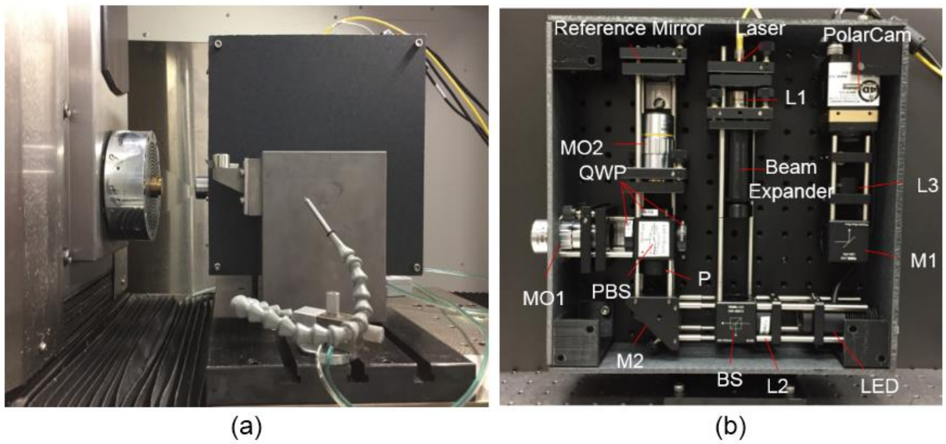

Figure 2.10 (a) SDIS mounted on diamond turning machine. (b) SDIS layout

Two sets of samples were fabricated by DTM and measured by SDIS on the DTM. Then these samples were measured by commercial interferometers in off-line condition for comparison. In off-line measurement, the surface form was measured by a Zygo Verifire^{TM} laser interferometer, and the surface roughness was measured by a Zygo NewView 8300 optical surface profiler. The first sample was a copper surface with a 50 mm radius of curvature and 25 mm diameter. Figure 2.11(a) shows the four phase-shifted interferograms of the copper surface in the laser interferometer mode. The measurement results in SDIS and Zygo laser interferometer are shown in Figure 2.11(b) and Figure(c), while a line profile comparison is shown in Figure 2.11(d). For surface roughness, the measurement area is about 800 μm x 800 μm at the center of the sample. One of the four interferograms is shown in Figure 2.12(a). The comparison of the measurement results is shown in Figure 2.12(b)-(d). The surface peak-to-valley (PV) and root mean square (RMS) are recorded in Table 2.1. The PV value is not recorded in the interference microscope mode due to its high dependence on the cutting debris.

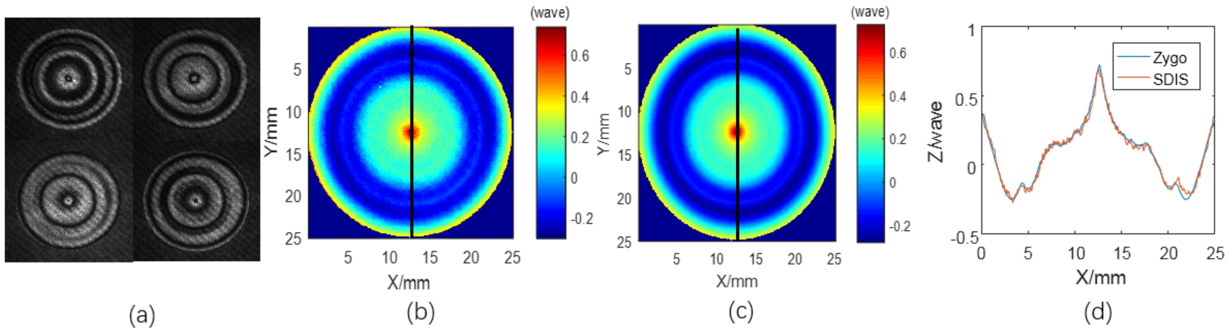

Figure 2.11 Surface form measurement of a diamond copper surface: (a) four phase shifted interferograms, (b) SDIS measurement, (c) off-line measurement, and (d) line profile comparation

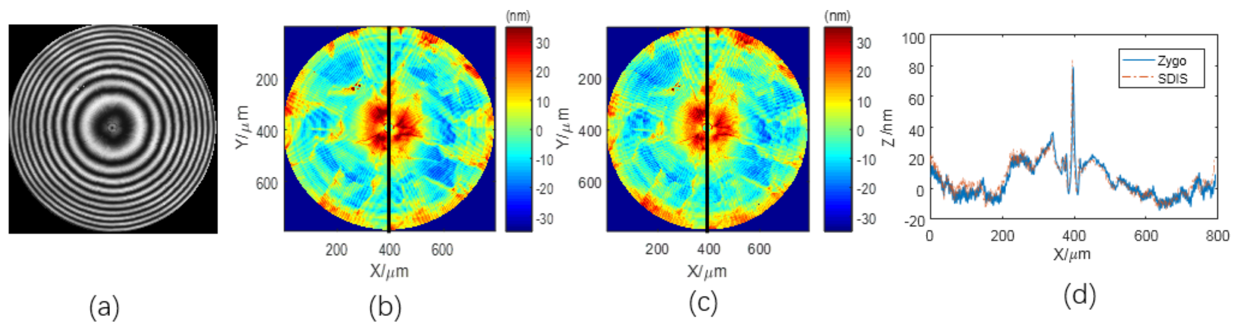

Figure 2.12 Surface roughness measurement of a diamond copper surface: (a) interferogram in SDIS, (b) SDIS measurement, (c) off-line measurement, and (d) line profile comparation

Another sample was fabricated with Polymethyl methacrylate (PMMA) with the same radius of curvature and diameter of the copper surface. Since the reflectance of the PMMA surface is much lower than the reference mirror, the orientation of the linear polarizer must be adjusted to achieve better fringe contrast. Figure 2.13 shows the surface form measurement of this PMMA surface, and Figure 2.14 shows the surface roughness measurement. Some speckly patterns can be seen in the measurement results due to the deeper tool marks and lower reflectance of the PMMA surface.

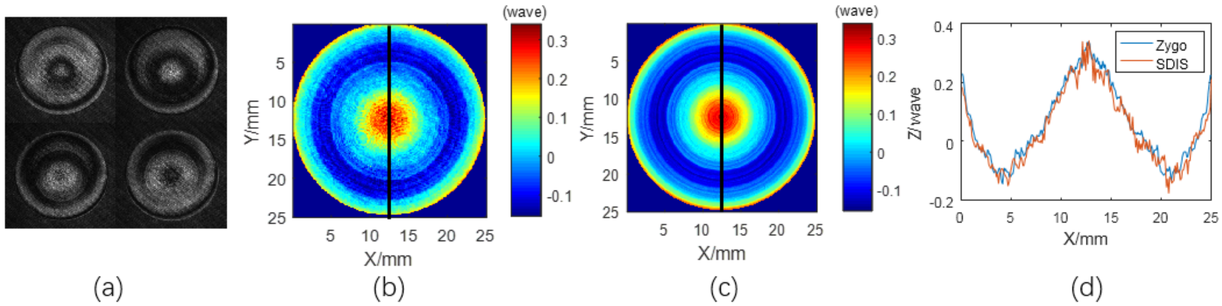

Figure 2.13 Surface form measurement of a PMMA surface: (a) four phase shifted interferograms, (b) SDIS measurement, (c) off-line measurement, and (d) line profile comparation

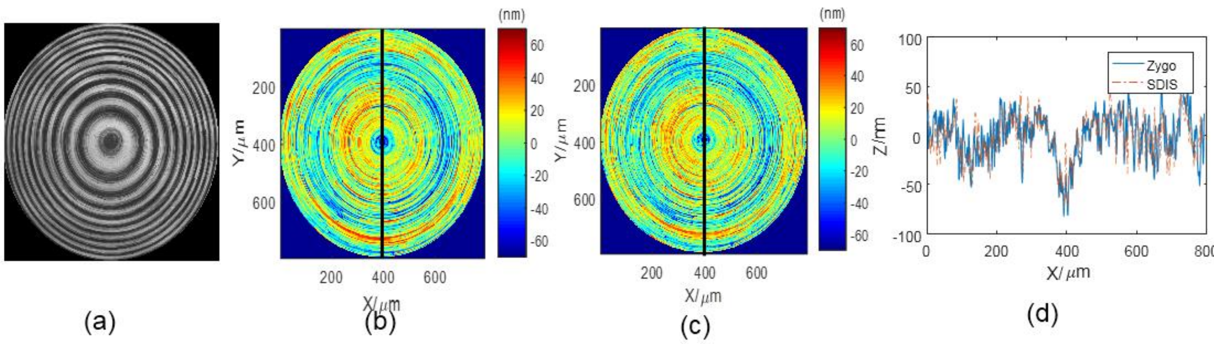

Figure 2.14 Surface roughness measurement of a PMMA surface: (a) interferogram in SDIS, (b) SDIS measurement, (c) off-line measurement, and (d) line profile comparation

Table 2-1 Comparison of SDIS and commercial interferometer

		Surface Form		Surface Roughness
		PV (λ)	RMS (λ)	RMS (nm)
Copper surface	Zygo interferometer	1.002	0.182	10.35
	SDIS	1.038	0.184	10.62
PMMA surface	Zygo interferometer	0.494	0.552	20.87
	SDIS	0.101	0.113	21.02

2.6 Conclusion

In this chapter, we proposed a compact, snapshot dual-mode interferometric system for on-machine metrology to measure surface form and surface roughness. A pixelated polarization camera was applied to achieve the simultaneous phase-shifting. We proposed a calibration method for the polarization camera. And components error in this system was analyzed. This SDIS is insensitive to environment noise like vibration and air turbulence. Thus it provides a power and portable tool for the real-time and on-machine surface characteristics.

Chapter 3 Snapshot Multi-wavelength Interference Microscope

3.1 Introduction

In recent years, interference microscopes are widely used in optical metrology and biomedical measurement for the quantitative characterization of micro-topographical features of the sample [45]. One limitation of the phase-shifting interference microscopes is that the height difference between two adjacent points must be less than $\lambda/4$. Otherwise, there would be an ambiguity problem during the phase unwrapping process. In order to overcome this limitation and increase the measurement range, different methods have been developed. Vertical scanning interferometer is one solution [45-49], which uses a broad range light source and the coherence-peak-sensing approach to extract surface information. Multi-wavelength interferometer [50-52] is another approach that extending the height difference limitation, which uses the combination of multi-wavelength to get precise surface measurement and large dynamic range. However, both methods have the same issue of slow measurement speed. The vertical scanning interferometer needs to scan the surface from the lowest point to the highest point, and the multi-wavelength interferometer needs to obtain each wavelength sequentially. To increase the measurement speed, several multi-wavelength interferometers have been developed. A phase-shifting multi-wavelength dynamic interferometer with polarization masked camera wave developed to obtain multi-wavelength data sequentially by a high speed polarization camera [53]. Another solution is the parallel interferometry with multiple phase masked CCD arrays [54, 55], which could obtain fast measurement but increases the difficulty in alignment and the cost of the system. Other solutions, including digital holography microscopy [56, 57] and off-axis interferometry [58], use the frequency-domain methods, leading to the lack of spatial information.

In this chapter, we proposed a snapshot multi-wavelength interference microscope (SMIM) to achieve high speed measurement of large vertical range discontinuous structure and surface roughness [59]. This SMIM uses a custom CMOS camera with a linear micro-polarizer array and Bayer filters [60] to achieve simultaneous measurement of three different colors. Due to the combination of micro-polarizer array and Bayer filters, 4 x 4 pixels form one superpixel, which has different polarization and color information. The spatial resolution is reduced by this combination, which can be partially addressed by image interpolation. Sensor with more and small pixels can also be used to improve the performance. By using this color polarization camera, phase-shifted interferograms in different color channels are captured in a single shot. Thus high speed and large vertical measurement range can be achieved, which makes this system suitable for dynamic measurement.

3.2 Multi-wavelength Metrology

One limitation in a single wavelength interferometer is that the height difference between two adjacent points must be less than $\lambda/4$, where λ is the wavelength of the light source. If the height is larger than $\lambda/4$, a 2π ambiguity would be introduced during the phase unwrapping process. Using the multi-wavelength method, the height can be determined by combining the phase values at different wavelengths.

The measurement range increases as the increasing of the equivalent wavelength, given by:

$$\Lambda_{12} = \frac{\lambda_1 \lambda_2}{|\lambda_1 - \lambda_2|} \tag{3.1}$$

If one surface is measured with two wavelengths λ_1 and λ_2, the measurable step height H can be extended from $\lambda_1/4$ to $\Lambda_{12}/4$. The height can be calculated with the equivalent wavelength and equivalent phase [61]

$$H_{12} = \frac{\Lambda_{12}}{2} \cdot \frac{\Phi}{2\pi} \tag{3.2}$$

where the equivalent phase $\Phi = \phi_1 - \phi_2$ is the difference between the two phases measured in each wavelength.

The problem of using the equivalent wavelength is that the phase error also increases by a factor of Λ_{12}/λ_1, which influences the accuracy of surface roughness measurement. In order to reduce this phase error, the fringe order method is used [62]. In this method, the fringe order N_1 of λ_1 is determined with the height calculated by the equivalent wavelength. Thus the height with less error can be calculated by:

$$\begin{aligned} H_1 &= \frac{\lambda_1}{2}\left(\frac{\phi_1}{2\pi} + N_1\right) \\ N_1 &= round\left(\frac{2H_{12}}{\lambda_1}\right) \end{aligned} \tag{3.3}$$

where *round* is the nearest integer. By using this fringe order method, the surface can be measured with a large dynamic range to the order of $\Lambda_{12}/4$ while keeps the surface error as low as a single wavelength interferometer. In order to get the correct fringe order, the phase noise in ϕ_1 must be smaller than $\lambda_1/(4\Lambda_{12})$ [63]. A longer equivalent wavelength not only leads to larger measurement, but also to a tighter noise limit.

The equivalent wavelength method can be extended to more wavelengths. For the case of three wavelengths, the equivalent wavelength can be calculated by:

$$\Lambda_{12-23} = \Lambda_{12}\Lambda_{23} / \left|\Lambda_{12} - \Lambda_{23}\right| \tag{3.4}$$

where $\Lambda_{12} = \lambda_1\lambda_2 / \left|\lambda_1 - \lambda_2\right|$ is the equivalent wavelength of λ_1 and λ_2, and $\Lambda_{23} = \lambda_2\lambda_3 / \left|\lambda_2 - \lambda_3\right|$ is the equivalent wavelength of λ_2 and λ_3. And the height calculated with three wavelength is:

$$H_{12-23} = \frac{\Lambda_{12-23}}{2} \cdot \frac{(\phi_1 - \phi_2) - (\phi_2 - \phi_3)}{2\pi} \tag{3.5}$$

where ϕ_1, ϕ_2 and ϕ_3 are the phase measured with λ_1, λ_2 and λ_3.

The maximum phase noise limit can be increased by calculating the fringe order separately instead of calculating the fringe order of λ_1 directly. The fringe order of Λ_{12} based on $H_{12\text{-}23}$ can be calculated firstly, and then the final step height H_1 is obtained from H_{12}. Thus the maximum phase noise limit can be extended from $\lambda_1/(4\Lambda_{12\text{-}23})$ to $\lambda_1/(4\Lambda_{12})$ or $\Lambda_{12}/(4\Lambda_{12\text{-}23})$.

3.3 Color Polarization Camera

3.3.1 Camera Design

The custom color polarization camera is a division-of-focal-plane RGB linear Stokes camera constructed by 4D Technology. This camera is realized by applying a wire-grid micro-polarizer array onto the traditional RGB Bayer sensor array, as shown in Figure 3.1. By using this color polarization camera, the linear polarization information and color information of any sample can be captured within a single shot. The CMOS imaging sensor in this custom camera comprises 1200 x 1600 total pixels, in which 1082 x 1312 pixels are usable. The pitches of the Bayer array and micro-polarizer arrays are 4.5 μm and 9 μm, and the frame rate is up to 54fps. The parallel transmission of the micro-polarizer array is >70% over the visible band.

In nowadays, color polarization cameras are commercially available, integrated with the Sony IMX250MYR polarized color sensor, as shown in Figure 3.2. This sensor with a pixel size of 3.45 μm and frame rates of up to 24 fps is based on the IMX250Sony Pregius CMOS color sensor with a polarizing filter added to the pixel [64]. The sensor design of Sony IMX250MYR is not the same as our polarization camera, but the principle is the same.

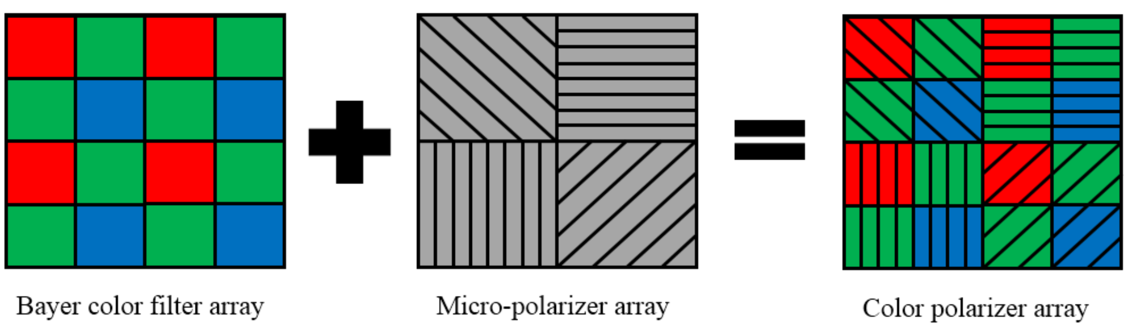

Figure 3.1 Our custom color polarization camera.

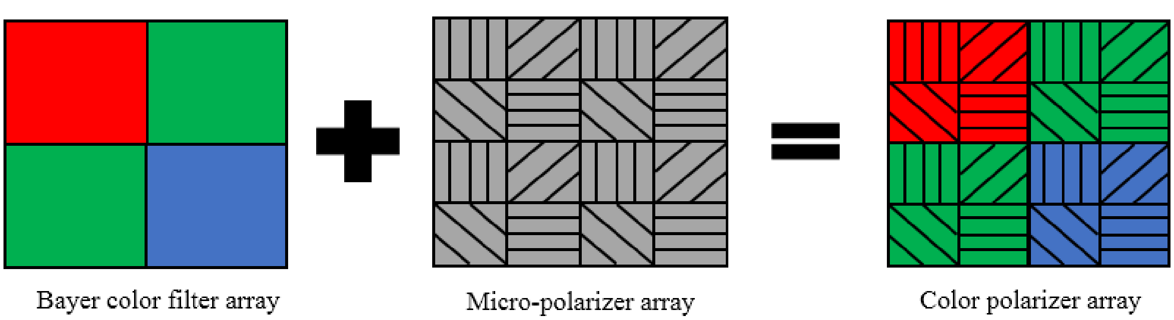

Figure 3.2 Sony IMX250MYR polarized color sensor

3.3.2 Color Polarization Camera Calibration

As the key component of the snapshot multi-wavelength interference microscope, the color polarization camera must be calibrated to ensure the accurate measurement. The calibration method is modified by the mono-polarization camera calibration method. However, since the color polarization camera contains both Bayer color filter and micro-polarizer array, color crosstalk and polarization crosstalk should also be considered during the calibration process [60], comparing to the mono-polarization camera calibration method.

During the camera calibration, missing irradiance due to the use of superpixel is recovered by a linear-spline interpolation. The incident Stokes vectors for red (R), green (G), and blue (B) are defined as:

$$\begin{aligned} \overrightarrow{S_R} &= [S_{R0}\ S_{R1}\ S_{R2}\ S_{R3}]^T \\ \overrightarrow{S_G} &= [S_{G0}\ S_{G1}\ S_{G2}\ S_{G3}]^T \\ \overrightarrow{S_B} &= [S_{B0}\ S_{B1}\ S_{B2}\ S_{B3}]^T \end{aligned} \tag{3.6}$$

where S_{R3}, S_{G3}, and S_{B3} are the circular parts in the Stokes vector of RGB light. Since this camera only measures linear polarized light and the circular part is 0 during the experiment, the input Stoke vector can be simplified as:

$$\begin{aligned} \overrightarrow{S_R} &= [S_{R0}\ S_{R1}\ S_{R2}]^T \\ \overrightarrow{S_G} &= [S_{G0}\ S_{G1}\ S_{G2}]^T \\ \overrightarrow{S_B} &= [S_{B0}\ S_{B1}\ S_{B2}]^T \end{aligned} \tag{3.7}$$

Thus the relationship between recorded irradiance *I*, the analyzer matrix *W*, and the input Stokes vector *S* can be written as:

$$\begin{gathered} I = WS \\ \begin{bmatrix} \vec{I}_R \\ \vec{I}_G \\ \vec{I}_B \end{bmatrix} = W \cdot \begin{bmatrix} \vec{S}_R \\ \vec{S}_G \\ \vec{S}_B \end{bmatrix} \end{gathered} \tag{3.8}$$

where $\overrightarrow{I_R} = [I_{R0}\ I_{R1}\ I_{R2}\ I_{R3}]^T$, $\overrightarrow{I_G} = [I_{G0}\ I_{G1}\ I_{G2}\ I_{G3}]^T$, and $\overrightarrow{I_B} = [I_{B0}\ I_{B1}\ I_{B2}\ I_{B3}]^T$ are the irradiance values for the RGB channels captured by color polarization camera, 0, 1, 2, and 3 are corresponding to 0°, 45°, 90°, and 135° linear polarization states.

The setup for the calibration process is shown in Figure 3.3. RGB LEDs with bandpass filters are used as light sources. The bandwidth of the bandpass filters is 10 nm with center wavelengths at 460 nm, 540 nm, and 630 nm separately. Only one LED is turned on at each time during the color crosstalk calibration. An integration sphere is used to produce uniform unpolarized illumination. The incident Stoke vector for a given wavelength is

$$\vec{S} = [S_0\ S_1\ S_2]^T = [S_0\ S_0\cos\theta\ S_0\sin\theta]^T \tag{3.9}$$

where θ is the rotation angle of the linear polarizer. The linear polarizer is rotated 18 times with a step of 10° for each wavelength. There are a total of 54 measurements used to calculate the analyzer matrix *W*.

$$W = I \cdot S^+ = \begin{bmatrix} I_{R0}^1 & \cdots & I_{R0}^{54} \\ \vdots & \ddots & \vdots \\ I_{B3}^1 & \cdots & I_{B3}^{54} \end{bmatrix} \cdot \begin{bmatrix} S_{R0}^1 & \cdots & S_{R0}^{54} \\ \vdots & \ddots & \vdots \\ S_{B2}^1 & \cdots & S_{B2}^{54} \end{bmatrix}^+ \tag{3.10}$$

where S^+ is the pseudo inverse of input Stokers vector S. The ideal analyzer matrix for each wavelength that transforms Stokes vector into linear polarization state at 0°, 45°, 90°, and 135° is

$$W_{ideal} = \frac{1}{2} \begin{bmatrix} 1 & 1 & 0 \\ 1 & 0 & 1 \\ 1 & -1 & 0 \\ 1 & 0 & -1 \end{bmatrix} \tag{3.11}$$

The correction matrix C for each pixel is:

$$C = \begin{bmatrix} W_{ideal} & 0 & 0 \\ 0 & W_{ideal} & 0 \\ 0 & 0 & W_{ideal} \end{bmatrix} \cdot W^{+} \tag{3.12}$$

And the corrected irradiance $\tilde{I}$ for each pixel can be calculated by:

$$\tilde{I} = C \cdot I \tag{3.13}$$

After calibration, the PRNU and FPN noise are minimized, as well as the color crosstalk between red, green, and blue channels.

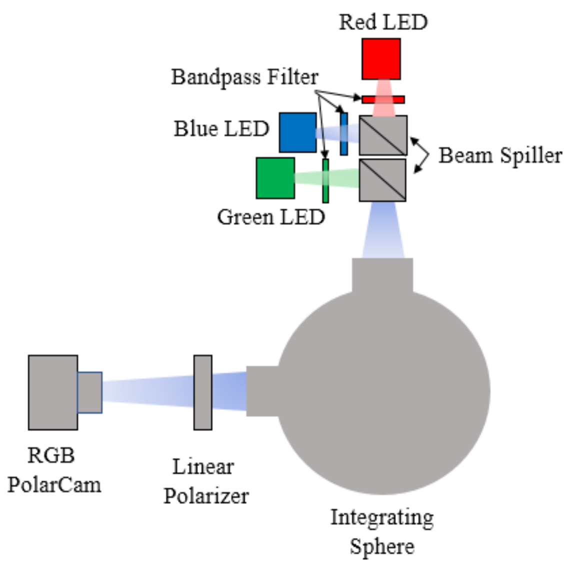

Figure 3.3 Color polarization camera calibration setup

3.4 Three Wavelength Interference Microscope

3.4.1 System Design

The system setup is shown in Figure 3.4. The system is built based on a Linnik configuration interference microscope. Three LEDs in red, green, and blue color channels are used as light sources to provide multi-wavelength illumination. In front of each LED, a bandpass filter is inserted to narrow the bandwidth of the light source, leading to longer coherent length. The center wavelengths of the bandpass filters are 460 nm, 540 nm, and 630 nm with a bandwidth of 10 nm. Two achromatic quarter wave plates (QWP) with the fast axis at 45° relative to the x-axis are used in the test and reference arms. Two identical long working distance microscope objectives (Edmund M Plan Apo 10X) with NA 0.28 are used for matching the optical paths, forming a Linnik interferometer. Another achromatic QWP with its fast axis at 45° is placed in front of the camera, transforming the two orthogonal linear polarized beams to opposite circular polarized beams. A custom color polarization camera with a wire-grid micro-polarizer array on the traditional RGB Bayer filter array is utilized to record phase-shifted interferograms in RGB channels in a single shot. Due to a small misalignment between the wire-grid micro-polarizer array and the RGB Bayer filter array, one of the G channel has lager polarization crosstalk error that the other in sub-superpixel [60]. Thus only half of the G channel is used in the calculation. The phase in red, green, and blue spectrum can be calculated by a four-step phase-shifted algorithm:

$$\tan(\phi_R) = \frac{I_{R3} - I_{R1}}{I_{R0} - I_{R2}}$$
$$\tan(\phi_G) = \frac{I_{G3} - I_{G1}}{I_{G0} - I_{G2}} \tag{3.14}$$
$$\tan(\phi_B) = \frac{I_{B3} - I_{B1}}{I_{B0} - I_{B2}}$$

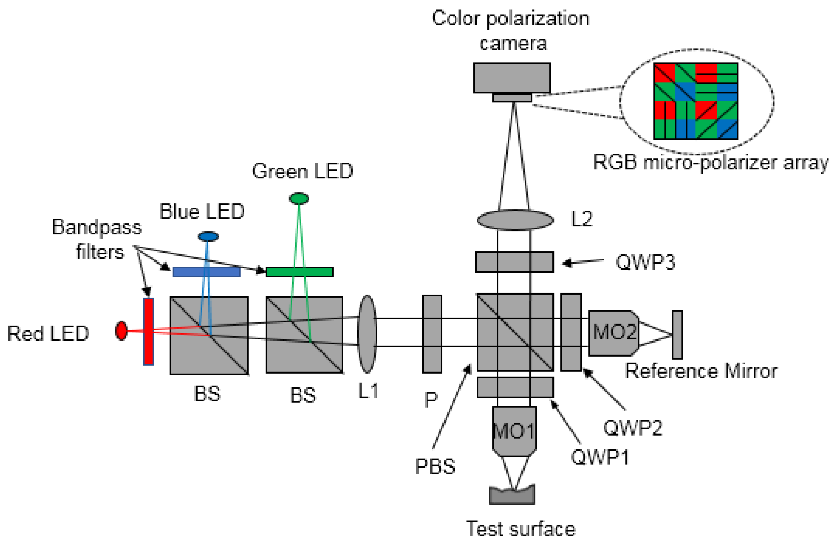

Figure 3.4 System layout of three wavelength interference microscope. BS: beam splitter; L1and L2: lens; P: polarizer; PBS: polarized beam splitter; QWP1, QWP2, and QWP3: achromatic quarter wave plate; MO1 and MO2: microscopy objective; Color polarization camera: a custom camera with a wire-grid micro-polarizer and Bayer color filter

The retardance of the achromatic QWP are 0.2527, 02455, and 0.2460 for B (460 nm), G (540 nm), and R (630 nm), provided by the manufacture Bolder Vison Optik, Inc, as shown in Figure 3.5(a). The phase error caused by achromatic QWP is shown in Figure 3.5(b), which is small enough to be ignored.

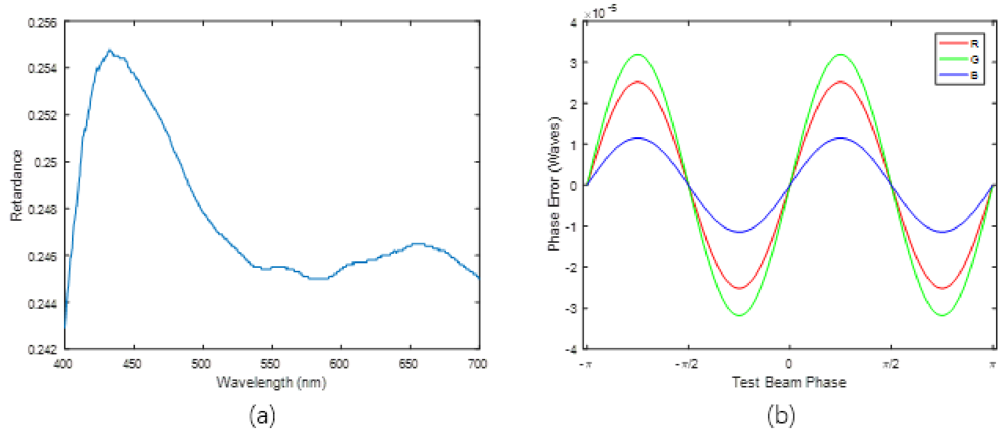

Figure 3.5 (a) Retardance of achromatic QWP given by Bolder Vision Optik, Inc., and (b) phase errors caused by QWP retardance error for RGB LED light.

Based on Equation 3.5, the calculated height is directly related to the effective wavelength. The spectrum of the bandwidth and the center wavelengths of the light sources are important factors that affect the measurement accuracy due to the fact that the Bayer filter in the sensor has a wide transmission bandwidth. In order to obtain a more accurate measurement, bandpass filters with 10 nm bandwidth are used. The LED spectrum is not exactly as symmetry Gaussian distribution, as shown in Figure 3.6. The mean wavelengths must be calibrated before measurement. Generally speaking, a narrower bandwidth has a more accurate extraction of the mean wavelength.

A small shift in a single wavelength would cause a significant difference in the effective wavelength. The mean wavelengths are calibrated by measuring a VLSI step height standard (SHS 4606 Å). Before calibration, the effective wavelength with R (630 nm), G (540 nm), and B (460 nm) is 17388 nm. The calibrated wavelengths are 629.7 nm for the R channel, 540 nm for the G channel, and 459.8 nm for the B channel. Based on Equation 3.4, the effective wavelength is $\Lambda_{12\text{-}23}$ =16888 nm, which means the measurement range for this RGB light source is $\Lambda_{12\text{-}23}/4$ = 4222 nm. The effective wavelength difference before and after calibration is 500 nm, which would significantly influence the measurement accuracy.

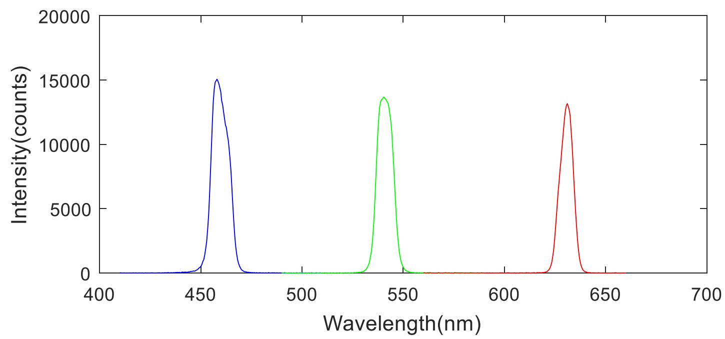

Figure 3.6 Spectrum for RGB LED light source

3.4.2 Experimental Results

To demonstrate the performance of the system, a VLSI step height standard (SHS-1.8 QC) was measured. The measurement results of the VLSI height standard are shown in Figure 3.7. Figure 3.7(a)-(d) are the interferograms recorded in R channel, G channel, and B channel. Figure 3.7(e) shows the 3D surface profile, and Figure 3.7(f) is the line profile. The sample was measured 10 times and averaged in accordance to the definition in ISO 5436-1 standard. The average height is 1720.051 nm, with a standard deviation of 0.54 nm, as shown in Table 3.1. For comparison, the sample was also measured by Zygo NewView 8300 white light interference microscope with a step height of 1722 nm. The corresponding difference between our system and the Zygo interferometer is 1.49 nm. Figure 3.8 is the 3D surface profile measured by Zygo Newview 8300.

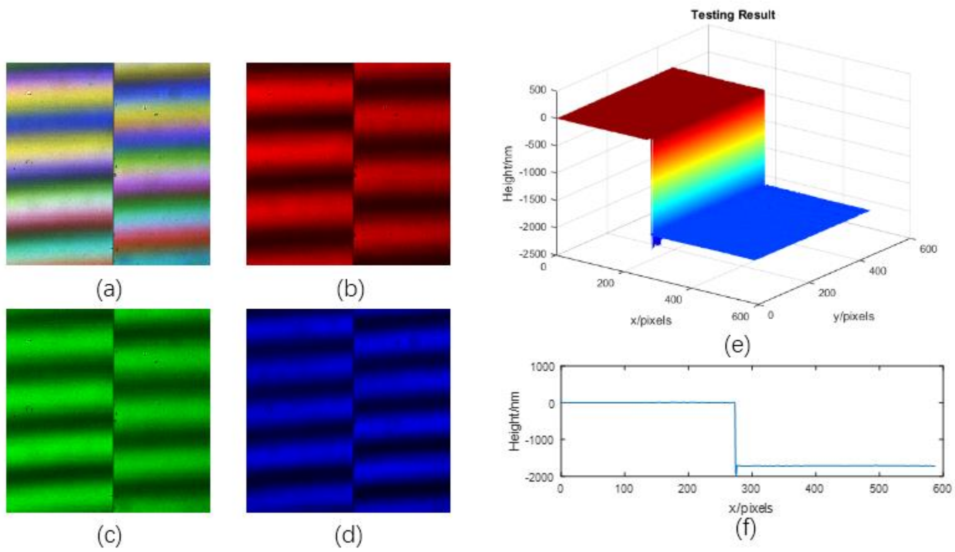

Figure 3.7 VSLI step height measurement. (a)-(d) are RGB, R, G and B interferograms, (e) and (f) are 3D surface and line profile.

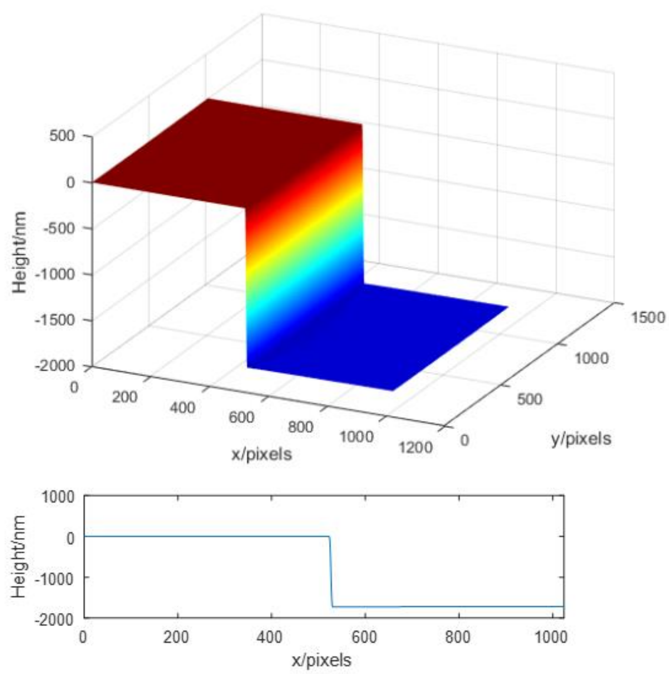

Figure 3.8 VSLI step height measurement by Zygo Newview 8300.

Table 3-1 Measurement results of the VLSI step height standard from the R channel.

No.	Step Height (nm)	No.	Step Height (nm)
1	1721.57	6	1719.98
2	1720.17	7	1719.69
3	1720.91	8	1720.46
4	1720.76	9	1720.07
5	1721.02	10	1720.46
Mean value	1720.51		
Std. Dev.	0.54		

The surface roughness of a diamond turned copper surface was measured and compared with the Zygo interferometer. Figure 3.9 shows the measurement results in red, green, and blue channels. The surface root mean square (RMS) is 8.62 nm in red channel, 8.78 nm in green channel, and 8074 nm in blue channel. This surface was also measured by Zygo Newview 8300 white light interference microscope for comparison. The RMS comparison is shown in Table 3.2. The measured RMS difference between our system and Zygo Newview 8300 is below 0.5 nm, which could be caused by the different bandwidth of light source, residual color crosstalk, and polarization crosstalk.

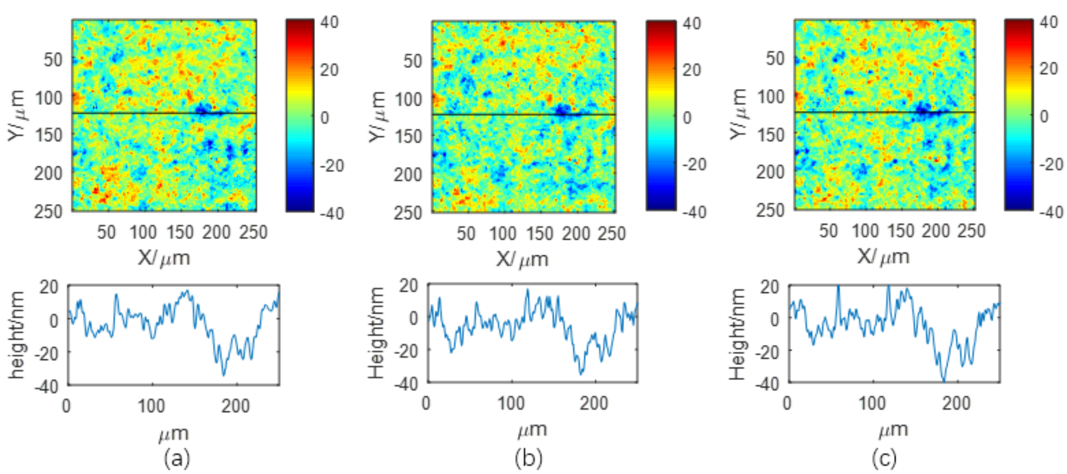

Figure 3.9 Surface topography of a diamond turned copper surface measured by (a) R channel, (b) G channel, and (c) B channel.

Table 3-2 Comparison of RMS between Zygo Newview 8300 and snapshot multi-wavelength interference microscope

	Surface RMS (nm)	Test error (nm)
Zygo Newview 8300	8.36	
R channel	8.62	0.26
G channel	8.78	0.42
B channel	8.74	0.38

3.5 Four Wavelength Interference Microscope

3.5.1 System Design

In a phase-shifting interference microscope, the upper limit of the discontinuity in step height measurement is limited by the coherence length of the light source, the depth of field of the objective, and the equivalent wavelength. In most cases, the equivalent wavelength is the primary limit of the dynamic range. The equivalent wavelength can be increased by reducing the differences of two wavelengths or increasing the number of wavelengths. However, due to the limitation of the Bayer filter, two wavelengths cannot be distinguished if the difference is too small.

By replace in RGB LEDs in Figure 3.4 with lasers at 442.8 nm, 533.3 nm, and 659.8 nm, the equivalent wavelength can be increased to 42 μm, which leads to 10.5 μm measurement range. Since the bandwidth of laser is much shorter than LED, the mean wavelength can be determined more precisely. The problem of using lasers as light sources is that the measurement results are influenced by coherent noise, limitation the accuracy of surface roughness measurement. To reduce this coherent noise, the laser sources are focused onto a rotating diffuser and then coupled into a multi-mode fiber with a 600 μm core and 0.2 NA. Besides, a LED is used as light source together with lasers. Three lasers at λ_1 = 442.8 nm, λ_2 = 533.3 nm, and λ_4 = 659.8 nm with one LED at λ_3 = 629.7 nm are used in this system, as shown in Figure 3.10. Figure 3.11 shows the spectrum of these light sources. By adding the LED in the light sources, one more step is added in fringe order calculation. The equivalent wavelengths in fringe order calculation are $\Lambda_{12\text{-}24}$=42μm, $\Lambda_{12\text{-}23}$=10.4μm, Λ_{12}=2.6μm and λ_3=0.6297μm, leading to a larger maximum phase noise limit from $\lambda_3/(4\Lambda_{12})$=0.0603 waves to $\Lambda_{12}/(4\Lambda_{12\text{-}24})$=0.015 waves. The system is more robust for measuring large step heights due to the larger maximum phase noise limit. The LED is also used for surface roughness reconstructing due to less coherent noise. Thus this system can achieve a long measurement range with 10.5 μm while maintaining high quality surface roughness measurement.

Since the wavelengths of red laser and red LED are similar, these two signals cannot be distinguished in a single shot. This problem can be solved by using one color polarization camera and one mono-polarization camera with color filters to separate these two wavelengths. The laser signal is recorded by the color polarization camera while the LED signal is recorded by the mono-polarization camera. Capturing two images sequentially is another solution. In our experiment, the surface height is reconstructed with two images captured sequentially.

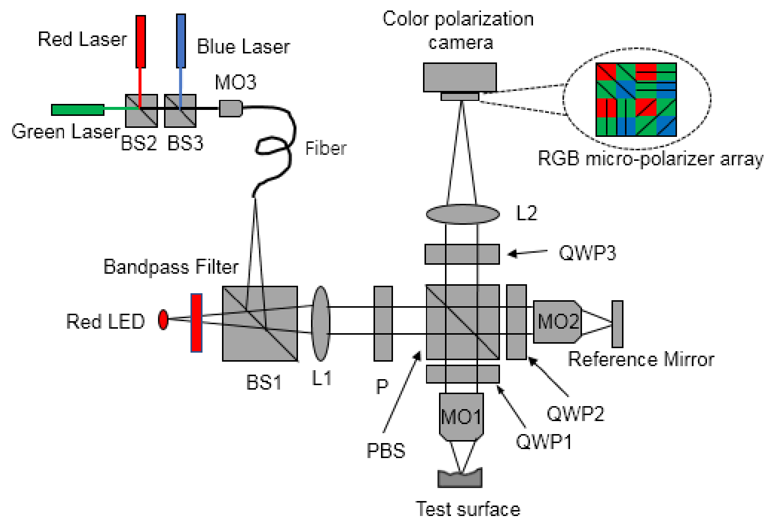

Figure 3.10 System layout with RGB Laser and Red LED as light source

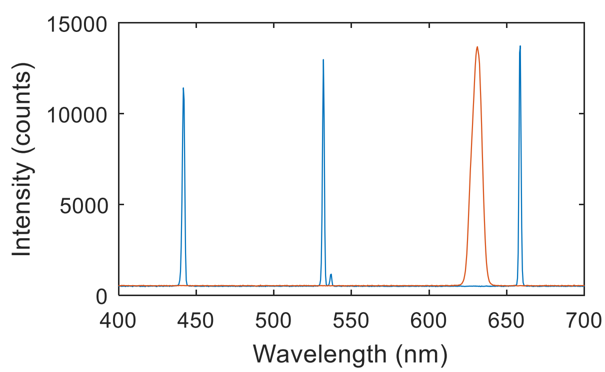

Figure 3.11 Spectrum for RGB laser and RLED.

3.5.2 Experiment Results

A diamond turned copper surface with multiple step heights was tested by our system. This sample contains step heights from 3 μm to 10 μm with a step of 1 μm. Figure 3.12 shows the step height measurement results of 3 μm, 4 μm, and 5 μm. The interferograms of the RGB lasers and the red LED are shown in Figure 3.12(a)-(d). Figure 3.12(e)(f) are the 3D surface profile and line profile.

The surface roughness within the red square in Figure 3.12(c) is measured and compared with Zygo NewView 8300 white light interference microscope, as shown in Figure 3.13. The RMS difference between our system and Zygo NewView 8300 can be caused by different objective numerical apertures and different bandwidth of light sources.

Each step was measured 10 times and compared with the measurement results of Zygo NewView 8300, as shown in Table 3.3. The corresponding difference between commercial interference microscope and our snapshot multi-wavelength interference microscope is within 0.26% of each step height. Figure 3.14 shows the measurement error from 3 μm to 10 μm.

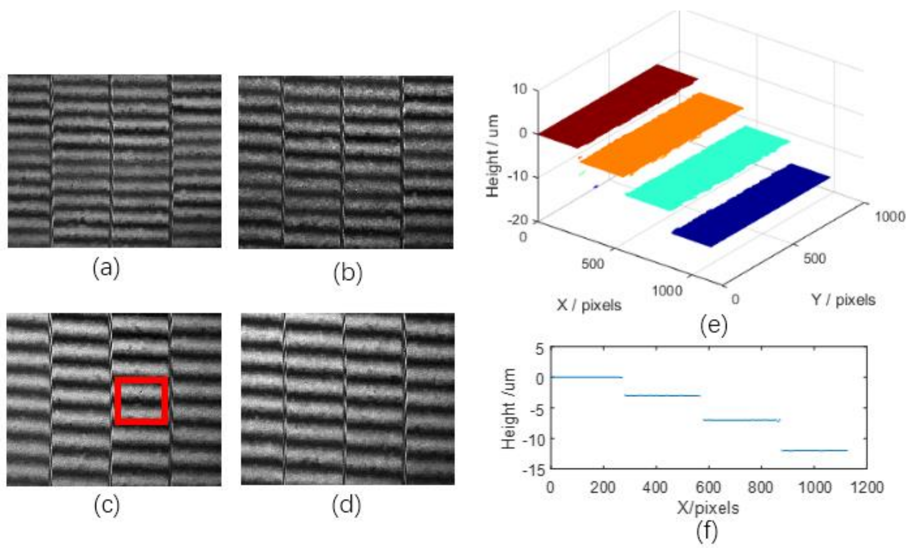

Figure 3.12 Measurement result for diamond turned copper with 3, 4 and 5 μm step heights. Gray scale interferograms are for (a) Blue laser, (b) Green laser, (c) Red LED, and (d) Red laser. (e) and (f) are 3D surface profile and line profile.

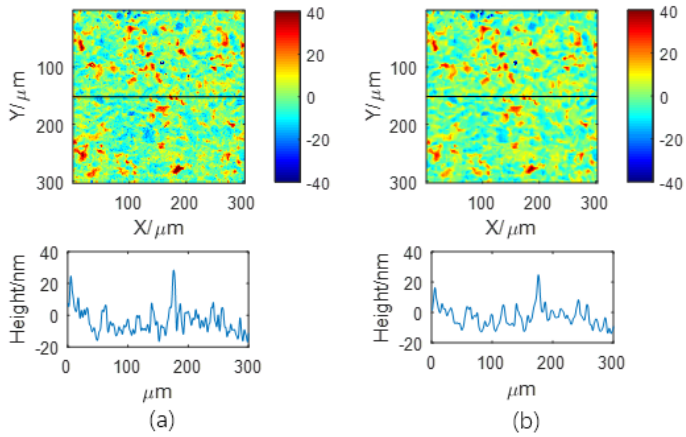

Figure 3.13 Surface topography of a diamond turned copper surface measured by (a) R channel in our system (b) Zygo NewView 8300.

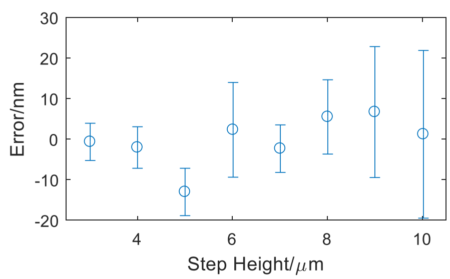

Figure 3.14 Measurement results for 3μm to 10μum step heights

Table 3-3 Measurement results of the diamond turned copper step height.

Zygo Newview 8300 Result (μm)	Snapshot multi-wavelegth interference microscope (μm)
3.0038	3.0031
4.0005	3.9984
5.0020	4.9890
6.0137	6.0160
7.0091	7.0067
8.0079	8.0134
8.9998	9.0065
10.0228	10.0240

3.6 Conclusion

We propose a snapshot multi-wavelength interference microscope for optical metrology. A custom color polarization camera is used to capture phase-shifted interferograms in three spectrums. The camera calibration method is presented to reduce the polarization error as well as color crosstalk. Single-shot measurement with large vertical range and high quality surface roughness measurement is achieved. This system is capable of measuring optical components at high speed with a large vertical range.

Chapter 4 Multi-wavelength Quantitative Polarization and Phase Microscope

4.1 Introduction

Measurement of the quantitative phase and optical anisotropy information has long been of interest to biomedical researchers. In recent years, a variety of quantitative phase microscopes have been developed to reconstruct the 3D profile of biomedical samples, including Fourier phase microscopy [65], digital holographic microscopy [66], Hilbert phase microscopy [67], diffraction phase microscopy [68], tomographic phase microscopy [69], and polarization phase microscopy [70]. Due to the characteristic of molecular architecture, most biological samples exhibit some degree of alignment. The extensive membranous structures can generate some birefringence and dichroism, which could influence the accuracy of phase measurement. Besides, these optical anisotropy properties of a specimen provide a sensitive method to analyze the alignment of molecular bands or fine structure form in cells and whole organisms [71]. Quantitative polarized light microscopy [72-75] has been developed to acquire the optical anisotropy information like birefringence, absorption, refraction, and scattering. Recently methods that combine the quantitative phase and birefringence measurement in a single system have been proposed in [76, 77]. However, in all these methods, the phase or birefringence information was measured in a single wavelength.

Multi-wavelength techniques contribute to the measurement in many aspects [78]. The quantitative phase shows the optical path length, which is a combination of refractive index and physical thickness. By combing the quantitative phase in multi-wavelength, the refractive index and thickness can be separated [79]. Cells with different protein concentrations can be distinguished by measuring the refractive index of cells [80, 81]. The measurement range can be increased by using a multi-wavelength method in solving the 2π ambiguities in phase unwrapping [82, 83]. Dual-wavelength and multi-wavelength techniques can also be used to solve the focusing problem [84] and the chromatic aberration [85]. The optical anisotropy like birefringence is always wavelength-dependent, which shows a different behavior in different wavelengths. Several systems have been developed to study the wavelength-dependent optical information, including spectroscopic phase microscopy [86], spectroscopic diffraction phase microscopy [87], quantitative dispersion microscopy [88], quantitative phase spectroscopy [89], dynamic spectroscopic phase microscopy [90] and white light interference microscopy.

In this section, we proposed a snapshot multi-wavelength quantitative polarization and phase microscope (MQPPM) to obtain the spectral dependent quantitative phase and polarization information, which uniquely integrates a polarized light microscope and a snapshot quantitative phase microscope in a single system [91]. A novel full-Stokes camera operating in the red, green, and blue spectrum is used in this system. With the advantages of simple structure and rapid measurement, this system is a useful tool in measuring quantitative polarization and phase information.

4.2 RGB Full-Stokes Camera

4.2.1 RGB Full-Stokes Camera Deign

A novel RGB full-Stokes camera [60] is used in this MQPPM to obtain irradiance, color, and polarization of the sample simultaneously. This RGB full-Stokes camera is constructed with a non-polarization beam splitter to separate light, two custom color polarization cameras constructed by 4D Technology, an achromatic QWP in front of one color polarization camera to capture circular polarization information, and a blank glass with the same thickness of the achromatic QWP in front the second color polarization camera to compensate the optical path. These two cameras are aligned with sub-pixel accuracy. Figure 4.1 shows the schematic of the RGB full-Stokes camera.

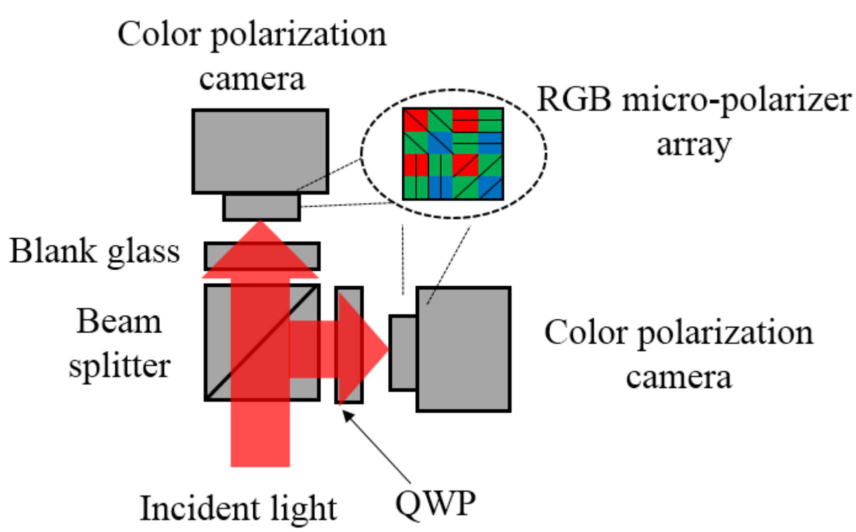

Figure 4.1 The schematic of the RGB full-Stokes camera

4.2.2 Camera Calibration

The color full-Stokes information is reconstructed with the irradiance of the two cameras. The missing irradiance is recovered at each pixel by a linear-spline interpolation. The camera calibration setup is shown in Figure 4.2. Three bandpass filters with center wavelengths of 460 nm, 540 nm, and 630 nm and a full width half maximum (FWHM) of 10 nm are used in the calibration. The light passing through the integrating sphere is considered as uniform unpolarized light, with a Stokes vector as:

$$S^0 = [\overrightarrow{S_R^0}\ \overrightarrow{S_G^0}\ \overrightarrow{S_B^0}]^T = [I_R\ 0\ 0\ 0\ I_G\ 0\ 0\ 0\ I_B\ 0\ 0\ 0]^T \tag{4.1}$$

where I_R, I_G and I_B are the total irradiance of the beam. The Stokes vector incident on the detectors is defined as

$$\begin{aligned} S &= [\overrightarrow{S_R}\ \overrightarrow{S_G}\ \overrightarrow{S_B}]^T \\ \overrightarrow{S_R} &= M_R^{QWP} M_R^P \overrightarrow{S_R^0} = [S_{R0}\ S_{R1}\ S_{R2}\ S_{R3}]^T \\ \overrightarrow{S_G} &= M_G^{QWP} M_G^P \overrightarrow{S_B^0} = [S_{G0}\ S_{G1}\ S_{G2}\ S_{G3}]^T \\ \overrightarrow{S_B} &= M_B^{QWP} M_B^P \overrightarrow{S_B^0} = [S_{B0}\ S_{B1}\ S_{B2}\ S_{B3}]^T \end{aligned} \tag{4.2}$$

where M^{QWP} and M^P are the Muller matrix of the achromatic QWP and the linear polarizer in the RGB spectrum measured by a commercial AxoScan Mueller matrix polarimeter. After interpolation, the irradiance I of each pixel contains the information of four polarization states (orientated at 0°, 45°, 90°, 135°), three wavelengths (460 nm, 540 nm, and 630 nm) from two cameras, which makes a total of 4*3*2 = 24 irradiance value. The relationship between recorded irradiance I, the analyzer matrix W and the input Stokes vector S on the detector can be written as:

$$I = WS \tag{4.3}$$

To calculate the analyzer matrix *W*, the linear polarizer is orientated at vertical, and the fast axis of QWP is rotated from 0° to 170° with a step of 10° for three wavelengths (460 nm, 540 nm, and 630 nm). In total, there are 54 measurements with 54 input light states. After get the analyzer matrix *W*, the incident Stokes vector can be solved as:

$$S = W^{+} \quad (4.4)$$

where W^{+} is the pseudo inverse of the analyzer matrix.

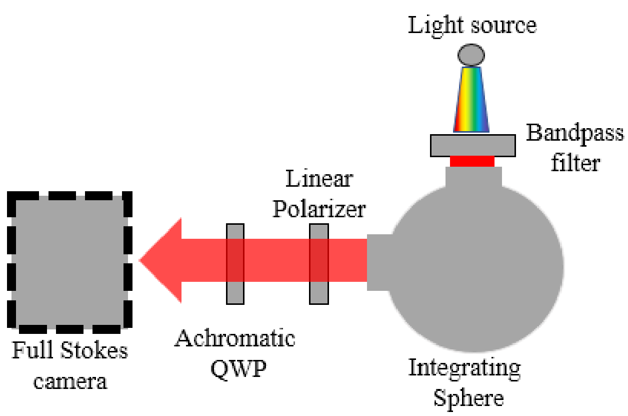

Figure 4.2 RGB full-Stokes camera calibration

4.3 Quantitative Polarization and Phase Microscope

4.3.1 System Design

This MQPPM is built on a Linnik interferometer microscope, as shown in Figure 4.3. Three LEDs in red, green, and blue from Thorlabs Inc. proved the multi-wavelength illumination. The central wavelengths of each LED are narrowed with bandpass filters at 460 nm, 540 nm, and 630 nm with a bandwidth of 10 nm. The light from LEDs passes through an achromatic collimating lens (L1) and a linear polarizer with a transmission axis at 0°. The light is then split into the test and reference arms by a non-polarization beam splitter (BS). Two achromatic QPWs are inserted in the test and reference arm. The QWP1 in the test arm is orientated at 45° related to the optical axis, transforms linear polarized light to circular polarized at first. This circular polarized light passes through the sample, is reflected by a flat mirror, and passes through QWP1 again. The polarization of the incident light rotates 90° after passing twice through the QPW1. And the QWP2 in reference arm is oriented at 0° related to the optical axis, which is used to matching the optical path length to test arm and does not change the polarization. This QWP2 can also be replaced with an optical window with the same optical thickness of the QWP1. A customized RGB full Stokes camera is used to capture the polarization images of the sample in three wavelengths simultaneously.

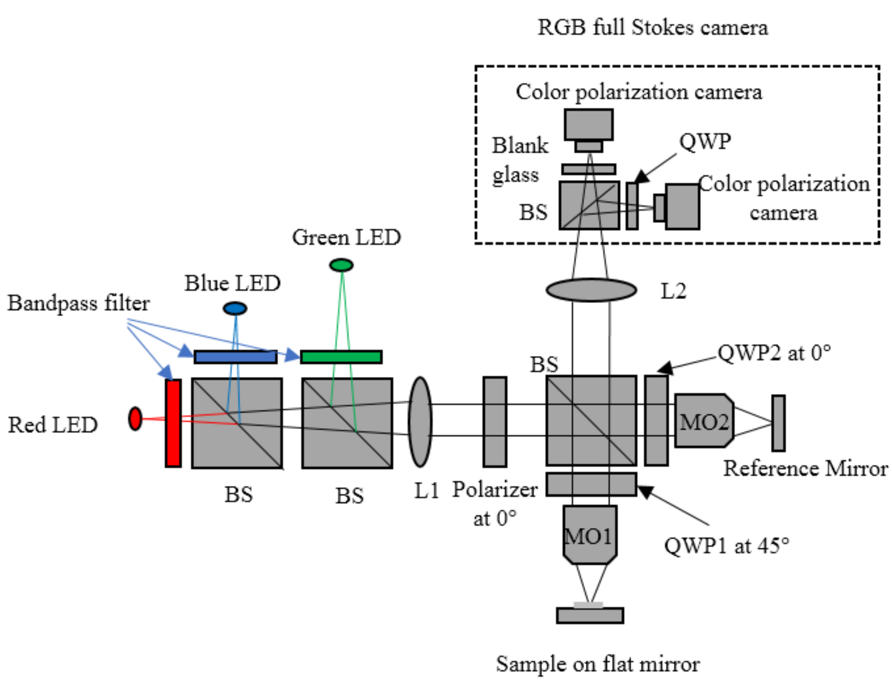

Figure 4.3 System layout of the snapshot multi-wavelength quantitative polarization and phase microscope (MQPPM). BS: non-polarizing beams splitter; L1 and L2: lens; P: polarizer; QWP1, QWP2 and QWP3: achromatic quarter waveplate; MO1 and MO2: microscope objective.

Based on the irradiance on the full-Stokes camera, the Stokes vector is calculated by Equation 4.4. The Stokes vector can be represented by the electric field vector E_x in x-direction and E_y in y-direction:

$$S = \begin{bmatrix} S_0 \\ S_1 \\ S_2 \\ S_3 \end{bmatrix} = \begin{bmatrix} E_x E_x^* + E_y E_y^* \\ E_x E_x^* - E_y E_y^* \\ E_x E_y^* + E_y E_x^* \\ i(E_x E_y^* - E_y E_x^*) \end{bmatrix} \tag{4.5}$$

where S_0 is the absolute irradiance, S_1 describes the amount of light polarized along the horizontal or the vertical axes, S_2 describes the amount of light polarized along 45° or 135°, and S_3 describes the amount of right or left circularly polarized light.

If a biomedical sample with birefringence information is measured in the system, the Jones vector in the test arm can be written as:

$$E_T = QWP(-45) * S(\phi, \delta, -\alpha) * M_R * S(\phi, \delta, \alpha) * QWP(45) * E_{in} \tag{4.6}$$

where $E_{in} = \begin{bmatrix} 1 \\ 0 \end{bmatrix}$ is the incident Jones vector of the beam after passing through the linear polarizer at 0°, $QWP(\alpha) = R(-\alpha)\begin{bmatrix} e^{i\pi/4} & 0 \\ 0 & e^{-i\pi/4} \end{bmatrix} R(\alpha)$ is the Jones matrix of the quarter wave plate with fast axis aligned at angle α, $R(\alpha) = \begin{bmatrix} \cos\alpha & \sin\alpha \\ -\sin\alpha & \cos\alpha \end{bmatrix}$ is a rotation matrix, and $M_R = \begin{bmatrix} 1 & 0 \\ 0 & -1 \end{bmatrix}$ is the Jones matrix of the dielectric mirror. The Jones matrix of a birefringence sample is written as:

$$S(\phi, \delta, \alpha) = e^{-i\phi} R(-\alpha) \begin{bmatrix} e^{i\delta/2} & 0 \\ 0 & e^{-i\delta/2} \end{bmatrix} R(\alpha) \tag{4.7}$$

where δ is the retardation, α is the angle of the fast axis and ϕ is the phase.

Based on Equation 4.6 and 4.7, the Jones vector of the beam returning from the test arm becomes

$$E_T = \begin{bmatrix} e^{-2i(\phi+\alpha)} \sin\delta \\ e^{-2i\phi} \cos\delta \end{bmatrix} \tag{4.8}$$

Since the fast axis of QWP in reference beam is oriented at 0°, the Jones vector of the beam in the reference arm can be calculated as:

$$E_R = QWP(0) * M_R * QWP(0) * E_{in} = \begin{bmatrix} 1 \\ 0 \end{bmatrix} \tag{4.9}$$

4.3.2 Birefringence Measurement

This system can be modified as a quantitative polarized light microscope by blocking the reference arm. For a birefringence sample, the retardance and fast axis can be measured simultaneously. Based on Equation 4.5 and 4.8, the Stokes vector of the birefringence sample is:

$$S_T = \begin{bmatrix} S_{T0} \\ S_{T1} \\ S_{T2} \\ S_{T3} \end{bmatrix} = \begin{bmatrix} 1 \\ -\cos 2\delta \\ \cos 2\alpha \sin 2\delta \\ \sin 2\alpha \sin 2\delta \end{bmatrix} \tag{4.10}$$

The fast axis angle and retardance can be calculated as:

$$\alpha = \frac{1}{2}\arctan(\frac{S_{T3}}{S_{T2}}) \tag{4.11}$$

$$\delta = \frac{1}{2}\arctan\frac{\sqrt{S_{T2}^2 + S_{T3}^2}}{-S_{T1}} \tag{4.12}$$

The calculated retardance has an ambiguity when the retardance is larger than $\pi/2$. This ambiguity could be unwrapped to get absolute retardance in a depth resolved imaging system [92]. Due to this ambiguity problem, the absolute retardance larger than $\pi/2$ can be calculated with:

$$\delta = \begin{cases} n\pi + \frac{1}{2}\arctan\frac{\sqrt{S_{T2}^2 + S_{T3}^2}}{-S_{T1}}, & n\pi \le \delta < (n+\frac{1}{2})\pi \\ (n+1)\pi - \frac{1}{2}\arctan\frac{\sqrt{S_{T2}^2 + S_{T3}^2}}{-S_{1T}}, & (n+\frac{1}{2})\pi \le \delta < (n+1)\pi \end{cases} \tag{4.13}$$

As shown in Equation 4.13, the range of retardance must be determined first to get absolute retardance. However, without prior knowledge of the birefringence of the sample, the range of retardance is undetermined. In addition, S_{T2} and S_{T3} are close to 0 when the retardance is close to $n\pi / 2$, which could lead to discontinuity for the fast axis calculation. This discontinuity problem can be solved by combining the results from the different wavelengths.

4.3.3 Phase Measurement

The phase of the sample can be measured with the interference phase microscope mode. The electric field of the optical field is the combination of the field of test and reference:

$$E = E_T + E_R = \begin{bmatrix} e^{-2i(\phi+\alpha)}\sin\delta + 1 \\ e^{-2i\phi}\cos\delta \end{bmatrix} \tag{4.14}$$

The Stokes vector of the recorded interferogram can be calculated with Equation 3.5 and 3.14, written as:

$$S = \begin{bmatrix} 1 \\ -\cos 2\delta \\ \cos 2\alpha \sin 2\delta \\ \sin 2\alpha \sin 2\delta \end{bmatrix} + \begin{bmatrix} 1 \\ 1 \\ 0 \\ 0 \end{bmatrix} + 2\begin{bmatrix} \cos(2\alpha + 2\phi)\sin\delta \\ \cos(2\alpha + 2\phi)\sin\delta \\ \cos\delta\cos 2\phi \\ -\cos\delta\sin 2\phi \end{bmatrix} = S_T + S_R + 2S_F \tag{4.15}$$

where $S_R = \begin{bmatrix} 1 \\ 1 \\ 0 \\ 0 \end{bmatrix}$ is the Stokes vector for the reference arm and $S_F = \begin{bmatrix} S_{F0} \\ S_{F1} \\ S_{F2} \\ S_{F3} \end{bmatrix} = \begin{bmatrix} \cos(2\alpha + 2\phi)\sin\delta \\ \cos(2\alpha + 2\phi)\sin\delta \\ \cos\delta\cos 2\phi \\ -\cos\delta\sin 2\phi \end{bmatrix}$ is the Stokes vector for the interference term between the sample and reference arms. To calculate the phase of the sample, S_F should be separated from the recorded interferogram. Since the frequency of the interferogram can be increased by tilting the reference mirror, S_F can be separated from $\boldsymbol{S}$ by Fourier transform method. Subtracting the Stokes vector of the sample and reference arms is another solution to get the S_F, which needs two separate measurements. The birefringence-induced phase error is corrected using the birefringence data. The phase can be calculated by

$$\phi = \frac{1}{2}\arctan\left(-\frac{S_{F3}}{S_{F2}}\right). \tag{4.16}$$

If the sample has no birefringence, i.e. when retardance $\delta = 0$, then Equation 4.15 can be simplified as

$$S = \begin{bmatrix} 2 \\ 0 \\ 2\cos 2\phi \\ -2\sin 2\phi \end{bmatrix} \tag{4.17}$$

The phase can be calculated from a single-shot measurement by

$$\phi = \frac{1}{2}\arctan\left(-\frac{S_3}{S_2}\right). \tag{4.18}$$

The phase in multi-wavelengths are the product of the refractive index n and physical thickness h, written as:

$$\begin{aligned} \phi_R &= h \cdot n(\lambda_R) \\ \phi_G &= h \cdot n(\lambda_G) \\ \phi_B &= h \cdot n(\lambda_B) \end{aligned} \tag{4.19}$$

And refractive index n can be represented with two-term form of Cauchy's equation

$$n(\lambda) = A + \frac{B}{\lambda^2} \tag{4.20}$$

where the coefficients A and B are determined specifically for this form of equation. The physical thickness and refractive index at λ_R, λ_G and λ_B can be determined by solving the Equations 4.19 and 4.20.

4.4 Experiment Results

4.4.1 System Validation

To verify the accuracy of the system, a waveplate was measured in our MQPPM. The fast axis of this waveplate rotated from 0° to 180° in steps of 10°. The retardance was measured by an AxoScan Mueller matrix polarimeter, as shown in Figure 4.4. The measured retardances at 460 nm (B), 540 nm (G), and 630 nm (R) are 131°, 104°, and 85°, respectively. Based on the knowledge that retardance for the R channel is in the range $(0, \pi/2)$, and retardance for the G and the B channels are in the range $(\pi/2, \pi)$, the retardance can be calculated by Equation 4.13 without ambiguity. The measured retardance for R, G, and B channel are 84.44°, 103.02°, and 129.63° with a standard deviation of 1.01°, 2.12°, and 3.05°, respectively. Figure 4.5(a) shows the retardance of the waveplate. The fast axis of this waveplate is calculated by Equation 4.11, as shown in Figure 4.5 (b). The standard deviation of the difference between the measured data and actual data are 2.75°, 3.79°, and 3.01° at the R, G, and B channels. The errors in retardance and fast axis orientation are caused by imperfect optical components and the limitation of the manually controlled rotational mounts.

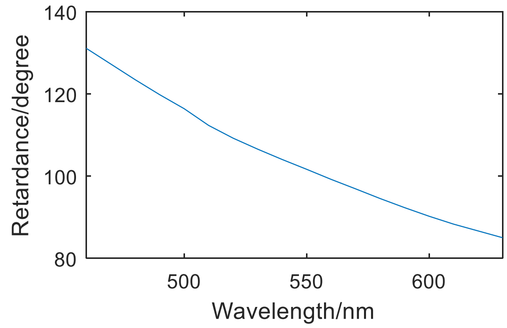

Figure 4.4 The retardance of waveplate measured by AxoScan Mueller matrix polarimeter

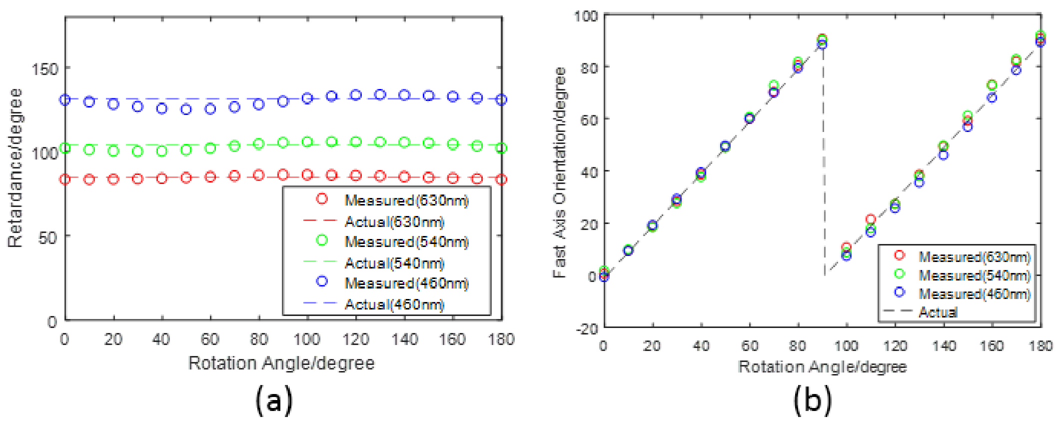

Figure 4.5 Measurement results of a waveplate (a) Retardance and (b) fast axis orientation angle of the waveplate at RGB spectrum as a function of rotation angle from 0° to 180° with 10° steps.

A step height standard (VLSI, SHS 4606 Å) was measured as a phase sample by our system. The step height standard is measured 10 times, calculated and averaged in accordance to the definition in ISO 5436-1 standard. Figure 4.6 shows the 3D surface and line profile of the step height standard in the R channel. The averaged measured step height is 460.37 nm, with a standard deviation of 1.87 nm, as shown in Table 4.1.

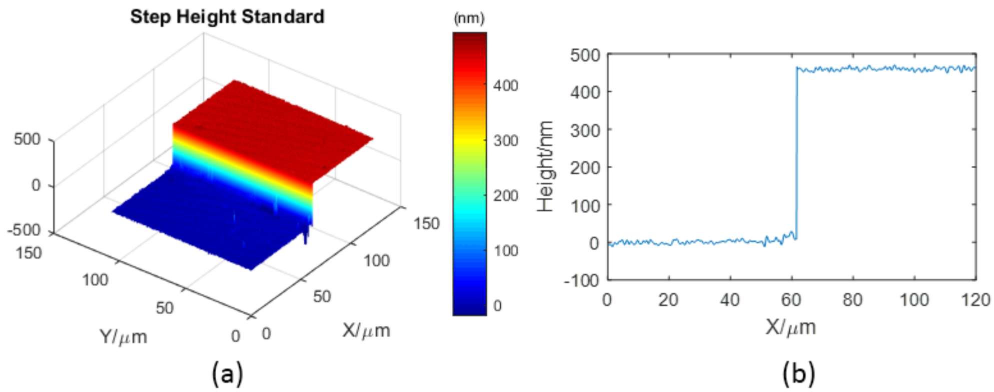

Figure 4.6 System calibration using a step height measurement. (a) 3D surface and (b) line profile of a step height standard.

Table 4-1 Measurement results of the VLSI step height standard from the R channel.

No.	Step Height (nm)	No.	Step Height (nm)
1	459.76	6	461.26
2	456.85	7	458.98
3	462.09	8	460.30
4	460.82	9	463.89
5	460.04	10	459.78
Mean value	460.37		
Std. Dev.	1.87		

4.4.2 Birefringent Sample

To demonstrate the capability of birefringence measurement, a drop of liquid crystal on a flat mirror was measured in our system, which contains both birefringence and phase information. To calculate the birefringence of this sample, the retardance for R, G, and B channels are firstly calculated by Equation 4.12, as shown in Figure 4.7(a)-(c). Since the retardance is larger than $\pi/2$, there is an ambiguity problem of these results. With a prior knowledge that the thickness of the liquid crystal drop increases from left to right starting from 0, the range of the retardance can be calculated by the slope. The retardance slope for each point (x, y) was calculated by $\delta(x+1, y)-\delta(x, y)$. We added a low pass filter to the retardance during the slope calculation to get rid of the influence of surface roughness. Any point (x, y) with a minus slope was considered in the range of $(n+\frac{1}{2})\pi \leq \delta < (n+1)\pi$, a minus sign was given to the retardance. After the range of the retardance is determined, the corrected wrapped retardance can be calculated by Equation 4.13, as shown in Figure 4.7(d)-(f). Then the wrapped retardance were unwrapped and shown in Figure 4.7(g)-(i).

The fast axis orientation of the R, G, and B channels were calculated by Equation 4.11 and shown in Figure 4.8(a)-(c). Two kinds of discontinuities are observed in the fast axis orientation map. The first discontinuity is due to the modulo nature of the arctangent function. The second discontinuity is caused by the fact that both the denominator and the numerator are zero in Equation 4.11 when the retardance is equal to $n\pi/2$, leading a large noise in the calculation. By combining the fast axis orientation in three wavelengths, this retardance-related and wavelength-dependent discontinuity can be removed. To combine the measurement in three different wavelengths, the fast axis of the R channel is used first since the standard deviation for the R channel is the smallest. If the retardance of one pixel in the R channel is less than 5° or greater than 85°, then the fast axis orientation of the R channel is considered unreliable, and the fast axis of this pixel is replaced with that of the G channel. If the retardance of the G channel is still less than 5° or greater than 85°, then the fast axis of this pixel is replaced with that of the B channel. In the case that the retardances of the RGB channels are less than 5° or greater than 85°, the fast axis orientation is defined to be zero. The fast axis orientation map after combining three wavelengths is shown in Figure 4.8(d).

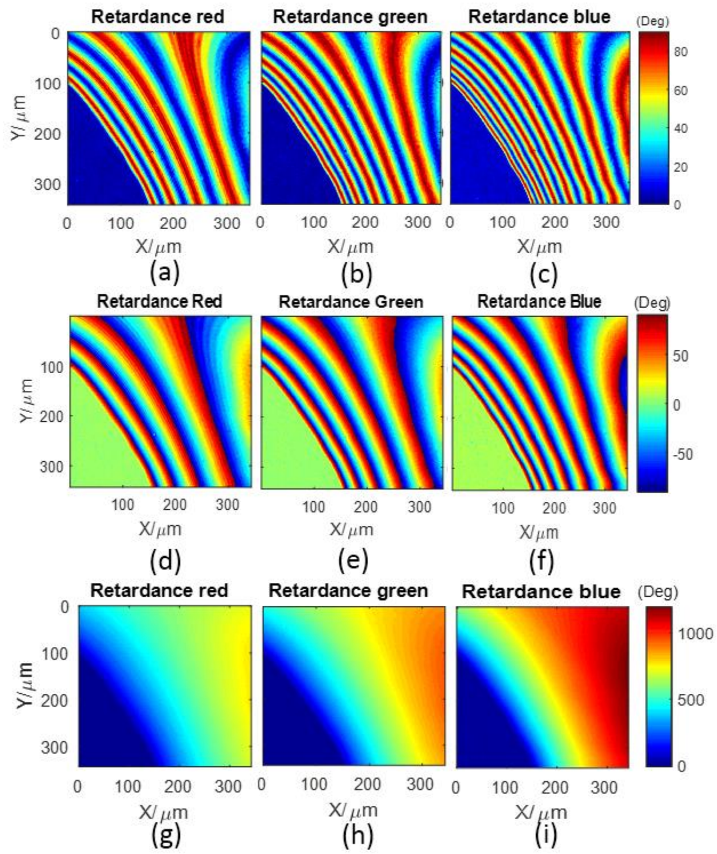

Figure 4.7 Measured retardance of liquid crystal in (a) red, (b) green and (c) blue. Wrapped retardance of liquid crystal in (d) red, (e) green and (f) blue. Unwrapped retardance of liquid crystal in (g) red, (h) green and (i) blue.

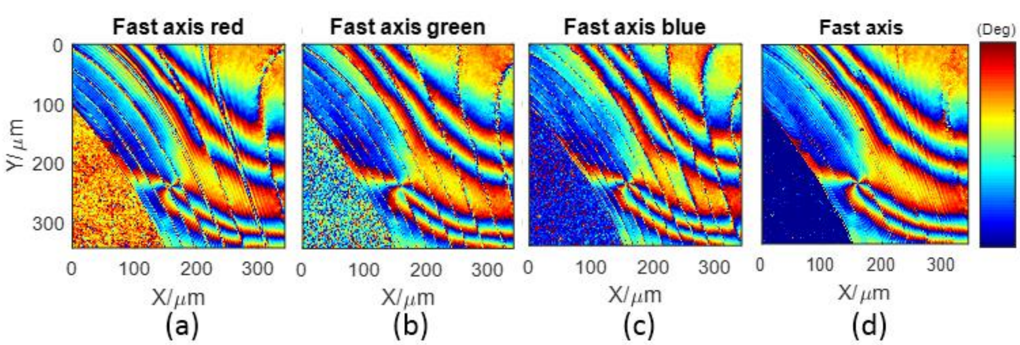

Figure 4.8 Fast axis orientation in (a) red, (b) green, (c) blue and (d) combined result of RGB.

The phase information was obtained with two separate measurements. The Stokes images were taken in both quantitative phase microscope mode and polarized light microscopes mode. The phase of this liquid crystal sample is calculated by Equation 4.16. The wrapped phase in R, G, and B channels are shown in Figure 4.9. Besides the discontinuity caused by the modulo nature of arctangent function, another discontinuity in phase map is observed, which is caused by the fact that both denominator and numerator are zero when the retardance equals to $(n+\frac{1}{2})\pi$. Due to the chromatic aberration and the limitation of the coherence length, the contrast of the interferograms in the blue channel drops faster than red and green, causing the increased noise in the blue channel as the thickness of liquid crystal increased.

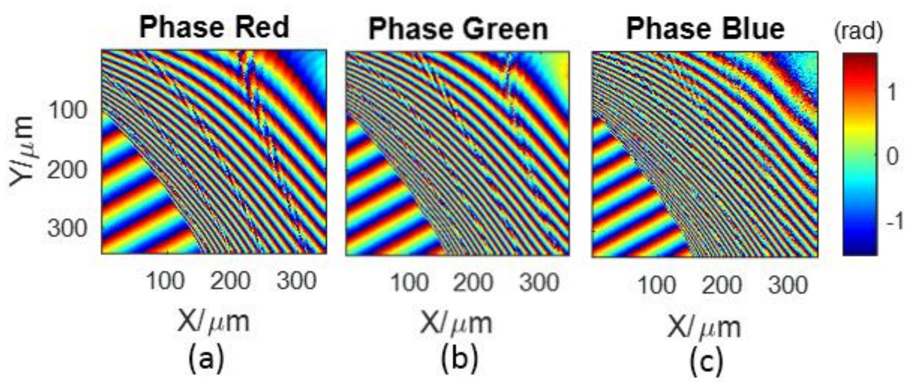

Figure 4.9 Wrapped phase of liquid crystal in (a) red, (b) green and (c) blue channels.

4.4.3 Biological Phase Samples

To demonstrate MQPPM's performance in real time imaging of biological samples, the red blood cells (RBCs) and human breast cancer cells were measured. These transparent biological cells were placed on a flat mirror in their growth media. The physical thickness and refractive index at R, G, and B wavelengths can be calculated by Equation 4.19 and 4.20.

Figure 4.10(a) shows the phase map of several RBCs in the red channel. Figures 4.10(b)-(d) show the three dimensional (3-D) images of one RBC in the R, G, and B channels, and Figure 4.10(e) shows the corresponding profiles of this cell. The OPD is larger for shorter wavelength due to its larger refractive index at a shorter wavelength.

Figure 4.11 shows the dynamic measurement of human breast cancer cells after the growth media was diluted by purified water. Purified water was added at 0 minute and 8 minutes. The cells osmotically swell after exposure to purified water in Figure 4.11(a)-(b). In Figure 4.11(c)-(d), swelling and flattening were observed after the cells were exposed to more purified water.

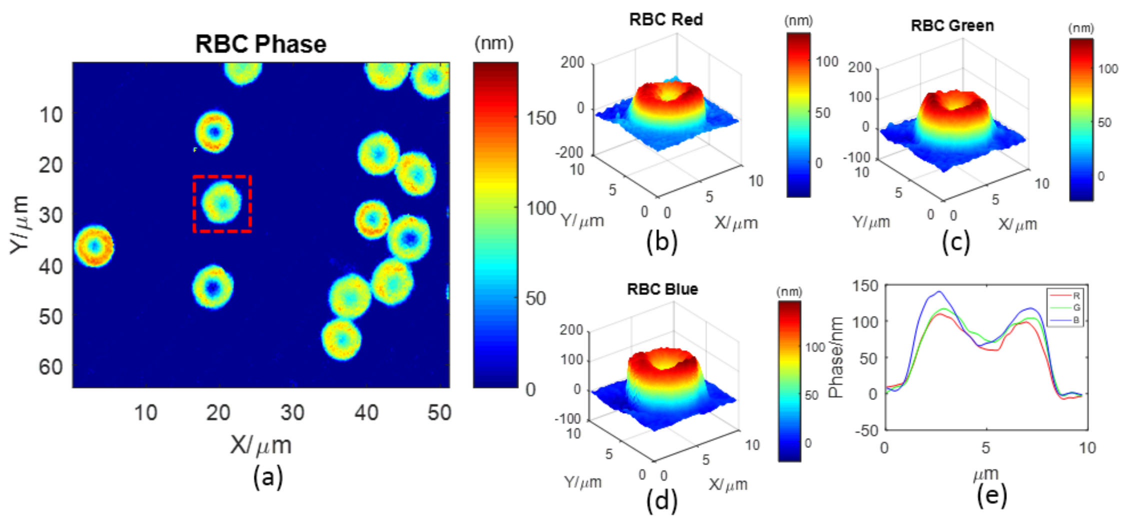

Figure 4.10 Measurement results of red blood cells (RBCs). (a) RBC phase in R channel, (b)-(d) 3-D images of one cell in the R, G and B channels, and (e) the phase profile of one cell in different wavelengths.

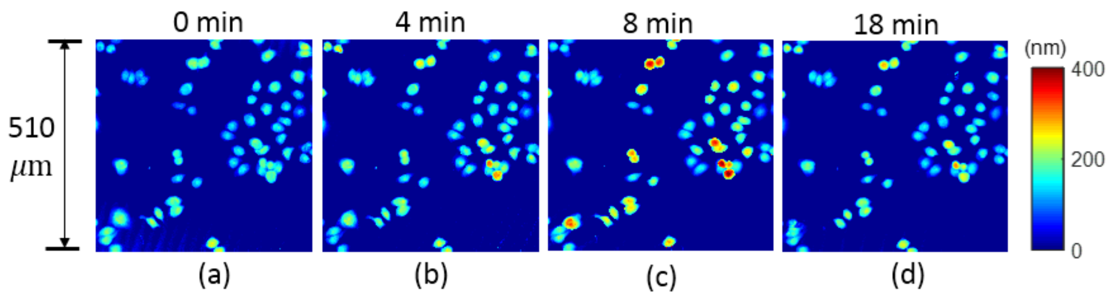

Figure 4.11 Time series of phase images of breast cancer cells after contact with purified water. (a)-(b) Cells osmotically swell after exposure to purified water. (c)-(d) Cells swell and flatten after more purified water were added.

4.4.4 Depolarization Sample

The polarization images of Arthrospira platensis were captured in the system in the polarized light microscope mode. The depolarization effect of Arthrospira platensis was recorded. The degree of polarization (DoP) is calculated by $DoP = \sqrt{S_1^2 + S_2^2 + S_3^2} / S_0$ in RGB spectrum. The color image of the sample is represented by S_0 images in Figure 4.12(a). The DoP images of R, G, and B are shown in Figure 4.12(b)-(d) with a scale bar of 20 μm. We can see the depolarization effect is wavelength related, and the shorter wavelength has a stronger depolarization.

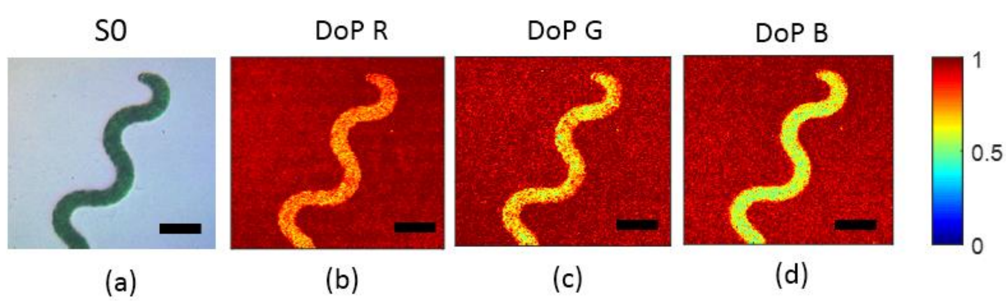

Figure 4.12 Measurement of an Arthrospira platensis sample (a) The S0 of the Stokes images (b)-(d) DoP of the Arthrospira platensis in R, G and B. The scale bar is 20 μm.

4.5 Conclusion

In this section, we demonstrate a multi-wavelength quantitative polarization and phase microscope, which combines the function of a polarized light microscope and a quantitative phase microscope in a single system. A custom full Stokes camera is used in the system to capture the full Stokes images in RGB channels simultaneously. Calibration method is demonstrated for this custom full Stoke camera to reduce the polarization crosstalk and color crosstalk. The system's capability for the quantitative phase and optical anisotropy information measurement is theoretically analyzed and experimental verified. This system shows a potential application in label-free imaging of biological specimens.

Chapter 5 Snapshot Phase-shifting Diffraction Phase Microscope

5.1 Introduction

Quantitative phase imaging (QPI) has been demonstrated as a valuable technology for characterizing phase objects [68,93,94]. Interferometric QPI approaches, which generate interferograms by extracting the phase differences between the object and reference beams, are the most widely used method for obtaining quantitative phase information. One of the major problems in retrieving highly sensitive quantitative phase images is phase noise due to the mechanical vibrations and air fluctuations. Among the various quantitative phase microscopes, diffraction phase microscopy (DPM) significantly alleviates the phase noise problem due to its common-path configuration.

Based on the angle between the object and reference beams, the basic configuration of QPI includes off-axis interferometry [95-97] and on-axis interferometry [98-101]. Off-axis interferometry generates a high frequency carrier due to the large angle between the object and the reference beams. The phase images can be obtained from a single interferogram by Fourier and Hilbert transforms [67,102, 103], which makes it suitable for dynamic measurement such as live cells in growth media. However, one limitation of this off-axis interferometry is that the carrier frequency must be high enough to separate the reconstructed phase information from the unwanted direct component and the twin images in the frequency domain. Thus the spatial resolution of the reconstructed phase image is limited. The interferograms in on-axis interferometry contain low frequency fringes due to the near zero angle between the object and reference beams. The phase information is extracted with a phase-shifting algorithm with several interferograms captured in time sequence. With a limitation of temporal resolution, the full space-bandwidth of the imaging system can be used.

In recent years, an intermediate solution between the on-axis and off-axis configuration, named slightly-off-axis interferometry, was proposed to optimize the tradeoff between the spatial and temporal resolution for QPI [104-106]. In slightly-off-axis interferometry, the object wave only needs to be separated from its conjugate term instead of its autocorrelation term in the frequency domain, which means the spatial frequency of the reference beam can be equally or slightly larger than the maximum spatial frequency of the recorded object wave. Thus the lateral resolution of the reconstructed phase image can be increased.

In this chapter, we present a snapshot phase-shifting diffraction phase microscopy (SPDPM) for high spatial frequency phase images reconstruction simultaneously [107]. A polarization grating is used to generate opposite circular polarization beams for the object and reference paths. Phase-shifted interferograms can be obtained simultaneously by spatial phase-shifting using a polarization camera [108]. This compact common-path configuration of DPM reduces phase noise caused by mechanical vibrations and air turbulence. The acquisition speed is only limited by the speed of the polarization camera. The spatial resolution of the reconstructed phase images can be increased by using a phase-shifting algorithm.

5.2 Principle of SPDPM

This SPDPM combines the single-shot spatial phase-shifting feature of the polarization camera with an off-axis DPM. Opposite circular polarization beams are generated for the sample and reference paths in the DPM. Four phase-shifted interferograms can be captured simultaneously with the polarization camera. The diffraction phase module is shown in Figure 5.1. A polarization grating is located at the image plane of the microscope, where is also the input plane of the 4f system. This polarization grating separates the incident beam into opposite circular polarized beams in positive and negative first orders. A spatial filter is placed at the Fourier plane of Lens L1 to extract the +1st and -1st diffraction orders as the reference and sample fields. The positive first order is low-pass filtered by a pinhole in the spatial filter as reference beam while the negative first order passes the spatial filter with its entire frequency content.

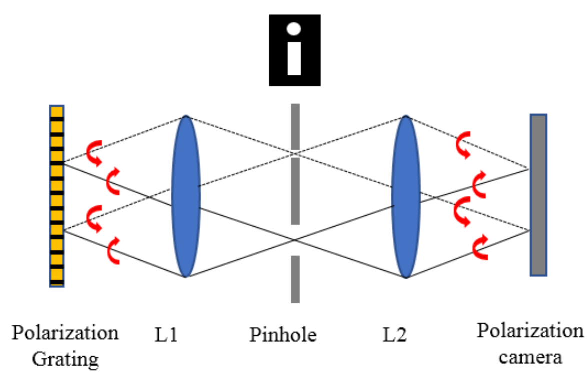

Figure 5.1 A schematic of diffraction phase module in SPDPM.

The field after passing through the polarization grating can be written as:

$$E_{PG} = E_{-1}(x,y)e^{-i\frac{2\pi}{\Lambda}x} + E_{+1}(x,y)e^{i\frac{2\pi}{\Lambda}x} \tag{5.1}$$

where $E_{-1}(x,y) = A_{-1}(x,y)e^{i\varphi_{-1}(x,y)}\begin{bmatrix}1\\ i\end{bmatrix}$ is the -1st order field and $E_{+1}(x,y) = A_{+1}(x,y)e^{i\varphi_{+1}(x,y)}\begin{bmatrix}1\\ -i\end{bmatrix}$ is the +1st order field [109], Λ is the grating period.

At the spatial filter plane before the pinhole, the field is taken Fourier transform by the first lens L1 in 4f system:

$$\tilde{E}_{SF^-}(\xi,\eta) = \tilde{E}_{-1}(\xi + \frac{2\pi}{\Lambda},\eta) + \tilde{E}_{+1}(\xi - \frac{2\pi}{\Lambda},\eta) \tag{5.2}$$

where $\xi = \frac{2\pi}{\lambda f_1}x_1$ and $\eta = \frac{2\pi}{\lambda f_1}y_1$, ($x_1$,$y_1$) are the coordinates at the Fourier plane.

After passing through the spatial filter with a small pinhole to filter down the +1st, the field can be written as:

$$\begin{aligned}\tilde{E}_{SF^+}(\xi,\eta) &= \tilde{E}_{-1}(\xi + \frac{2\pi}{\Lambda},\eta) + \tilde{E}_{+1}(\xi - \frac{2\pi}{\Lambda},\eta) * \delta(\xi - \frac{2\pi}{\Lambda},\eta) \\ &= \tilde{E}_{-1}(\xi + \frac{2\pi}{\Lambda},\eta) + \tilde{E}_{+1}(0,0)\delta(\xi - \frac{2\pi}{\Lambda},\eta)\end{aligned} \tag{5.3}$$

Then this field passes through the second lens L2 in the 4f system, the resulting field at the camera plane can be written as:

$$\begin{aligned}E(x,y) &= E_{-1}(x,y)e^{-i\frac{2\pi}{\Lambda}x} + E_{+1}(0,0)e^{i\frac{2\pi}{\Lambda}x} \\ &= A_{-1}(x,y)e^{i\varphi_{-1}(x,y)}e^{-i\frac{2\pi}{\Lambda}x}\begin{bmatrix}1\\ i\end{bmatrix} + A_{+1}e^{i\varphi_{+1}}e^{i\frac{2\pi}{\Lambda}x}\begin{bmatrix}1\\ -i\end{bmatrix}\end{aligned} \tag{5.4}$$

These left and right circular polarized beams generate interferograms on the detector plane of the polarization camera as follows:

$$\begin{aligned}
I_{0^\circ}(x,y) &= I_{-1}(x,y) + I_{+1} + 2\sqrt{I_{-1}(x,y)I_{+1}}\cos(\Delta\phi + \frac{4\pi}{\Lambda}x) \\
I_{45^\circ}(x,y) &= I_{-1}(x,y) + I_{+1} + 2\sqrt{I_{-1}(x,y)I_{+1}}\cos(\Delta\phi + \frac{4\pi}{\Lambda}x + 90^\circ) \\
I_{90^\circ}(x,y) &= I_{-1}(x,y) + I_{+1} + 2\sqrt{I_{-1}(x,y)I_{+1}}\cos(\Delta\phi + \frac{4\pi}{\Lambda}x + 180^\circ) \\
I_{135^\circ}(x,y) &= I_{-1}(x,y) + I_{+1} + 2\sqrt{I_{-1}(x,y)I_{+1}}\cos(\Delta\phi + \frac{4\pi}{\Lambda}x + 270^\circ)
\end{aligned} \tag{5.5}$$

where $\Delta\phi(x,y) = \phi_{-1}(x,y) - \phi_{+1}$, I_{0°, I_{45°, I_{90°, and I_{135° are the irradiance of the pixels with the linear polarizers with orientation angles of 0°, 45°, 90°, and 135°. The phase of the sample can be calculated with a four-step phase-shifting algorithm:

$$\Delta\phi = \tan^{-1}(\frac{I_{135^\circ} - I_{45^\circ}}{I_{0^\circ} - I_{90^\circ}}) \tag{5.6}$$

5.3 SPDPM with Polarization Grating

5.3.1 System Layout

The experimental setup of the proposed SPDPM is shown in Figure 5.2. Both transmitted and reflected DPM illumination modes have been implemented in this system. Two HeNe lasers (λ=632.8 nm) are used as light sources in the system. The polarizers after light sources are orientated at 0°. The microscope objective and the tube lens produce an image of the sample at the image plane of the microscope. The diffraction phase module contains a 4f optical system that consists two lenses with the focal lengths of 75 mm and 250 mm. The first lens L1 contains two 2-inch achromatic doublets (Thorlabs AC508-150-A-ML) while the second lens L2 is a 1-inch achromatic doublet (Thorlabs AC254-250-A-ML). The input plane of the 4f-system coincides with the image plane of the microscope and a polarization grating with 159 grooves per millimeter

(Edmund Optics #12-677). A polarization camera (BFS-U3-51S5P-C) is used to capture four phase-shifted interferograms.

Due to the high groove density of this grating, the frequency of the interferograms is too high to resolve. There are several methods to reduce the fringe density. The first and most straightforward method is to replace this commercial polarization grating with a custom polarization grating with lower groove density. The second solution is increasing the magnification of the 4f system, which could reduce the frequency of the fringe but also reduce the field of view (FOV) of this SPMPM. The last solution is adding folding mirrors before the spatial filter plane to decrease the distance between the positive and negative first order, as shown in Figures 5.2 and 5.3. The fringe density of the interferograms can be adjusted by changing the distances of the folding mirrors. During the experiment the folding mirror method is used. Since object and reference beams are not exactly common path after these folding mirrors, phase error may be introduced due to environmental noise like vibration. However, this phase error can be minimized with the snapshot feature of this system.

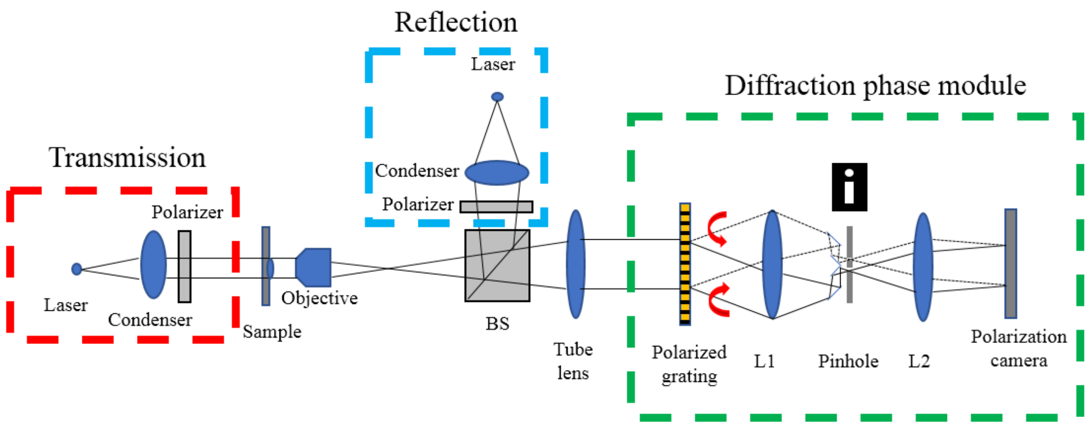

Figure 5.2 Experiment setup for SPDPM with polarization grating. BS: beam splitter.

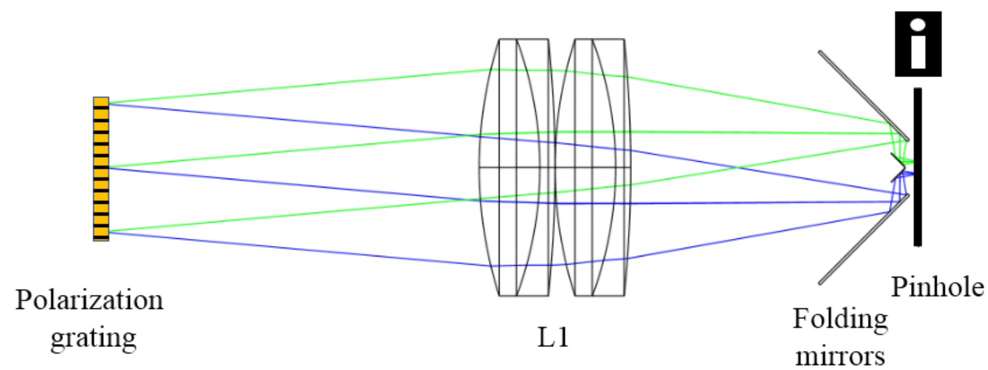

Figure 5.3 Folding mirrors in diffraction phase module

5.3.2 Experiment Results

To demonstrate the feasibility of the proposed system, both transmission and reflection samples were measured. A step height standard (VLSI, SHS 4606 Å) was used as a reflection sample. The microscope objective has a magnification of 10x and a numerical aperture of 0.25. The magnification of the 4f system is 3.3. The total magnification of the system is 33. The polarization camera has 2448 x 2048 pixels with a pixel size of 3.45 μm. The interferograms with a phase-shifted value of 0°, 90°, 180°, and 270° are shown in Figure 5.4. The reconstructed 3D surface of this step height standard is shown in Figure 5.5(a). Figure 5.5(b) shows the line profile comparison measured by our SPDPM, which is averaged with 10 pixels. Figure 5.6 shows the 3D profile and line profile measured by Zygo 8300 white light interference microscope. The measured step height is 464.5 nm by SPDPM and 462 nm by Zygo white light interference microscope. The height deviation is about 2.5 nm. The surface root mean square (RMS) is 18.13 nm by SPDPM and 0.77 nm by Zygo. This large RMS deviation is mainly caused by the coherence noise of the laser light source. To reduce this error, a low coherence light source can be used. This experiment demonstrates the accuracy of the proposed SPDPM.

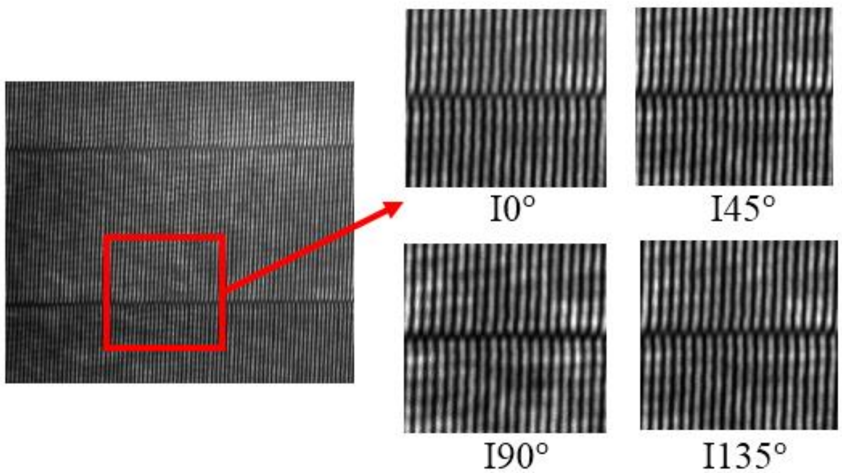

Figure 5.4 Phase-shifted interferograms of the step height target with phase shifts: 0°, 90°, 180° and 270°.

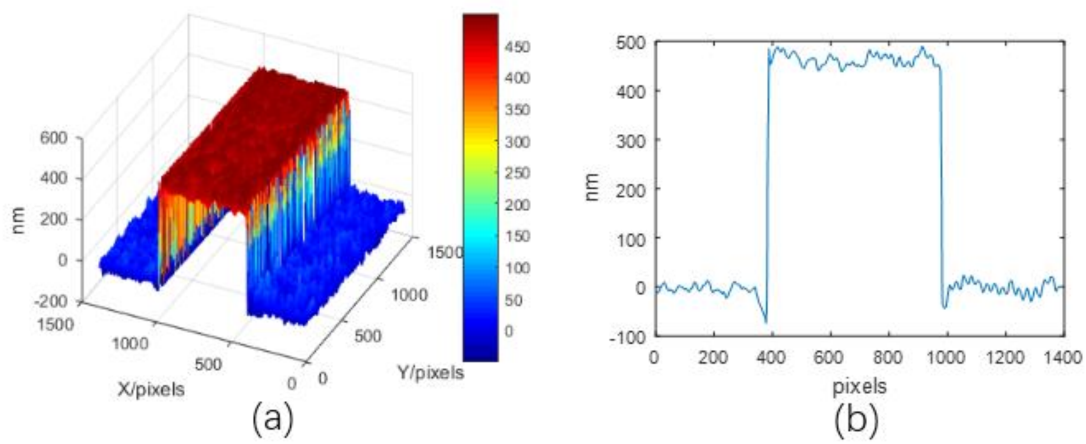

Figure 5.5 Reconstructed step height measured by SPDPM. (a) 3D surface and (b) line profile of a step height standard.

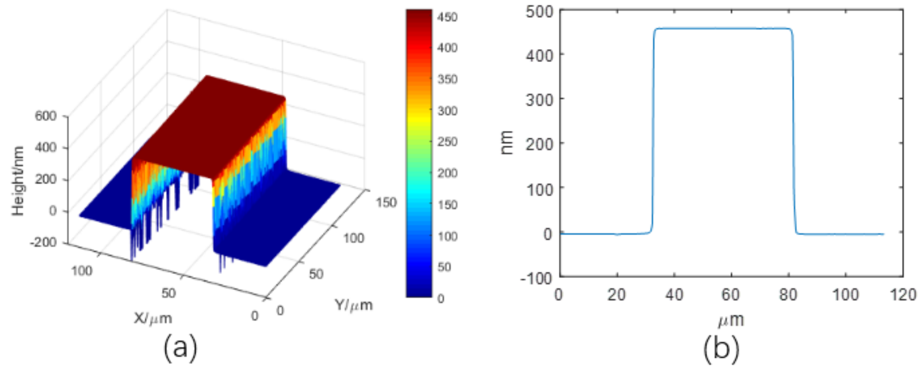

Figure 5.6 Reconstructed step height measured by Zygo NewView 9300 white light interference microscope.

(a) 3D surface and (b) line profile.

A 3D printed lens was used as a transmission sample to demonstrate the phase measurement of transmission mode. Figure 6.7(a) shows the phase-shifted interferograms of the 3D printed lens. Figure 6.7(b) and 6.7(c) are the reconstructed 3D surface and line profile across the center of this lens.

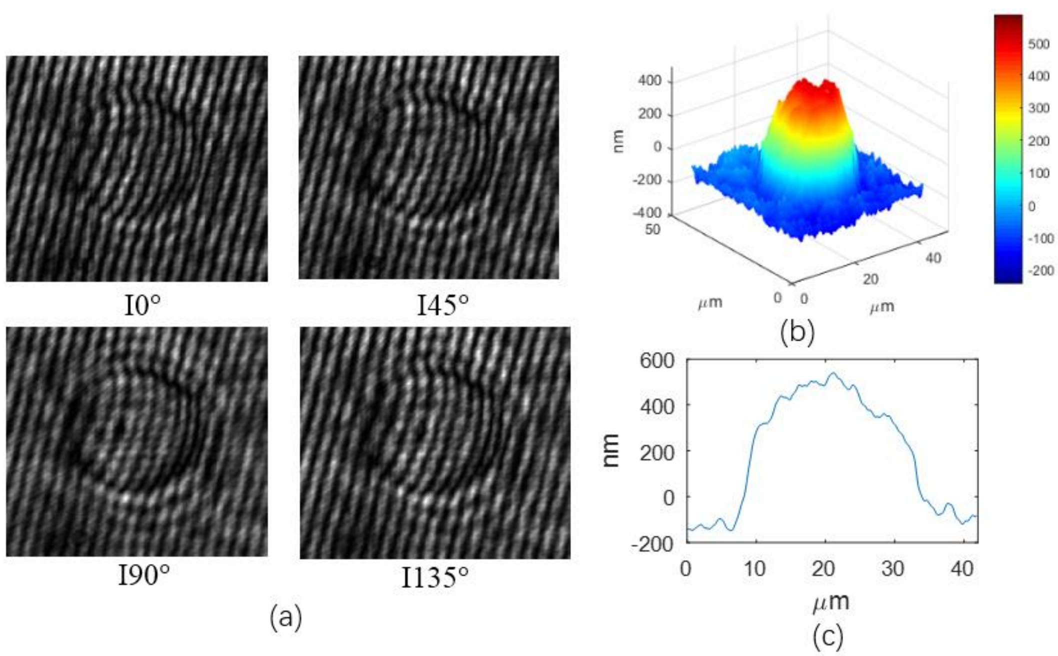

Figure 5.7 3D printed lens. (a) interferograms, (b) 3D reconstructed surface, and (c) line profile.

5.4 SPDPM with Polarizers and QWP

5.4.1 System Layout

The polarization grating can be replaced by a regular grating with orthogonal polarizers and a quarter wave plate (QWP). The diffraction phase module is shown in Figure 5.8. A 4f optical system consists of two lenses with focal lengths of 75 mm and 250 mm. A transition grating with 70 grooves per millimeter (Edmund Optics #46-068) is used in this configuration. The incident beam with a linear polarization state is diffracted into multiple orders at the grating. The 0th order of the beams with 41% diffraction efficiency serves as the object beam to reduce the off-axis aberration. The first order of the beams with 32% diffraction efficiency is filtered with a 30 μm pinhole to generate a spherical wavefront as the reference beam. Two polarizers orientated at 0° and 90° are attached after the pinhole plane. The relative irradiance between the objective and reference beams can be adjusted by changing the polarization state of the incident beam. A QWP orientated at 45° is placed between the polarizers and L2. The object and reference beams with orthogonal linear polarization states are transformed into opposite circular polarizer states after passing through the QWP. Then four phase-shifted interferograms can be captured simultaneously with the polarization camera.

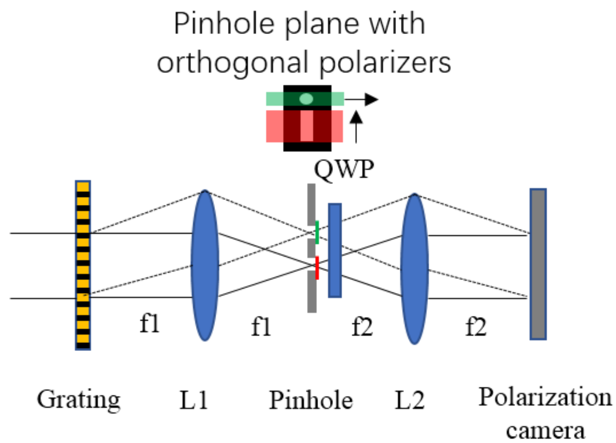

Figure 5.8 Diffraction phase module with orthogonal polarizer and QWP.

5.4.2 Experiment Results

To demonstrate the feasibility of the system with polarizer and grating, one drop of UV cure glue was used as a transmissive sample. One of the phase-shifted interferograms is shown in Figure 5.9 (a). Figure 5.9 (b) shows the reconstructed 3D phase image.

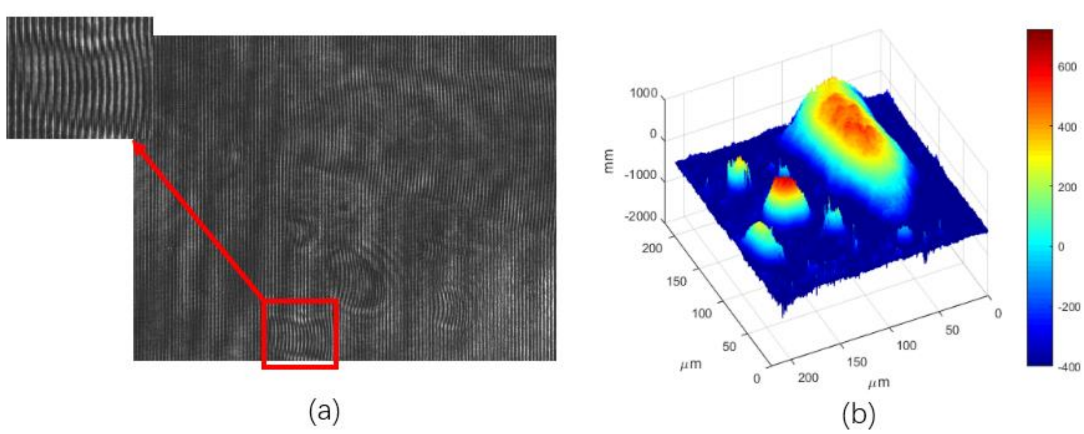

Figure 5.9 Measurement result of UV cure glue. (a) Interferogram and (b) reconstructed phase image

5.5 Conclusion

In this chapter, a single-shot high spatial resolution phase image reconstruction technology by combing the spatial phase-shifting feature of the polarization camera and an off-axis diffraction phase microscopy has been proposed. By generating opposite circular polarization beams with polarization grating for the object and reference arms, phase-shifted interferograms can be capture by the polarization camera simultaneously. Transmission and reflection illumination modes have been developed and used for quantitative phase image reconstruction. We believe the presented approach is a useful tool for fast high spatial resolution quantitative phase measurement.

Chapter 6 Snapshot Adaptive Freeform Null Testing

6.1 Introduction

With the development of optical design and fabrication, freeform optics plays an important role in modern optical systems. Compared to spherical surfaces, a freeform optical system has the benefits of better performance, fewer elements, and light weight. While the design method of the freeform surface has been improved significantly recently, the freeform metrology is one of the key barriers in effectively and expediently fabricating complex freeform elements.

Both interferometric method and non-interferometric method have been investigated for freeform surface metrology. Null interferometry with a computer-generated hologram (CGH) has high accuracy for freeform surface testing [108, 109], but each surface requires a custom CGH. Non-null interferometry systems, such as tilt-wave-interferometer [110] and stitching interferometer [111], have been commercialized for freeform surface metrology, but they are expensive and bulky. In addition, calibration must be taken to do stitching and remove errors like retrace error [112]. Non-interferometric methods, such as deflectometry [113] and probe-scanning [114], have the advantages of large measurement range, but they also have some limitations. Deflectometry is a slope measuring method, which needs special calibration based on the system configuration. Probe-scanning, like coordinate measuring machine (CMM) [115] and chromatic confocal probe [116], takes measurement point-by-point, needs accurate surface fitting [117], and requires long measurement time.

To overcome the limitations of null interferometry, the deformable mirror (DM) has been used as an adaptive null component. In 2004, Pruss and Tiziani [117] proposed a concept with a membrane DM as a compensator to test symmetrical aspheric. In 2014, Fuerschbach *et al.* [118] reported an interferometric null testing system for a freeform φ polynomial mirror. Adjustable sub-systems with Offner lenses, tilted testing mirror, and DM are used to null the spherical aberration, astigmatism, and coma, respectively. A Shark-Hartmann sensor was used to measure the DM's shape. In 2016, Huang *et al.* [119] reported an adaptive interferometric null testing method for unknown freeform optics. DM and null optics were used for null testing. The DM's shape is optimized by the stochastic parallel gradient descent (SPGD) algorithm and measured by a deflectometry system. In 2018, Zhang *et al.* [120] proposed an adaptive interferometer which combines the DM surface monitoring and freeform surface measurement in one interferometer. One limitation of all the proposed methods is that the DM surface shape may drift slightly during the phase-shift measurement, introducing measurement errors.

In this chapter, we propose a snapshot adaptive null interferometric system with DM as a null corrector for measuring unknown freeform surfaces. The DM surface shape is optimized by the SPGD algorithm. A micro-polarizer array-based simultaneous phase-shifting interferometer is used in the system. The total measurement time is determined by the steps number of the iteration process and time spend in each step. Comparing with temporal phase-shifting, the measurement speed is greatly increased by using a snapshot interferometric system. And our system is insensitive to the environment noise or DM drift noise.

6.2 System Design

The system layout is shown in Figure 6.1. A HeNe laser with the wavelength of 632.8 nm is collimated by the collimation lens L1, a polarizer (P) is placed between L1 and polarization beam splitter (PBS) for adjusting the fringe contrast. The polarized light is divided into two beams with orthogonal polarization. Both beams pass twice through a quarter wave plate (QWP1 or QWP2) with the fast axis at 45° relative to the horizontal axis before returning to the PBS. Then two orthogonal linear polarized beams are transformed to opposite circular polarized light by QWP3. An Alpao DM with 97 actuators and 13.5 mm aperture diameter is placed in the test arm as the adaptive null corrector. The DM is tilted 45° about the optical axis. The test ray is reflected at DM, then passes through a microscope objective (MO), which is used as a transmission sphere, and finally hit on the surface under test. L3 is an imaging lens, imaging the test surface onto the detector.

To achieve snapshot measurement, a pixelated polarization camera PolarCam from 4D Technology is used to capture 4 phase-shifted interferograms simultaneously. A compact deflectometry system [121], which contains a small LCD monitor and a camera, is used to measure the DM shape precisely after DM is optimized. Comparing with other wavefront measurement methods, such as the Shack-Hartmann sensor, the deflectometry system has higher spatial resolution and is able to measure DM surface accurately.

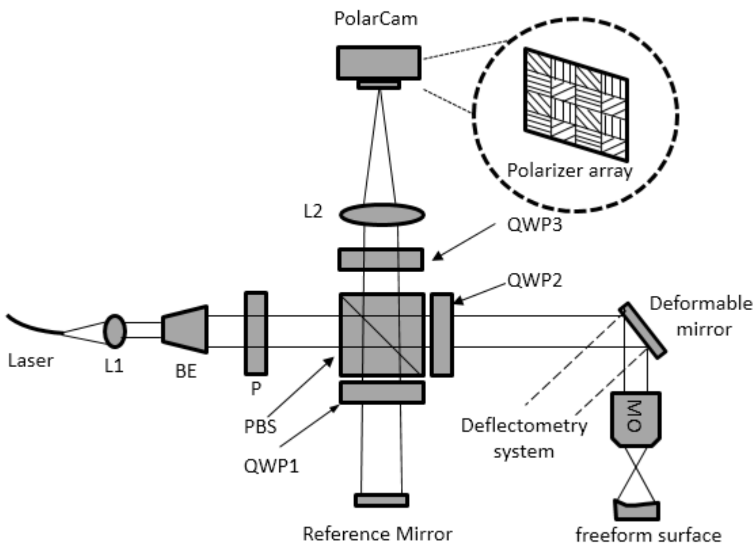

Figure 6.1 System layout: L1 - L2: lenses; P: polarizer; PBS: polarized beam splitter; QWP1 - QWP3: quarter wave plate; MO: microscope objective; PolarCam: pixelated polarizer camera; and DM: deformable mirror. Deflectometry system contains a LCD monitor and camera.

6.3 Principle of Snapshot Adaptive Freeform Null Testing

6.3.1 DM Calibration

The freeform surface shape is a function of the measured wavefront from the interferometer and DM shape, written as:

$$W_t = f(W_I, S_{DM}) \tag{6.1}$$

where W_t is the wavefront of the surface under test, W_I is the wavefront measured by the interferometer, S_{DM} is the DM shape measured by deflectometry system. W_I is close to zero if we adjust the DM to achieve null fringe condition. But due to the limited number of actuators, there will always be some residue errors, which can be measured by the interferometer.

Different from wavefront measurement, the S_{DM} could not be directly added to the interferometric measurement results. Besides, only part of the DM surface is used in correcting the freeform wavefront, depending on the actual size of the surface under test. The mapping relationship between W_t and S_{DM} must be calculated. During the calibration process, a standard reference sphere instead of a freeform surface was placed in the test arm. So the W_t was zero during the calibration. For first order approximation, W_t is a linear combination of W_I and S_{DM}, then we have

$$\Delta W_I + c \cdot \Delta S_{DM} = 0 \tag{6.2}$$

where c is a constant value related to the angle between the DM surface and the optical axis, ΔW_I is the wavefront change measured by the interferometer, ΔS_{DM} is the DM shape change measured by deflectometry. In the calibration process, a set of DM shapes were generated and captured by both interferometer and deflectometry. A mapping relationship between W_I and S_{DM} can be established based on these two sets of measurement data.

6.3.2 DM Control Algorithm

An adaptive null algorithm containing three steps has been developed to drive the DM. The DM is controlled by stochastic parallel gradient descent (SPGD) algorithm [122] in the first and second steps. SPGD algorithm is a wavefront aberration correction algorithm that can recover the wavefront without a wavefront sensor. It is suitable to tune DM when the wavefront cannot be measured by the interferometer. A small random voltage perturbation is generated and applied to each actuator, system performance metric (J) is evaluated after the voltages are applied. The control signals update of SPGD algorithm is based on Equation 6.3 and 6.4:

$$u^{k+1} = u^k - \gamma \delta J^k \delta u^k \tag{6.3}$$

$$\delta J^k = J(u^k + \delta u^k / 2) - J(u^k - \delta u^k / 2) \tag{6.4}$$

where u is the control signal vector, k is the iteration number, $u^k = \{u_1^k, u_2^k, \cdots, u_N^k\}$ is the control signal vector, N is the control channel number which is 97 in our experiment, γ is the gain coefficient, $\delta u^k = \{\delta u_1^k, \delta u_2^k, \cdots, \delta u_N^k\}$ is the small random perturbations with Bernoulli probability distribution and identical amplitudes.

In the first step, the no-fringe areas are searched by the grayscale response of the camera. The system performance metric J_1 is defined as:

$$J_1 = \sum_{mask} \{I_1 + I_2 + I_3 + I_4\} / N \tag{6.5}$$

where I_1, I_2, I_3, and I_4 are the interferograms irradiance with 0°, 90°, 180°, and 270° phase-shift values, the mask includes all the pixels in the no-fringe areas, and N is the total number of pixels within the mask. The sum of four phase-shifted interferograms is a constant value without considering noise. A threshold value is set as the average of four phase-shifted interferograms. For the no-fringe area, the sum irradiance of four different phase-shifted interferograms is below the threshold value. The actuators are tuned to restore the fringes.

After the fringe restored, the DM is fine tuned to reduce the dense fringe. The system performance metric J_2 for the tuning process of the second step is defined as:

$$J_2 = \sum_{mask} g(x, y) \tag{6.6}$$

$$g(x, y) = \begin{cases} 1, & if \;\; W(x, y) > 2\pi \\ 0, & if \;\; W(x, y) \le 2\pi \end{cases} \tag{6.7}$$

$$W(x, y) = abs[W_{wrap}(x, y) - W_{wrap}(x-1, y)] / 2 + abs[W_{wrap}(x, y) - W_{wrap}(x, y-1)] / 2 \tag{6.8}$$

where $W_{wrap} = \arctan\frac{I_4 - I_2}{I_1 - I_3}$ is the wrapped phase calculated by the four-step phase-shift algorithm. W_{wrap} contains a 2π phase shift between adjacent pixels if the phase value is larger than π or smaller than -π. By calculating the number of points with a 2π phase shift, we can evaluate the fringe density of the interferogram. In this step, the unwrapped phase is hard to calculate due to the dense fringe, but the wrapped phase can be easily calculated using the four-step phase-shift algorithm. Compared to the performance metric calculated by the grayscale value of the interferograms, the performance metric defined by phase information provides us a more robust optimization progress since it's less influenced by noise such as laser instability and background illumination.

After the iteration process of SPGD, the fringe density of interferograms is reduced, and the phase information is now measurable by the interferometer. But there may still be large retrace errors due to the dense fringe. In the third step, the fringe is further relaxed to almost null condition. To reduce the optimization time, near null fringe condition is obtained by the influence matrix of DM.

6.4 Experiment Results

The DM and deflectometry were calibrated before the measurement. The responses of DM to the action of actuators were calculated. The actuators have been shown to behave linearly. Figure 6.2 shows the DM shape after the actuators are tuned to obtain a flat surface. The flatten DM is set as the initial condition of DM in the fringe null process. Figure 6.3 shows the measurement results of a DM surface with random amounts of 4^{th} - 15^{th} Zernike terms using Zygo Verifire interferometer and deflectometry, showing the deflectometry system result is comparable with the commercial interferometer.

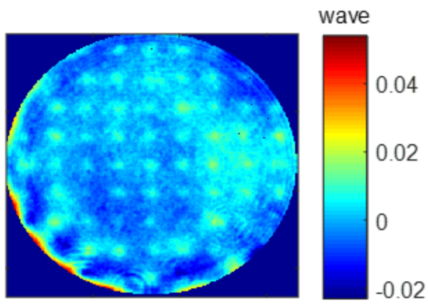

PV=0.077λ, rms=0.006λ

Figure 6.2 Phase map of the DM surface after the actuators are tuned to obtain a flat surface

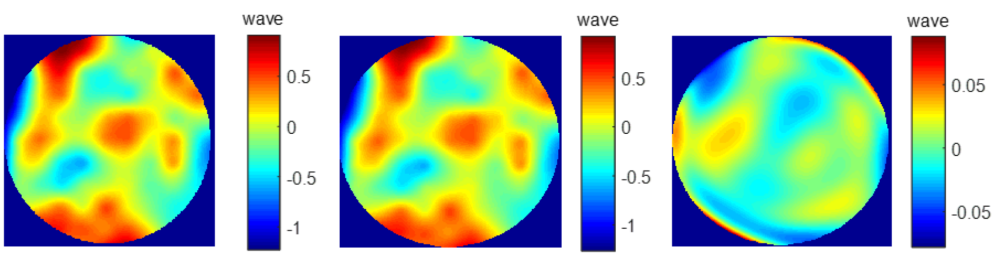

PV=2.1363λ, rms=0.3184λ (a) PV=2.1823λ, rms=0.3209λ (b) PV=0.1662λ, rms=0.0178λ (c)

Figure 6.3 Measurement results of a DM surface using (a) Zygo interferometer, (b) deflectometry system, and (c) difference between Zygo interferometer and deflectometry system.

To verify the accuracy of the proposed method, a biconic surface with a radius of 25 mm and a conic of 1.0 in *x*-direction was measured with Zygo Verifire laser interferometer and our system. Figure 6.4(a) shows the measurement result of Zygo interferometer. Figure 6.4(b) is the measurement result from the proposed system in near null fringe condition. The difference between Figure 6.4(a) and Figure 6.4(b) is shown in Figure 6.4(c). There is about 0.05 wave difference in the RMS wavefront. One reason is the speckle noise caused by the laser. Another possible reason is that only first order approximation of wavefront change caused by S_{DM} is considered. For a large deviation of DM, the retrace error is unavoidable [123].

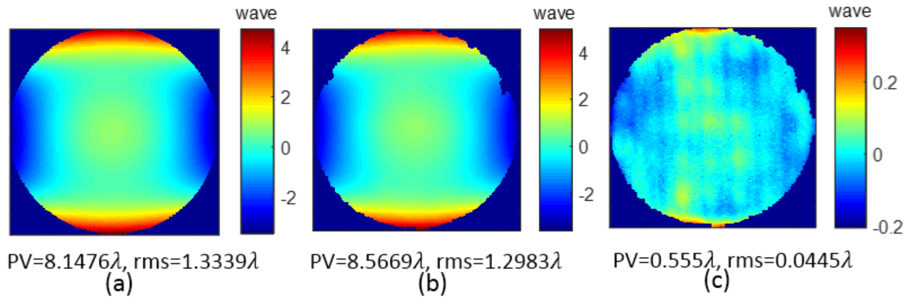

Figure 6.4 Phase map of the biconic surface measured by (a) Zygo interferometer (b) the proposed system, and (c) difference between Zygo interferometer and the proposed system.

To demonstrate the capability of the proposed system for freeform metrology, a freeform surface with a radius of 26 mm, conic of -1 in y-direction and radius of 23.5 mm, conic of -2 in *x*-direction was first measured using Zygo Verifire interferometer. Due to the large surface slope, the commercial interferometer cannot measure this surface. The interferogram is shown in Figure 6.5. The top and bottom parts of the fringes in the interferogram are missed, and the fringes of most part of the interferogram are too dense.

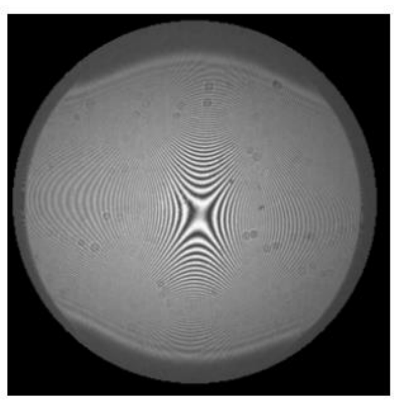

Figure 6.5 Interferogram of a freeform surface from Zygo Verifire interferometer.

The same freeform surface was tested in our system. The no-fringe areas are shown in the top and bottom parts in Figure 6.6(a). In the first step, the no-fringe areas were searched by the grayscale response of the camera. The system performance metric J_1 is defined in Equation 6.5. The performance metric J_1 of the restoring fringe is shown in Figure 6.6(g). The optimization process took 7 seconds.

After the fringe was restored, the DM was fine tuned to reduce the dense fringe. The system performance metric J_2 for this tuning process is defined in Equation 6.6. Figure 6.6(c) shows the final relaxed fringe after the second step. The performance metric J_2 of relaxing fringe is shown in Figure 6.6(h). This optimization process took about 60 seconds. During turning DM to reduce the fringe density, phase information captured by snapshot interferometer was used as a performance metric to describe the fringe density. The phase ambiguity map defined as Equation 6.7 is shown in Figure 6.6(e)(f). Figure 6.6(e) is the ambiguity map corresponding to Figure 6.6(b), while Figure 6.6(f) is the ambiguity map corresponding to Figure 6.6(c). By using the ambiguity map as the performance metric J_2, the optimization process is more robust since it's less sensitive to noise such as laser instability and background illumination.

After the fringe density was reduced, the surface under test can be measured. In order to minimize the retrace error and improve the accuracy, we still need to get null fringe condition. The influence matrix of DM, calibrated using the interferometer, was used to calculate the voltage of each actuator to achieve the null fringe condition. Using the influence matrix is much faster than using the SPGD algorithm to get null fringe. Figure 6.6(d) shows the final relaxed fringe. It contains some residue aberrations. The measurement results of near null fringe and freeform surface are shown in Figure 6.7. Figure 6.7(a) shows the near null phase measured by the interferometer. Figure 6.7(b) is the final processed measurement result of the freeform surface.

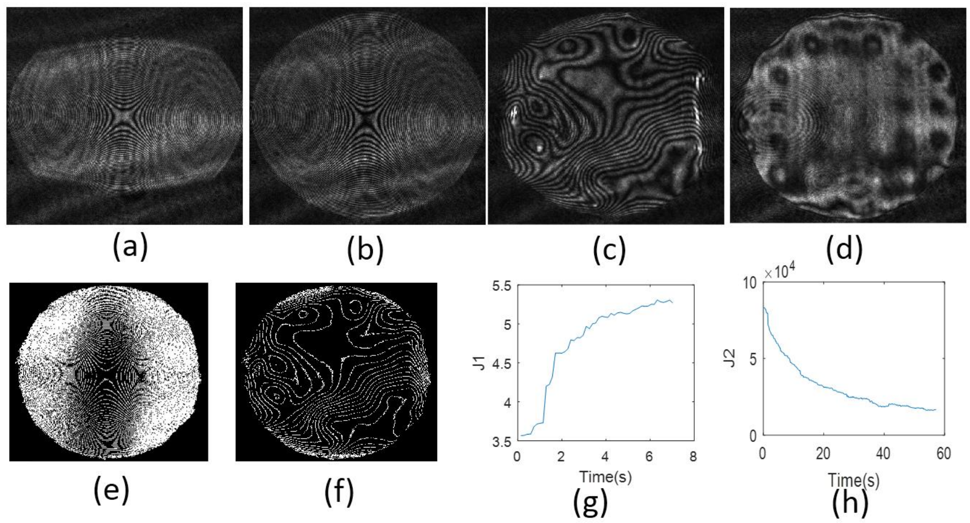

Figure 6.6 Interferometer fringes: (a) original interferogram with no-fringe area; (b) interferogram after restoring fringe; (c) interferogram after relaxing fringe; (d) final restored fringe. Ambiguity map: (e) after restoring fringe; (f) after relaxing fringe. System performance metric J in: (g) restoring fringe; (h) relaxing fringe

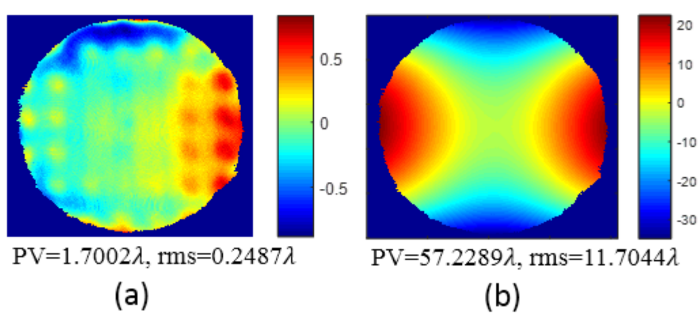

Figure 6.7 (a) Interferometer measurement result with near null fringe (b) Final processed measurement result for the freeform surface.

6.5 Conclusion

In this chapter, we propose a snapshot, adaptive interferometric system with a DM as an adaptive null component for freeform surface metrology. An adaptive null algorithm has been developed to drive the DM, and a deflectometry system is used to measure the DM shape with high spatial resolution. The process of establishing the relationship between DM wavefront and DM shape is proposed. The snapshot measurement is enabled by a pixelated polarization camera, increasing the measurement speed and reducing the environmental errors. Although potentially it is a powerful interferometric system for freeform surface testing, significant studies are needed to reduce the retrace error, improve the measurement accuracy of the DM surface shape, establish more accurate relationship between DM wavefront and DM surface shape and the relationship between the effective DM dimension and the dimension of the surface under test.

Chapter 7 Conclusion

Phase-shifting interferometry is an established method for optical metrology for its high measurement accuracy, rapid measurement, good results for low contrast fringes, and independence of irradiance variations across the pupil. Methods for phase-shifting include temporal phase shifting that introduces a phase-shift sequentially, and spatial phase-shifting which split the beam into parallel channels for simultaneous measurement. A single shot interferometry based on spatial phase-shifting can reduce phase error caused by environment noise like vibration and air turbulence, which is often the largest source of error in phase-shifting interferometry. As a spatial-phase shifting method, the pixelated polarization camera method has the advantages of a common path configuration, compact design, achromatic over a very wide range, and fixed spatial interference pattern results in fast processing, which makes it suitable for dynamic and vibration insensitive measurement. In this dissertation, snapshot phase-shifting interferometry systems based on pixelated polarization camera are presented. The principle and application of each system are theoretical analyzed and experimental demonstrated in each chapter.

Chapter 2 introduces a dual-mode snapshot interferometry system for on-machine metrology. A laser interferometer for surface shape measurement and an interference microscope for surface roughness measurement are combined within this system. A mono-polarization camera is applied to acquire the four $\pi/2$ phase-shifted interferograms simultaneously. The mono-polarization camera calibration and system error caused by optical components are discussed in this chapter.

This system is insensitive to environment noise and compact, which makes it suitable for working in the fabrication environment.

Chapter 3 introduces a snapshot multi-wavelength interference microscope for high speed measurement of large vertical range discontinuous microstructures and surface roughness. One limitation of the phase-shifting interference microscopes is that the height difference between two adjacent points must be less than $\lambda/4$, which could be solved by using a multi-wavelength method. A custom color polarization camera, which contains a CMOS camera with a linear micro-polarizer array and Bayer filter, is used to capture phase-shifted interferograms in red, green, and blue channels simultaneously. Camera calibration for this custom color polarization is demonstrated in this chapter. A multi-wavelength method with lasers and LED as a light source is also presented, which could increase the measurement range as well as keep the high quality surface roughness measurement.

Chapter 4 introduces s multi-wavelength quantitative polarization and phase microscope for measuring the quantitative phase and optical anisotropy information. This system integrates a polarized light microscope and a snapshot quantitative phase microscope in a single system. A novel full-Stokes camera operating in the red, green, and blue spectrum is used in this system. Stokes images in multi-wavelength can be reconstructed simultaneously by this system. The full-Stoke camera calibration algorithm and the Stokes image reconstruction algorithm are discussed in this chapter. The capability of phase and polarization information reconstruction of this system is demonstrated with theoretical analysis and experiment results. With the advantages of simple structure and rapid measurement, this system is a useful tool in measuring quantitative polarization and phase information.

Chapter 5 introduces a snapshot phase-shifting diffraction phase microscope. The diffraction phase microscope is widely used in biomedical sample measurement due to its common-path configuration. By combing the diffraction phase microscope and spatial phase-shifting technology with a polarization camera, the phase map of the biomedical sample can be obtained simultaneously. The environment noise can be minimized by this common path configuration of the system. A high spatial resolution phase map is reconstructed with a phase-shifting algorithm. This approach shows a potential application for phase imaging of dynamic processes with high resolution in a high vibration environment.

Chapter 6 introduces a snapshot adaptive freeform null testing system with a deformable mirror (DM) compensator. This interferometric system can measure unknown freeform surfaces with this DM compensator. The final freeform surface can be reconstructed as a combination of the interferometric null measurement and the DM shape obtained by a deflectometry system. Spatial phase-shifting is achieved by the pixelated polarization camera, which increases the measurement speed of the system and reduces the environmental noise. An adaptive null algorithm has been developed to drive the DM and the deflectometry system. The process of establishing the relationship between the DM wavefront and the DM shape is also proposed. This system has been demonstrated as a useful tool for unknown freeform surface measurement.

Publications

First Author Publications

- X. Tian, X. Tu, J. Zhang, O. Spires, N. Brock, S. Pau, and R. Liang, “Snapshot multi-wavelength interference microscope,” Opt. Express **26**(14), 18279–18291 (2018).
- X. Tian, Y. Zhang, A. Sohn, O. J. Spires, and R. Liang, "Dual-mode snapshot interferometric system for on-machine metrology," Opt Eng **58**, 044104 (2019).
- X. Tian, X. Tu, K. Croce, G. Yao, H. Cai, N. Brock, S. Pau, and R. Liang, "Multi-wavelength quantitative polarization and phase microscope," Biomed. Opt. Express **10**(4), 1638-1648 (2019).
- X. Tian and R. Liang, "Snapshot phase-shifting diffraction phase microscope," Opt. Lett 45(12), 3208-3211 (2020).

Other Publications

- Y. Zhang, X. Tian, and R. Liang, "Fringe-print-through error analysis and correction in snapshot phase-shifting interference microscope," Opt. Express **25**(22), 26554-26566 (2017).
- X. Tu, O. J. Spires, X. Tian, N. Brock, R. Liang, and S. Pau, "Division of amplitude RGB full-Stokes camera using micro-polarizer arrays," Opt. Express **25**(26), 33160-33175 (2017).
- D. Wang, X. Tian, P. Xu, J. Liang, H. Wu, O. Spires, and R. Liang, "Compact snapshot multi-wavelength interferometer," Opt. Lett **44**(18), 4463-4466 (2019).
- Y. Zhang, X. Tian, and R. Liang, "SPGD and Newton iteration mixed algorithm used in freeform surface metrology," Opt. Lasers Eng. **129**, 106050 (2020).

References

[1] E. P. Goodwin and J. C. Wyant, "Field guide to interferometric optical testing." SPIE Press, Bellingham (2006).
[2] D. Malacara, ed., Optical Shop Testing, 3rd ed. (John Wiley and Sons, 2007).
[3] A. A. Michelson and E. W. Edward, "LVIII. On the relative motion of the earth and the luminiferous Æther." The London, Edinburgh, and Dublin Philosophical Magazine and Journal of Science, 24(151), 449-463 (1887).
[4] J. C. Wyant, “Dynamic interferometry,” Opt. Photon. News 14(4), 36–41 (2003).
[5] N. Brock, J. Hayes, B. Kimbrough, J. Millerd, M. North-Morris, M. Novak, and J. C. Wyant, “Dynamic interferometry,” Proc. SPIE5875, 58750F (2005).
[6] H. H. Barrett and K. J. Myers, Foundations of Image Science (Wiley, 2003).
[7] M. Takeda, H. Ina, and S. Kobayashi, “Fourier-transform method of fringe-pattern analysis for computer-based topography and interferometry,” J. Opt. Soc. Am. A 72, 156–160 (1982).
[8] K. Creath, “Phase-shifting speckle interferometry,” Appl. Opt. 24, 3053–3058, (1985).
[9] S. L. Hahn, Hilbert transforms in signal processing (Artech House, Boston, 1996).
[10] Q. Kemao, “Two-dimensional windowed Fourier transform for fringe pattern analysis: Principles, applications and implementations,” Opt. Lasers Eng. 45(2), 304–317 (2007).
[11] J. Zhong and J. Weng, “Spatial carrier-fringe pattern analysis by means of wavelet transform: wavelet transform profilomatry,” Appl. Opt. 43, 4993–4998 (2004).
[12] J. M. Bioucas-Dias and G. Valadão, “Phase Unwrapping via Graph Cuts,” IEEE Trans. Image Process. 16(3), 698–709 (2007).
[13] P. Hariharan, Basics of InTterferometry. (Elsevier, Second Edition 2007).
[14] R. K. Leach, Optical measurement of surface topography (Springer, Berlin Heidelberg, 2011).
[15] J. A. Soobitsky, "Piezoelectric micromotion actuator." U.S. Patent No. 4,577,131 (1986).
[16] S. Helen, M. Kothiyal, and R. Sirohi, “Achromatic phase shifting by a rotating polarizer,” Opt. Commun. 154, 249–254 (1998).
[17] S. S. Helen, M. P. Kothiyal, and R. S. Sirohi, “Phase shifting by a rotating polarizer in white-light interferometry for surface profiling,” J. Mod. Opt. 46, 993–1001 (1999).
[18] M. Kujawinska, “Spatial phase measurement methods,” in Interferogram Analysis: Digital Fringe Pattern Measurement, D. W. Robinson and G. Reid, eds. (IOP, 1993), pp. 141–193.
[19] M. Kujawinska and J. Wojciak, “Spatial-carrier phase-shifting technique of fringe pattern analysis,” Proc. SPIE 1508, 61–67 (1991).
[20] M. Pirga and M. Kujawinska, “Two directional spatial-carrier phase-shifting method for analysis of crossed and closed fringe patterns,” Opt. Eng. 34(8), 2459–2466 (1995).
[21] A. J. P. van Haasteren and H.J. Frankena, “Real-time displacement measurement using a multicamera phase-stepping speckle interferometer,” Appl. Opt. 33, 4137–4142 (1994).
[22] R. Smythe and R. Moore, “Instantaneous Phase Measuring Interferometry,” Opt. Eng. 23(4), 361–364 (1984).
[23] C. L. Koliopoulos, “Simultaneous phase-shift interferometer,” Proc. SPIE 1531, 119–127 (1992).
[24] K. Qian, H. Miao, and X. Wu, “Real-time polarization phase shifting technique for dynamic deformation measurement,” Opt. Lasers Eng. 31(4), 289–295 (1999).
[25] J. E. Millerd and J. C. Wyant, “Simultaneous phase-shifting Fizeau interferometer,” U.S. Patent 7,057,738 (2006).
[26] J. Millerd, N. Brock, J. Hayes, M. North-Morris, M. Novak, and J. Wyant, “Pixelated phase-mask dynamic interferometer,” Proc. SPIE 5531, 304–314 (2004).
[27] K. Creath, “Phase-Measurement Interferometry Techniques,” Prog. Opt. 26, 349–393 (1988).
[28] https://thinklucid.com/tech-briefs/polarization-explained-sony-polarized-sensor/
[29] J. C. Wyant and J. Schmit, "Computerized interferometric measurement of surface microstructure," Proc SPIE 2782, 26-37 (1996).

[30] G. Y. Tian and R. Lu, "Hybrid vision system for online measurement of surface roughness," J. Opt. Soc. Am. A, **23**(12), 3072-3079 (2006).
[31] Y. Quinsat, C. Tournier, “In situ non-contact measurements of surface roughness,” Precision Engineering, **36**(1), 97-103 (2012).
[32] H. Nouira, N. E. Hayek, X. Yuan, and N. Anwer, “Characterization of the main error sources of chromatic confocal probes for dimensional measurement,” Meas. Sci. Technol. **25**(4), 044011 (2014).
[33] X. Zou, X. Zhang, G. Li, Z. Li, and T. Sun, “Non-contact on-machine measurements using a chromatic confocal probe for an ultra-precision turning machine,” Int J Adv Manuf Technol, **90**(5-8), 2163-2172 (2017).
[34] P. Su, M Khreishi, R Huang, T, Su, and J. H. Burge, “Precision aspheric optics testing with SCOTS: a deflectometry approach,” Proc. SPIE 8788, 87881E(2013).
[35] D. Lin, X. Jiang, F. Xie, W. Zhang, L. Zhang, and I. Bennion, “High stability multiplexed fibre interferometer and its application on absolute displacement measurement and on-line surface metrology,” Opt. Express **12**(23), 5729-5734(2004).
[36] F. Xie, M. Li, D. Song, J. Sun, and T. Zhang, “Large range and high resolution on-line displacement measurement system by combining double interferometers,” Opt. Express **18**(24), 24961-24968(2010).
[37] F. Xie, J. Wang, S. Ma, and Y. Liu, “Multiplexing optical fiber low coherence and high coherence interferometrc system with large range and high resolution for on-line measurement,” Measurement **46**(1), 171-176(2013).
[38] X. Tian, Y. Zhang, A. Sohn, O. J. Spires, R. Liang, "Dual-mode snapshot interferometric system for on-machine metrology," Opt Eng **58**, 044104 (2019).
[39] Z. Chen, X. Wang, and R. Liang, "Calibration method of microgrid polarimeters with image interpolation," Appl. Opt. **54**(5), 995-1001 (2015).
[40] S. K. Gao and V. Gruev, “Bilinear and bicubic interpolation methods for division of focal plane polarimeters,” Opt. Express **19**(27), 26161–26173 (2011).
[41] M. Novak, J. Millerd, N. Brock, M. North-Morris, J. Hayes, and J. Wyant, “Analysis of a micropolarizer array-based simultaneous phase-shifting interferometer,” Appl. Opt. **44**(32), 6861–6868 (2005).
[42] Y. Zhang, X. Tian, and R. Liang, "Fringe-print-through error analysis and correction in snapshot phase-shifting interference microscope," Opt. Express **25**(22), 26554-26566 (2017).
[43] Y. Zhang, X. Tian, R. Liang, “Random two-step phase shifting interferometry based on Lissajous ellipse fitting and least squares technologies,” Opt. Express **26**(12), 15059-15071 (2018).
[44] Y. Zhang, X. Tian, and R. Liang, “Three-step random phase retrieval approach based on difference map normalization and diamond diagonal vector normalization,” Opt. Express **26**(22), 29170-29182
[45] P. de Groot, “Principles of interference microscopy for the measurement of surface topography,” Adv. Opt. Photonics **7**(1), 1–65 (2015).
[46] P. Sandoz, “Wavelet transform as a processing tool in white-light interferometry,” Opt. Lett. **22**(14), 1065–1067 (1997).
[47] M. Li, C. Quan, and C. J. Tay. "Continuous wavelet transform for micro-component profile measurement using vertical scanning interferometry." Opt. Laser Technol. **40**(7), 920-929 (2008).
[48] S. Ma, C. Quan, R. Zhu, C. J. Tay, and L. Chen, "Surface profile measurement in white-light scanning interferometry using a three-chip color CCD," Appl. Opt. **50**(15), 2246-2254 (2011).
[49] P. K. Upputuri, L. Gong, H. Wang, M. Pramanik, K. M. Nandigana, and M. P. Kothiyal, "Measurement of large discontinuities using single white light interferogram," Opt. Express **22**(22), 27373-27380 (2014).
[50] Y. -Y. Cheng and J. C. Wyant, "Multiple-wavelength phase-shifting interferometry," Appl. Opt. **24**(6), 804-807 (1985).
[51] A. Pförtner and J. Schwider, "Red-green-blue interferometer for the metrology of discontinuous structures," Appl. Opt. **42**(4), 667-673 (2003).
[52] A. Wada, M. Kato, and Y. Ishii, "Large step-height measurements using multiple-wavelength holographic interferometry with tunable laser diodes," J. Opt. Soc. Am. A **25**(12), 3013-3020 (2008).
[53] M. B. North-Morris, J. E. Millerd, N. J. Brock, and J. B. Hayes, “Phase shifting multi-wave length dynamic interferometry,” Proc. SPIE 5531, 64–75 (2004)
[54] A. Safrani and I. Abdulhalim, "Hight speed 3D imaging using two wavelengths parallel phase shift interferometry," Opt. Letter. **54**(16), 5083-5087 (2015).

[55] M. Ney, A. Safrani, and I. Abdulhalim, "Three wavelengths parallel phase-shift interferometry for real-time focus tracking and vibration measurement," Opt. Letter. **42**(4), 719-722 (2017).
[56] J. Kühn, T. Colomb, F. Montfort, F. Charrière, Y. Emery, E. Cuche, P. Marquet, and C. Depeursinge, "Real-time dual-wavelength digital holographic microscopy with a single hologram acquisition," Opt. Express **15**(12), 7231-7242 (2007).
[57] C. J. Mann, P. R. Bingham, V. C. Paquit, and K. W. Tobin, "Quantitative phase imaging by three-wavelength digital holography," Opt. Express **16**(13), 9753-9764 (2008).
[58] M. T. Rinehart, N. T. Shaked, N. J. Jenness, R. L. Clark, and A. Wax, "Simultaneous two-wavelength transmission quantitative phase microscopy with a color camera," Opt. Lett. **35**(15), 2612-2614 (2010).
[59] X. Tian, X. Tu, J. Zhang, O. Spires, N. Brock, S. Pau, and R. Liang, "Snapshot multi-wavelength interference microscope," Opt. Express **26**(14), 18279–18291 (2018).
[60] X. Tu, O. J. Spires, X. Tian, N. Brock, R. Liang, and S. Pau, "Division of amplitude RGB full-Stokes camera using micro-polarizer arrays," Opt. Express **25**(26), 33160-33175 (2017).
[61] Y. -Y. Cheng and J. C. Wyant, "Two-wavelength phase shifting interferometry," Appl. Opt. **23**(24), 4539-4543 (1984).
[62] K. Creath, "Step height measurement using two-wavelength phase-shifting interferometry," Appl. Opt. **26**(14), 2810-2816 (1987).
[63] J. Gass, A. Dakoff, and M. K. Kim, "Phase imaging without 2π ambiguity by multiwavelength digital holography," Opt. Lett. **28**(13), 1141-1143 (2003).
[64] https://thinklucid.com/phoenix-polarization-color-camera-featuring-sony-imx250myr-sensor-at-cvpr-2018/
[65] G. Popescu, L. P. Delflores, J. C. Vaughan, K. Badizadegan, H. Iwai, R. R. Dasari and M. S. Feld, "Fourier phase microscopy for investigation of biological structures and dynamics," Opt. Lett. **29**, 2503-5 (2004).
[66] B. Rappaz, P. Marquet, E. Cuche, Y. Emery, C. Depeursinge, and P. J. Magistretti, "Measurement of the integral refractive index and dynamic cell morphometry of living cells with digital holographic microscopy," Opt. Express **13**, 9361-9373 (2005).
[67] T. Ikeda, G. Popescu, R.R. Dasari, and M.S. Feld, "Hilbert phase microscopy for investigating fast dynamics in transparent systems," Opt. Lett. **30**, 1165 (2005).
[68] G. Popescu, T. Ikeda, R. R. Dasari, and M. S. Feld, "Diffraction phase microscopy for quantifying cell structure and dynamics," Opt. Lett. **31**, 775–777 (2006) .
[69] W. Choi, C. Fang-Yen, K. Badizadegan, S. Oh, N. Lue, R. R. Dasari, and M. S. Feld, "Tomographic phase microscopy," Nature Methods **4**, 717–719 (2007).
[70] K. Creath and G. Goldstein, "Dynamic quantitative phase imaging for biological objects using a pixelated phase mask," Biomed. Opt. Express **3**(11), 2866–2880 (2012).
[71] M. Koike-Tani, T. Tani, S. B. Mehta, A. Verma, and R. Oldenbourg, "Polarized light microscopy in reproductive and developmental biology," Mol. Reprod. Dev. **82**(7-8), 548–562 (2015).
[72] I. H. Shin, S. M. Shin, and D. Y. Kim, "New, simple theory-based, accurate polarization microscope for birefringence imaging of biological cells," J. Biomed. Opt. **15**(1), 016028 (2010).
[73] M. Shribak, "Complete polarization state generator with one variable retarder and its application for fast and sensitive measuring of two-dimensional birefringence distribution," JOSA A **28**(3), 410-419 (2011).
[74] S. Sugita and T. Matsumoto, "Quantitative measurement of the distribution and alignment of collagen fibers in unfixed aortic tissues," J. Biomech. **46**, 1403–1407 (2013).
[75] C. Li and Y. Zhu, "Quantitative polarized light microscopy using spectral multiplexing interferometry," Opt. Lett. **40**(11), 2622–2625 (2015).
[76] S. Aknoun, P. Bon, J. Savatier, B. Wattellier, and S. Monneret, "Quantitative retardance imaging of biological samples using quadriwave lateral shearing interferometry," Opt. Express **23**(12), 16383–16406 (2015).
[77] C. Li, S. Chen, M. Klemba, and Y. Zhu, "Integrated quantitative phase and birefringence microscopy for imaging malaria-infected red blood cells," Journal of biomedical optics **21**(9), 090501 (2016).
[78] B. Yayebi, J. h. Kim, J. H. Han, "Review on multi-wavelength quantitative phase microscopy," in 2016 4th international Winter Conference on Brain-Computer Interface, 1-2 (2016).
[79] Y. Park, M. Diez-Silva, G. Popescu, G. Lykotrafitis, W. Choi, M. S. Feld, and S. Suresh, "Refractive index maps and membrane dynamics of human red blood cells parasitized by Plasmodium falciparum," Proc. Natl. Acad. Sci. U.S.A. **105**(37), 13730-13735 (2008)

[80] P. Ferraro, S. Grilli, L. Miccio, D. Alfieri, S. De Nicola, A. Finizio, and B. Javidi, "Full color 3-D imaging by digital holography and removal of chromatic aberrations," J. Display Technol., **4**(1), 97-100 (2008).
[81] A. Wax, C. Yang, V. Backman, K. Badizadegan, C. W. Boone, R. R. Dasar, M. S. Feld, "Cellular organization and substructure measured using angle-resolved low-coherence interferometry," Biophys. J. **82**(4), 2256-2264 (2002).
[82] C. J. Mann, P. R. Bingham, V. C. Paquit, and K. W. Tobin, "Quantitative phase imaging by three-wavelength digital holography," Opt. Esxpress **16**(13), 9753-9764 (2008).
[83] N. Warnasooriya and M. K. Kim, "LED-based multi-wavelength phase imaging interference microscopy," Opt. Express **15**(15), 9239-9247 (2007).
[84] M. R. Jafarfard, S. Moon, B. Tayebi, and D. Y. Kim, "Dual-wavelength diffraction phase microscopy for simultaneous measurement of refractive index and thickness," Opt. Lett. **39**(10), 2908-2911 (2014).
[85] P. Gao, B. Yao, R. Rupp, J. Min, R. Guo, B. Ma, J. Zheng, M. Lei, S. Yan, D. Dan, and T. Ye, "Autofocusing based on wavelength dependence of diffraction in two-wavelength digital holographic microscopy," Opt. Lett. **37**(7), 1172-1174 (2012).
[86] Y. Park, T. Yamauchi, W. Choi, R. Dasari, and M. S. Feld, "Spectroscopic phase microscopy for quantifying hemoglobin concentrations in intact red blood cells," Opt. Lett. **34**(23), 3668-3670 (2009).
[87] H. Pham, B. Bhaduri, H. Ding, and G. Popescu, "Spectroscopic diffraction phase microscopy," Opt. Lett. **37**(16), 3438-3440 (2012).
[88] D. Fu, W. Choi, Y. Sung, Z. Yaqoob, R. R. Dasari, and M. Feld, "Quantitative dispersion microscopy," Biomed. Opt. Express, **1**(2), 347-353 (2010).
[89] M. Rinehart, Y. Zhu, and A. Wax, "Quantitative phase spectroscopy," Biomed. Opt. Express, **3**(5), 958-965 (2012).
[90] Y. Jang, J. Jang, and Y. Park, "Dynamic spectroscopic phase microscopy for quantifying hemoglobin concentration and dynamic membrane fluctuation in red blood cells," Opt. Express, **20**(9), 9673-9681 (2012).
[91] X. Tian, X. Tu, K. Croce, G. Yao, H. Cai, N. Brock, S. Pau, and R. Liang. "Multi-wavelength quantitative polarization and phase microscope." Biomed. Opt. Express **10**(4), 1638-1648 (2019).
[92] C. Fan and G. Yao, "Mapping local retardance in birefringent samples using polarization sensitive optical coherence tomography," Opt. Lett. **37**, 1415–1417 (2012).
[93] E. Cuche , F. Bevilacqua , and C. Depeursinge, " Digital holography for quantitative phase-contrast imaging ," Opt. Lett. 24 , 291 -3 (1999).
[94] Y. Park, C. Depeursinge, and G. Popescu, "Quantitative phase imaging in biomedicine," Nat. Photonics 12(10), 578–589 (2018)..
[95] Y. K. Park, G. Popescu, K. Badizadegan, R. R. Dasari, and M. S. Feld, "Diffraction phase and fluorescence microscopy," Opt. Express 14(18), 8263–8268 (2006).
[96] H. V. Pham, C. Edwards, L. L. Goddard, and G. Popescu, "Fast phase reconstruction in white light diffraction phase microscopy," Appl. Opt. **52**(1), A97–A101 (2013).
[97] I. Yamaguchi and T. Zhang, "Phase-shifting digital holography," Opt. Lett. **22**(16), 1268–1270 (1997).
[98] N. T. Shaked, T. M. Newpher, M. D. Ehlers, and A. Wax, "Parallel on-axis holographic phase microscopy of biological cells and unicellular microorganism dynamics," Appl. Opt. **49**(15), 2872–2878 (2010).
[99] P. Gao, B. Yao, J. Min, R. Guo, J. Zheng, T. Ye, I. Harder, V. Nercissian, and K. Mantel, "Parallel two-step phase-shifting point-diffraction interferometry for microscopy based on a pair of cube beamsplitters," Opt. Express **19**(3), 1930–1935 (2011).
[100] R. Guo, B. Yao, P. Gao, J. Min, J. Han, X. Yu, M. Lei, S. Yan, Y. Yang, D. Dan, and T. Ye, "Parallel on-axis phase-shifting holographic phase microscopy based on reflective point-diffraction interferometer with long-term stability," Appl. Opt. **52**(15), 3484–3489 (2013).
[101] M. Takeda, H. Ina, and S. Kobayashi, "Fourier-transform method of fringe-pattern analysis for computer-based topography and interferometry," J. Opt. Soc. Am. A **72**, 156–160 (1982).
[102] N. Lue, W. Choi, G. Popescu, T. Ikeda, R. R. Dasari, K. Badizadegan, and M. S. Feld, "Quantitative phase imaging of live cells using fast Fourier phase microscopy," Appl. Opt. 46(10), 1836–1842 (2007).
[103] L. Xue, J. Lai, S. Wang, and Z. Li, "Single-shot slightly-off-axis interferometry based Hilbert phase microscopy of red blood cells," Biomed. Opt. Express **2**(4), 987–995 (2011).
[104] N. T. Shaked, Y. Zhu, M. T. Rinehart, and A. Wax, "Two-step-only phase-shifting interferometry with optimized detector bandwidth for microscopy of live cells," Opt. Express **17**(18), 15585–15591 (2009).

[105] Y. Yang, Z. Cheng, H. Zhang, Q. Yue, and C. Guo, "Quantitative phase imaging system with slightly-off-axis configuration and suitable for objects both larger and smaller than the size of the image sensor." Opt. Express **26**(13), 17199-17208 (2018).
[106] L. Ma, J. Zhang, X. Yang, Y. Li, and W. Jin, "White light diffraction phase microscopy with slightly off-axis blind two-step phase-shifting." Opt. Commun. **455**, 124563 (2020).
[107] X. Tian and R. Liang, "Snapshot phase-shifting diffraction phase microscope," Opt. Lett 45(12), 3208-3211 (2020).
[108] J. C. Wyant and V. P. Bennett, "Using Computer Generated Holograms to Test Aspheric Wavefronts," Appl. Opt. 11, 2833-2839 (1972)
[109] P. Zhou and J. H. Burge, "Fabrication error analysis and experimental demonstration for computer-generated holograms," Appl. Opt.46, 657-663 (2007)
[110] G. Baer, J. Schindler, C. Pruss, J. Siepmann, and W. Osten, "Calibration of a non-null test interferometer for the measurement of aspheres and free-form surfaces," Opt. Express **22**(25), 31200-31211 (2014)
[111] P. Murphy, J. Fleig, G. Forbes, D. Miladinovic, G. DeVries, and S. O'Donohue, "Subaperture stitching interferometry for testing mild aspheres," Proc. SPIE 6293, 62930J (2006).
[112] D. Liu, Y. Yang, C. Tian, Y. Luo, and L. Wang, "Practical methods for retrace error correction in nonnull aspheric testing," Opt. Express **17**(9), 7025-7035 (2009).
[113] P. Su, R. E. Parks, L. Wang, R. P. Angel, and J.H. Burge, "Software configurable optical test system: a computerized reverse Hartmann test," Appl. Opt. **49**(23), 4404-4412 (2010).
[114] E. Nadim, N. Hichem, A. Nabil, D. Mohamed, and G. Olivier, "Comparison of Tactile and Chromatic Confocal Measurements of Aspherical Lenses for Form Metrology," Int. J. Precis. Eng. Manuf. **15**(5), 821–829 (2014).
[115] E. B. Hughes, A. Wilson, and G. N. Peggs. "Design of a high-accuracy CMM based on multi-lateration techniques." CIRP Annals-Manufacturing Technology 49(1), 391-394 (2000).
[116] S. DeFisher, M. Bechtold, and D. Mohring. "A non-contact surface measurement system for freeform and conformal optics." In Proc. SPIE, vol. 8016, p. 80160W (2011).
[117] Y. Zhang, H. Cheng, R. Wu, and R. Liang, "Data processing for point-based in situ metrology of freeform optical surface," Opt. Express 25(12), 13414-13424 (2017).
[118] C. Pruss and H. J. Tiziani, "Dynamic null lens for aspheric testing using a membrane mirror," Opt. Commun. **233**(1), 15–19(2004).
[119] K. Fuerschbach, K. P. Thompson, and J. P. Rolland, "Interferometric measurement of a concave, Φ-polynomial, Zernike mirror," Opt. Lett. **39**(1), 18-21 (2014).
[120] L. Huang, H. Choi, W. Zhao, L. R. Graves, and D. W. Kim, "Adaptive interferometric null testing for unknown freeform optics metrology," Opt. Lett.**41**(23), 5539-5542 (2016).
[121] L. Zhang, S. Zhou, D. Li, Y. Liu, T. He, B. Yu, and J. Li, "Pure adaptive interferometer for free form surfaces metrology," Opt. Express **26**(7), 7888-7898 (2018).
[122] M. A. Vorontsov and V. P. Sivokon, "Stochastic parallel-gradient-descent technique for high-resolution wave-front phase-distortion correction," J. Opt. Soc. Am. A **15**(10), 2745–2758 (1998).
[123] Y. He, L. Huang, X. Hou, W. Fan, and R. Liang, "Modeling near-null testing method of a freeform surface with a deformable mirror compensator," Appl. Opt. **56**(33), 9132-9138 (2017).